IN THE UNITED STATES PATENT AND TRADEMARK OFFICE

In Re Patent Application Of: Hui Chun Liu   Our File No: 11258-01 US

Application No: 09/836,464   Group Art Unit: 2878

Filed: 04/18/2001   Examiner: Lee, Shun K.

Title: Room Temperature Quantum Well Infrared Detector

June 16, 2004

Commissioner for Patents
P.O. Box 1450
Alexandria, VA 22313-1450, U.S.A.

Declaration Under 37 CFR 1.132

Sir:

I, Hui Chun Liu, the applicant of the above-identified patent application and the inventor of the subject matter described and claimed therein, depose and state:

1.   One skilled in the art at the time of the invention would have been skeptical of the teaching of Delacourt et al. at column 4, lines 40-44, relating to operation of a quantum well infrared photodetector at ambient temperature (i.e. 300 K). Delacourt et al. merely states that "**to be capable** of working at ambient temperature, the potential barrier to be crossed for the electrons, which has a value $h \cdot v_1^0$, should be greater than kT=26 meV....". Of course, a worker skill in the art at the time of the invention would have agreed that this statement is true. However, the same skilled worker would not have expected such a detector (solely by virtue of having a potential barrier greater than kT=26 meV) to **actually** work at ambient temperature (i.e. 300 K). The skepticism of the skilled worker would be based in part upon the wording that is used by Delacourt et al., which is merely speculative in nature. For instance "to be capable of working at ambient temperature..." and "should be greater than kT=26 meV." Secondly, the skepticism of the skilled worker would be based in part upon the overwhelming number of prior art teachings, and the generally accepted wisdom, that QWIP detectors require cryogenic cooling. As evidence supporting this last statement, I have included in Attachments A-E numerous publications, acquired from a wide variety of sources, which are unanimous in the belief that QWIP devices require cooling to cryogenic temperatures. This information is being provided

1

since secondary considerations such as skepticism of experts, including myself, are relevant to the issue of obviousness and must be considered in every case in which they are present.

2.   Attached to this my declaration and marked as exhibit A is a review article authored by A. Rogalski, whom I consider to be an expert in the field of the invention, which was published in the Journal of Applied Physics, a widely read publication in the field of the invention, and which describes the state of the art of infrared detectors during the period of time preceding December 20, 2002. Accordingly, this article establishes the state of the art of infrared detectors at about the time of and immediately after the date of the invention. In the article, Rogalski states at page 4357 that cooling is the main obstacle to a more widespread use of IR systems based on semiconductor photodetectors because it makes them bulky, heavy, expensive and inconvenient to use. Figure 4 on page 4360 and Figure 21 on page 4369 show typical comparisons for infrared detectors of different types, emphasizing the requirement that QWIP devices be cooled to cryogenic temperatures. This is evidence supporting the widespread acceptance that QWIPs must operate at cryogenic temperatures.

3.   Attached to this my declaration and marked as exhibit B is an article authored by J.Y. Andersson that was published in the Journal of Applied Physics, a widely read publication in the field of the invention, and which describes the state of the art of QWIP devices around the time of November, 1995. Anderson at Figure 6 on page 6303 shows detector operating temperatures over the range 60-77 K. This is further evidence supporting the widespread acceptance that QWIPs must operate at cryogenic temperatures.

4.   Attached to this my declaration and marked as exhibit C is an article authored by myself, H.C. Liu, and Published in Appl. Phys. Lett. Vol. 61, No. 22, 30 November 1992. At Figure 2 on page 2705, the detector operating temperatures ranging from about 40-80 K are shown for detector operation with background limited infrared operation. This is further evidence supporting the widespread acceptance that QWIPs must operate at cryogenic temperatures.

5.   Attached to this my declaration and marked as exhibit D is a document believed to be from the year 2000 and attributable to Fraunhofer-Institut für Angewandte Festkörperphysik IAF, which has a long standing tradition and competence in III-V compound semiconductors for electronic and optoelectronic applications. On page 30, it is indicated that the QWIPs are GaAs-based. Table 1, on page 30, lists several commercial camera products, each having a T_{Det} in the

2

range 60 to 90 K. This is further evidence supporting the widespread acceptance that QWIPs must operate at cryogenic temperatures.

6.   Attached to this my declaration and marked as exhibit E is a web page document with a copyright date of 2004, and attributable to Acreo. On the second page, first paragraph, it is stated that "cooling down to 70-73 K is necessary in order to reduce dark currents to a sufficiently low level." This is further evidence supporting the widespread acceptance that QWIPs must operate at cryogenic temperatures.

7.   The invention, as defined in the claims of the instant application, has already been the subject of copying by others. In particular, United States Patent Application Ser. No. 10/057,381 in the name of Plante (published as US 2003/0136909) was filed on January 23, 2002, which is less than nine months after the filing date of the instant application. Prior to the filing date of the Plante application, I disclosed to the Applicant of the Plante application specific features of the instant invention, including those features that are disclosed and claimed in the above-mentioned Plante application. At that time, the Applicant of the Plante application showed considerable interest, and in fact has since that time taken it upon himself to file a patent application claiming substantially the same subject matter. This information, which was discovered during a supplement search conducted on June 15, 2004, is being provided since secondary considerations such as copying by others are relevant to the issue of obviousness and must be considered in every case in which they are present.

7.   I acknowledge that willful false statements and the like are punishable by fine or imprisonment, or both (18 U.S.C. 1001) and may jeopardize the validity of the application or any patent issuing thereon.

8.   All statements made of declarant's own knowledge are true and all statements made on information and belief are believed to be true.

Signed,

_____   June 16, 2004

Hui Chun Liu   Date

3

EXHIBIT A

For

Declaration Under 37 CFR 1.132

US Application No. 09/836,464
Reply to Final Official Action mailed on April 16, 2004

APPLIED PHYSICS REVIEWS

Quantum well photoconductors in infrared detector technology

A. Rogalski
Institute of Applied Physics, Military University of Technology, 2 Kaliskiego St., 00-908 Warsaw, Poland

The paper compares the achievements of quantum well infrared photodetector (QWIP) technology with those of competitive technologies, with the emphasis on the material properties, device structure, and their impact on focal plane array (FPA) performance. Special attention is paid to two competitive technologies, QWIP and HgCdTe, in the long-wavelength IR (LWIR) and very-long-wavelength IR (VLWIR) spectral ranges. Because so far, the dialogue between the QWIP and HgCdTe communities is limited, the paper attempts to settle the main issues of both technologies. Such an approach, however, requires the presentation of fundamental limits to the different types of detectors, which is made at the beginning. To write the paper more clearly for readers, many details are included in the Appendix. In comparative studies both photon and thermal detectors are considered. Emphasis is placed on photon detectors. In this group one may distinguish HgCdTe photodiodes, InSb photodiodes, and doped silicon detectors. The potential performance of different materials as infrared detectors is examined utilizing the α/G ratio, where α is the absorption coefficient and G is the thermal generation rate. It is demonstrated that LWIR QWIP's cannot compete with HgCdTe photodiodes as single devices, especially at higher operating temperatures (>70 K). This is due to the fundamental limitations associated with intersubband transitions. The advantage of HgCdTe is, however, less distinct at temperatures lower than 50 K due to problems inherent in the HgCdTe material (p-type doping, Shockley–Read recombination, trap-assisted tunneling, surface and interface instabilities). Even though QWIP is a photoconductor, several of its properties, such as high impedance, fast response time, long integration time, and low power consumption, comply well with the requirements imposed on the fabrication of large FPA's. Due to a high material quality at low temperatures, QWIP has potential advantages over HgCdTe in the area of VLWIR FPA applications in terms of array size, uniformity, yield, and cost of the systems. The performance figures of merit of state-of-the-art QWIP and HgCdTe FPA's are similar because the main limitations come from the readout circuits. Performance is, however, achieved with very different integration times. The choice of the best technology is therefore driven by the specific needs of a system. In the case of readout-limited detectors a low photoconductive gain increases the signal-to-noise ratio and a QWIP FPA can have a better noise equivalent difference temperature than an HgCdTe FPA with a charge well of similar size. Both HgCdTe photodiodes and QWIP's offer multicolor capability in the MWIR and LWIR range. Powerful possibilities offered by QWIP technology are associated with VLWIR FPA applications and with multicolor detection. The intrinsic advantage of QWIP's in this niche is due to the relative ease of growing multicolor structures with a very low defect density. © *2003 American Institute of Physics.*
[DOI: 10.1063/1.1558224]

TABLE OF CONTENTS

FIG. 1. Comparison of D^* of various infrared detectors when operated at the indicated temperature. Chopping frequency is 1000 Hz for all detectors except the thermopile (10 Hz), thermocouple (10 Hz), thermistor bolometer (10 Hz), Golay cell (10 Hz), and pyroelectric detector (10 Hz). Each detector is assumed to view a surrounding hemisphere at a temperature of 300 K. Theoretical curves for the background-limited D^* for ideal photovoltaic and photoconductive detectors and thermal detectors are also shown.

I. INTRODUCTION

Since the initial proposal by Esaki and Tsu[1] and the advent of molecular beam epitaxy (MBE), interest in semiconductor superlattices (SL's) and quantum well (QW) structures has increased continuously over the years, driven by technological challenges and new physical concepts and phenomena as well as promising applications. A new class of materials and heterojunctions with unique electronic and optical properties has been developed. Here we focus on devices which involve infrared (IR) excitation of carriers in quantum wells. A distinguishing feature of QW infrared detectors is that they can be implemented in chemically stable wide-band-gap materials as a result of the use of intraband processes. Among the different types of quantum well infrared photodetectors (QWIP's), the technology of GaAs/AlGaAs multiple-quantum-well (MQW) detectors is the most mature.[2] Rapid progress has been made recently in the performance of these detectors. Detectivities have improved dramatically and they are now high enough for the fabrication of large (e.g., 640×486 and 640×512) focal plane arrays (FPA's) with a long-wavelength IR (LWIR) imaging performance comparable to that of state-of-the-art HgCdTe detectors.[3–5]

At present, HgCdTe is a variable-gap semiconductor most often used in the production of IR photodetectors. Over the last 40 years it has successfully fought off major challenges from extrinsic silicon and lead-tin telluride devices. Despite that, however, it has more competitors today than ever before. These include Schottky barriers on silicon, SiGe heterojunctions, AlGaAs multiple quantum wells, GaInSb strain layer superlattices, high-temperature superconductors, and especially two types of thermal detectors: pyroelectric detectors and silicon bolometers. It is interesting, however, that none of these is competitive in terms of fundamental properties. They may promise to be more easily manufactured, but never to provide higher performance or, with the exception of thermal detectors, to operate at higher or even comparable temperatures.
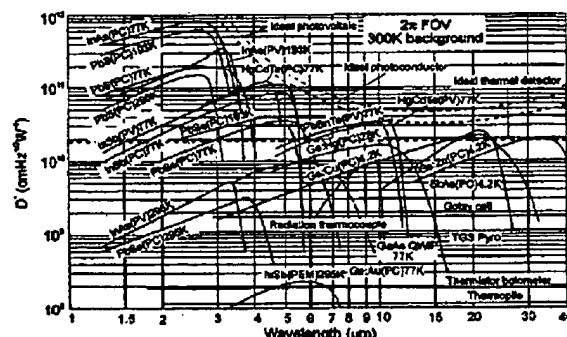
The main motivation to replace HgCdTe is the technological difficulties associated with this material. One of them is the weak Hg–Te bond resulting in bulk, surface, and interface instabilities. Uniformity and yield are still unresolved issues. Slow progress in the development of large photovoltaic HgCdTe infrared imaging arrays and the rapid achievements of novel semiconductor heterostructure systems have made it more difficult to predict what types of arrays will be readily available for future system applications. For space-borne surveillance systems, low-background IR seeker/tracker systems as well as reliable and affordable sensors with long life are needed which can function effectively at temperatures higher than 20–30 K currently required by bulk photon detectors. The only alternative to HgCdTe that has been available so far was extrinsic Si which operates at much lower temperatures where a problematic three-stage cryocooler would be required. Improvement in surveillance sensors and interceptor seekers requires highly uniform and multicolor (or multispectral) large-area IR FPA's operating in the LWIR and very-long-wavelength IR (VLWIR) regions. Among the competing technologies there are the QWIP's based on lattice matched GaAs/AlGaAs and strained layer InGaAs/AlGaAs material systems.

In this paper we discuss the performance of QWIP's as compared to other types of IR detectors including both photon and thermal detectors. As the QWIP detector is a photon detector, more attention is paid in our comparative studies to this family of detectors, especially to HgCdTe photodiodes. InSb photodiodes and doped silicon detectors are considered too. The potential performance of different materials is examined by utilizing the α/G ratio, where α is the absorption coefficient and G is the thermal generation rate.

The first part of the paper is devoted to different types of detectors operating as single devices. In the second part, such FPA issues as array size, uniformity, operability, multicolor capability, and system prices are discussed. The discussion is

TABLE I. Comparison of infrared detectors.

Detector type			Advantages	Disadvantages
Thermal (thermopile, bolometers, pyroelectric)			Light, rugged, reliable, and low cost Room temperature operation Easier to prepare More stable materials	Low detectivity at high frequency Slow response (ms order) Very high thermal expansion coefficient Large permittivity
Photon	Intrinsic	IV–VI (PbS, PbSe, PbSnTe)		
		II–VI (HgCdTe)	Easy band gap tailoring Well developed theory & expt. Multicolor detectors	Nonuniformity over large area High cost in growth and processing Surface instability
		III–V (InGaAs, InAs, InSb, InAsSb)	Good material and dopants Advanced technology Possible monolithic integration	Heteroepitaxy with large lattice mismatch Long wavelength cutoff limited to 7 μm (at 77 K)
	Extrinsic (Si:Ga, Si:As, Ge:Cu, Ge:Hg) Free carriers (PtSi, Pt₂Si, IrSi)		Very-long-wavelength operation Relatively simple technology Low-cost, high yields Large and close-packed 2D arrays Matured material growth	High thermal generation Extremely low-temperature operation Low quantum efficiency Low-temperature operation High thermal generation
	Quantum wells	Type I (GaAs/AlGaAs, InGaAs/AlGaAs)	Good uniformity over large area Multicolor detectors	Complicated design and growth
		Type II (InAs/InGaSb, InAs/InAsSb)	Low Auger recombination rate Easy wavelength control	Complicated design and growth Sensitive to the interfaces
	Quantum dots	InAs/GaAs, InGaAs/InGaP, Ge/Si	Normal incidence of light Low thermal generation	Complicated design and growth

mainly concentrated on two competitive technologies, QWIP and HgCdTe. In such a way, the paper attempts to settle the main issues of both technologies. To present the material more clearly for readers, many details are included in the Appendix.

II. FUNDAMENTAL LIMITS TO INFRARED DETECTOR PERFORMANCE

Spectral detectivity curves for a number of available IR detectors are shown in Fig. 1. The wavelengths of the two atmospheric windows, 3–5 μm [medium-wavelength IR (MWIR)] and 8–14 μm (LWIR), are the most interesting (atmospheric transmission is the highest in these windows and the room-temperature emissivity reaches its maximum at $\lambda \approx 10$ μm). It should be noted, however, that in recent years interest in longer wavelengths has been steadily increasing, stimulated by space applications.

Depending on the detection mechanisms, the nature of the interaction and material properties, various types of detectors have different characteristics. These characteristics result in advantages and disadvantages when the detectors are used in field applications.[6-9] Table I shows a comparison of various IR detectors.

In the class of photon detectors, radiation is absorbed within the material by means of interactions with free electrons or those bound either to lattice atoms or to impurity atoms. The observed electrical output signal results from the changed electron energy distribution. The response of photon detectors per unit incident radiation power depends selectively on wavelength. These detectors exhibit both perfect signal-to-noise performance and a very fast response. To achieve this, photon detectors require, however, cryogenic cooling. Photon detectors with long-wavelength limits exceeding approximately 3 μm are usually cooled. This is nec-

essary to prevent thermal generation of charge carriers. Thermal transitions compete with optical ones, making noncooled devices very noisy. Cooling is the main obstacle to a more widespread use of IR systems based on semiconductor photodetectors because it makes them bulky, heavy, expensive, and inconvenient to use.

Depending on the nature of the interaction, the class of photon detectors is further sub-divided into different types as shown in Table I. The most important are intrinsic detectors, extrinsic detectors, photoemissive (metal silicide Schottky barriers) detectors, and quantum well detectors. Depending on how the electric or magnetic fields are developed, there are various modes such as photoconductive, photovoltaic, photoelectromagnetic (PEM), and photoemissive ones. Each material system can be used in different modes of operation. In this paper, we focus on photodiodes and photoconductive detectors.

The second class of IR detectors is composed of thermal detectors. In a thermal detector the incident radiation is absorbed to change the temperature of the material, and the
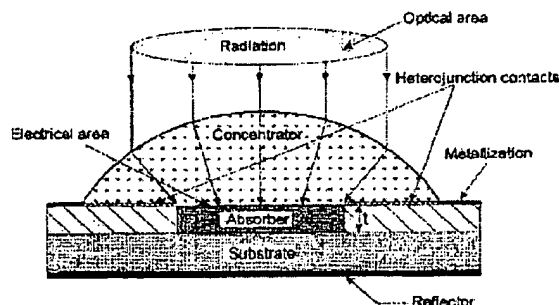

FIG. 2. Model of a photodetector.

resultant change in a certain physical property is used to generate an electrical output. The detector is suspended on legs which are connected to the heat sink. The signal does not depend upon the photonic nature of the incident radiation. Thus, thermal effects are generally wavelength independent; the signal depends upon the radiant power (or its rate of change) but not upon its spectral content. This would mean that the mechanism responsible for the absorption of radiation is itself wavelength independent, which is not strictly true in most cases. Three approaches are most widely applied in infrared technology: namely, bolometers, pyroelectric, and thermoelectric effects. In pyroelectric detectors, a change in the internal electrical polarization is measured, whereas in thermistor bolometers a change in the electrical resistance is measured. In contrast to photon detectors, thermal detectors typically operate at room temperature. They are usually characterized by modest sensitivity and slow response (because heating and cooling of the detector is a relatively slow process), but they are cheap and easy to use. They have found widespread use in low cost applications that do not require high performance and speed. Being unselective, they are frequently used in IR spectrometers. Uncooled FPA's fabricated currently from thermal detectors have revolutionized the development of thermal imagers.[10,11]

A. General theory of photon detectors

A photodetector is a slab of homogeneous semiconductor with an actual "electrical" area A_e. It is coupled to a beam of infrared radiation by its optical area A_o (Fig. 2). Usually, the optical and electrical areas of the device are the same or close to each other. The use of optical concentrators may increase the A_o/A_e ratio.

The current responsivity of a photodetector is determined by the quantum efficiency η and by the photoelectric gain g. The quantum efficiency value describes how well the detector is coupled to the radiation to be detected. It is usually defined as the number of electron-hole pairs generated per incident photon. The idea of photoconductive gain g was put forth by Rose[12] as a simplifying concept for the understanding of photoconductive phenomena and is now widely used in the field. The photoelectric gain is the number of carriers crossing the contacts per generated pair and it is defined simply as the ratio of the photoelectron lifetime to the transit time. This value shows how well the generated electron-hole pairs are used to generate the current response of a photodetector. Both η and g are assumed here to be constant over the volume of the device.

The spectral current responsivity is equal to

$$R_i = \frac{\lambda \eta}{hc} q g, \tag{1}$$

where λ is the wavelength, h is Planck's constant, c is the light velocity, and q is the electron charge. Assuming that the current gain for photocurrent and noise current is the same, the current noise due to the generation and recombination processes is[12]

$$I_n^2 = 2(G+R)A_e t \Delta f q^2 g^2, \tag{2}$$

where G and R are the generation and recombination rates, Δf is the frequency band, and t is the thickness of the detector.

The detectivity D^* is the main parameter characterizing the normalized signal-to-noise performance of detectors and can be defined as

$$D^* = \frac{R_i (A_o \Delta f)^{1/2}}{I_n}. \tag{3}$$

According to Eqs. (1)–(3),[13]

$$D^* = \frac{\lambda}{hc} \left(\frac{A_o}{A_e}\right)^{1/2} \eta [2(G+R)t]^{-1/2}. \tag{4}$$

For a given wavelength and operating temperature, the highest performance can be obtained by maximizing $\eta/[t(G+R)]^{1/2}$ which corresponds to the condition of the highest ratio of the sheet optical generation to the square root of sheet thermal generation and recombination. This means that high quantum efficiency must be obtained in a thin device. For a given wavelength and operating temperature, the performance may be increased by reducing the total number of generation and recombination acts which is $(G+R) \times (A_e t)$.

In further considerations we put $A_o/A_e = 1$. Assuming a single pass of the radiation and negligible frontside and backside reflection coefficients, the quantum efficiency and detectivity are

$$\eta = 1 - \exp(-\alpha t), \tag{5}$$

$$D^* = \frac{\lambda}{hc}(1 - e^{-\alpha t})[2(G+R)t]^{-1/2}, \tag{6}$$

where α is the absorption coefficient.

The highest detectivity is obtained for $t = 1.26/\alpha$. For this condition $(1 - e^{\alpha t})t^{-1/2}$ reaches its maximum of $0.62 \alpha^{1/2}$. This thickness is the best compromise between the requirements of high quantum efficiency and low thermal generation. In this optimum case $\eta = 0.716$ and detectivity is equal to[13]

$$D^* = 0.45\frac{\lambda}{hc}\left(\frac{\alpha}{G+R}\right)^{1/2}. \tag{7}$$

At equilibrium, the generation and recombination rates are equal to each other, and we have

$$D^* = 0.31\frac{\lambda}{hc}\left(\frac{\alpha}{G}\right)^{1/2}. \tag{8}$$

Considerations presented in Ref. 13 indicate

$$D^* = 0.31\frac{\lambda}{hc}k\left(\frac{\alpha}{G}\right)^{1/2}, \tag{9}$$

where $1 \leq k \leq 2$, and k is dependent on the contribution of recombination and backside reflection.

The ratio of the absorption coefficient to the thermal generation rate, α/G, is the fundamental figure of merit of any material intended for infrared photodetectors. It determines directly the detectivity limits of the devices. This figure should be used to assess any potential material.

An optimized photodetector should consist of the following:[14]

(i) A lightly doped active (base) region, which acts as an absorber of IR radiation. Its band gap, doping, and geometry should be precisely selected. The surface of the active region must be insulated from the ambient by a material that does not contribute to the generation of carriers; in addition, the carriers which are optically generated in the absorber should be kept away from the surfaces where recombination can reduce the quantum efficiency.

(ii) Electric contacts to the base region which sense optically generated charge carriers and should not contribute to the dark current of the device,

(iii) A backside mirror for double pass of IR radiation.

The above conditions may be fulfilled by using heterojunctions like N^+-p-p^+ and P^+-n-n^+ with heavily doped contact regions (symbol "+" denotes strong doping; capital letter, wider gap). Homojunction devices (like $n-p$, n^+-p, p^+-n) suffer from surface problems; excess thermal generation results in increased dark current and recombination, which in turn, reduce the photocurrent.

The total generation rate is the sum of the optical and thermal generation rates

$$G = G_{th} + G_{op}. \tag{10}$$

To achieve high performance, thermal generation must be suppressed to the lowest level possible. This is usually done with cryogenic cooling. For practical purposes, the ideal situation occurs when thermal generation is reduced below optical generation. The requirements for the thermal generation rate may be highly reduced in heterodyne systems, in which optical excitation by the local oscillator can dominate the generation, even in conditions of high thermal generation. Optical generation may be due to the signal or background radiation. For infrared detectors, background radiation is usually higher compared to signal radiation. If thermal generation is reduced much below the background level, the performance of the device is determined by the background radiation (BLIP conditions for background limited infrared photodetector). This condition may be described as

$$\frac{\eta \Phi_B \tau}{t} > n_{th}, \tag{11}$$

where n_{th} is the density of thermal carriers at temperature T, τ is the carrier lifetime, and Φ_B is the total background photon flux density (unit $cm^{-2} s^1$) reaching the detector. Rearranging Eq. (11) we obtain the BLIP requirements

$$G_{op} = \frac{\eta \Phi_B}{t} > \frac{n_{th}}{\tau} = G_{th}; \tag{12}$$

i.e., the photon generation rate needs to be greater than the thermal generation rate. Either majority or minority carriers can be considered.

The direct band gap semiconductor photodiode is a minority carrier device and in thermal equilibrium

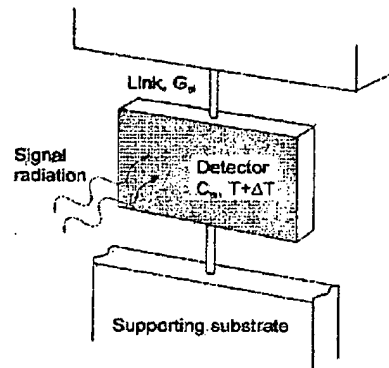$$n_{min} = \frac{n_i^2}{n_{maj}}, \tag{13}$$

FIG. 3. Thermal detector mounted via legs to heat sink.

where n_i is the intrinsic carrier concentration and n_{maj} is the majority carrier concentration. The ultimate limit on carrier lifetime in a direct gap semiconductor is given by band-to-band recombination, by either radiative or Auger processes. Humphreys indicated[15] that the van Roosbroeck–Shockley theory of radiative recombination underestimates the radiative lifetime due to noiseless photon reabsorption. As a result, Auger recombination is the dominant process in narrow gap semiconductors like HgCdTe ternary alloy, for example.

The extrinsic semiconductor photoconductor is strictly a majority carrier device.

The background limited detectivity or, the so-called, "photovoltaic" BLIP detectivity is given by[16,17]

$$D_{BLIP}^* = \frac{\lambda}{hc} \left(\frac{\eta}{2\Phi_B} \right)^{1/2}. \tag{14}$$

D_{BLIP}^* for photoconductors is $\sqrt{2}$ times lower that for photodiodes. This is attributable to the recombination process in photoconductors which is uncorrelated with the generation process contributing to the detector noise. The background photon flux density received by the detector depends on its angular field of view (FOV) of the background and on its ability to respond to the wavelengths contained in the source. Plots of D_{BLIP}^* as a function of wavelength for $T_{BLIP} = 300$ K and for full 2π FOV are shown in Fig. 1.

B. General theory of thermal detectors

Thermal detectors operate on the simple principle that, when heated by incoming IR radiation, their temperature increases and the temperature changes are measured by any temperature-dependent mechanism such as thermoelectric voltage, resistance, and pyroelectric voltage. The simplest representation of the thermal detector is shown in Fig. 3. The detector with the emissivity ϵ is represented by a thermal capacitance C_{th} coupled via thermal conductance G_{th} to a heat sink at a constant temperature T. In the absence of a radiation input, the average temperature of the detector will also be T, although it will exhibit fluctuations around this value. When a radiation input is received by the detector, the temperature rise is found by solving the heat balance equa-

A. Rogalski

tion. Assuming the radiant power to be a periodic function, the change in the temperature of any thermal detector due to the incident radiative flux is[16,18]

$$\Delta T = \frac{\epsilon \Phi_o}{(G_{th}^2 + \omega^2 C_{th}^2)^{1/2}}. \tag{15}$$

Equation (15) illustrates several features of thermal detectors. Clearly it is advantageous to make ΔT as large as possible. To do this, the thermal capacity of the detector (C_{th}) and its thermal coupling to its surroundings (G_{th}) must be as small as possible. The interaction of the thermal detector with the incident radiation should be optimized while reducing, as far as possible, all other thermal contacts with its surroundings. This means that a small detector mass and fine connecting contacts to the heat sink are desirable.

The characteristic thermal response time of a detector may be defined as

$$\tau_{th} = \frac{C_{th}}{G_{th}} = C_{th} R_{th}, \tag{16}$$

where $R_{th} = 1/G_{th}$ is the thermal resistance.

The values of the thermal time constant are typically in the millisecond range. This is much longer than the typical time of a photon detector. There is a trade-off between sensitivity ΔT and frequency response. If one wants a high sensitivity, a low-frequency response is then forced upon the detector.

For further discussion we introduce the coefficient $K = \Delta V/\Delta T$ that reflects the efficiency with which the temperature changes translate into the electrical output voltage of a detector.

The voltage responsivity R_v of the detector is the ratio of the output signal voltage ΔV to the input radiation power and is given by

$$R_v = \frac{K \epsilon R_{th}}{(1 + \omega^2 \tau_{th}^2)^{1/2}}. \tag{17}$$

In order to determine the detectivity of the detector, the noise mechanism must be known first. The Johnson noise is one of the major noises. Two other fundamental noises are important for assessing the ultimate performance of a detector, namely the thermal fluctuation noise and the background fluctuation noise.

The thermal fluctuation noise arises from temperature fluctuations in the detector. These fluctuations are caused by heat conductance variations between the detector and the surrounding substrate with which the detector is in thermal contact.

The spectral noise voltage due to temperature fluctuations is[16,18]

$$V_{th}^2 = \frac{4kT^2 \Delta f}{1 + \omega^2 \tau_{th}^2} K^2 R_{th}. \tag{18}$$

The third noise is the background noise resulting from radiative heat exchange between the detector at temperature
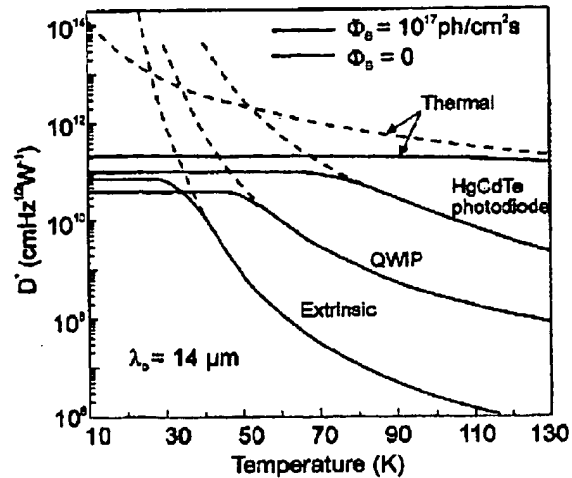

FIG. 4. Theoretical performance limits of LWIR photon and thermal detectors at zero background and background of 10[17] photons/cm^{2} s, as a function of detector temperature (after Ref. 19).

T_d and the surrounding environment at temperature T_b. It is the ultimate limit of a detector's performance capability and for a 2π FOV is given by[16,18]

$$V_b^2 = \frac{8k\epsilon\sigma A (T_d^2 + T_b^2)}{1 + \omega^2 \tau_{th}^2} K^2 R_{th}, \tag{19}$$

where σ is the Stefan–Boltzmann constant.

The fundamental limit of the sensitivity of any thermal detector is determined by the temperature fluctuation noise, i.e., random fluctuations of the detector temperature due to the fluctuations of the radiant power exchange between the detector and its surroundings. Under this condition we have at low frequencies ($\omega \ll 1/\tau_{th}$)

$$D_{th}^* = \left(\frac{\epsilon^2 A}{4kT_d^2 G_{th}} \right)^{1/2}. \tag{20}$$

It is assumed here that ϵ is independent of the wavelength, so that the spectral D_λ^* and blackbody $D^*(T)$ values are identical.

If the radiant power exchange is the dominant heat exchange mechanism, then G is the first derivative of the Stefan–Boltzmann function with respect to temperature. In that case, known as the background fluctuation noise limit, we have

$$D_b^* = \left[\frac{\epsilon}{8k\sigma(T_d^5 + T_b^5)} \right]^{1/2}. \tag{21}$$

Note that D_b^* is, as expected, independent of A.

Equations (20) and (21) assume that the detector receives the background radiation from all directions when the temperature of the detector and background are equal, and from the forward hemisphere only when the detector is at cryogenic temperatures. The highest possible D^* to be expected for a thermal detector operating at room temperature and viewing a background at room temperature is 1.98

$\times 10^{10}$ cm Hz$^{1/2}$ W^{-1}. Even if either the detector or background were cooled to absolute zero, the detectivity would improve only by the square root of two. This is the basic limitation of all thermal detectors. Photon detectors limited by background noise have higher detectivities as a result of their limited spectral responses.

The performance achieved by any real detector will be inferior to that predicted by Eq. (21). The degradation of performance will arise from (i) encapsulation of the detector (reflection and absorption losses at the window), (ii) effects of excess thermal conductance (influence of electrical contacts, conduction through the supports, influence of any gas: conduction and convection), or (iii) additional noise sources.

Typical values of the detectivities of thermal detectors at 10 Hz range from 10^8 to 10^9 cm Hz$^{1/2}$ W^{-1}.

C. Comparison of the fundamental limits of thermal and photon detectors

The temperature dependence of the fundamental limits of D^* of photon and thermal detectors at different levels of background are shown in Fig. 4. As seen the performance of intrinsic IR detectors (HgCdTe photodiodes) in the LWIR spectral range is higher than that of other types of photon detectors. HgCdTe photodiodes with a background limited performance operate at temperatures below ~80 K. HgCdTe is characterized by a high optical absorption coefficient and quantum efficiency and a relatively low thermal generation rate compared to QWIP's and extrinsic silicon detectors. Both QWIP and silicon detectors are extrinsic in their character and require more cooling than intrinsic photon detectors having the same long-wavelength limit.

The ultimate detectivity value for thermal detectors is much less temperature dependent than for photon detectors. At temperatures below 50 K and zero background, LWIR thermal detectors are characterized by D^* values lower that those of LWIR photon detectors. However, at temperatures above 60 K, thermal detectors perform better than photon ones. At room temperature, the performance of thermal detectors is much better than that of LWIR photon detectors. It is due to the influence of the fundamentally different types of noise (generation-recombination noise in photon detectors and temperature fluctuation noise in thermal detectors) that the dependences of the detectivity on the wavelength and temperature are different in these two classes of detectors. Photon detectors exhibit better performance at long-wavelength infrared radiation and lower operating temperatures. Thermal detectors perform better in the very-long-wavelength spectral range. The temperature requirements to attain the background-fluctuation-noise-limited performance, in general, favor thermal detectors at higher cryogenic temperatures and photon detectors at lower cryogenic temperatures.

The above relations, which are shown in Fig. 4 for a background of 10^{17} photons/cm^2 s, are modified by the influence of the background. It is interesting to note that in this case the theoretical curves of D^* for photon and thermal detectors show similar fundamental limits at low temperatures.
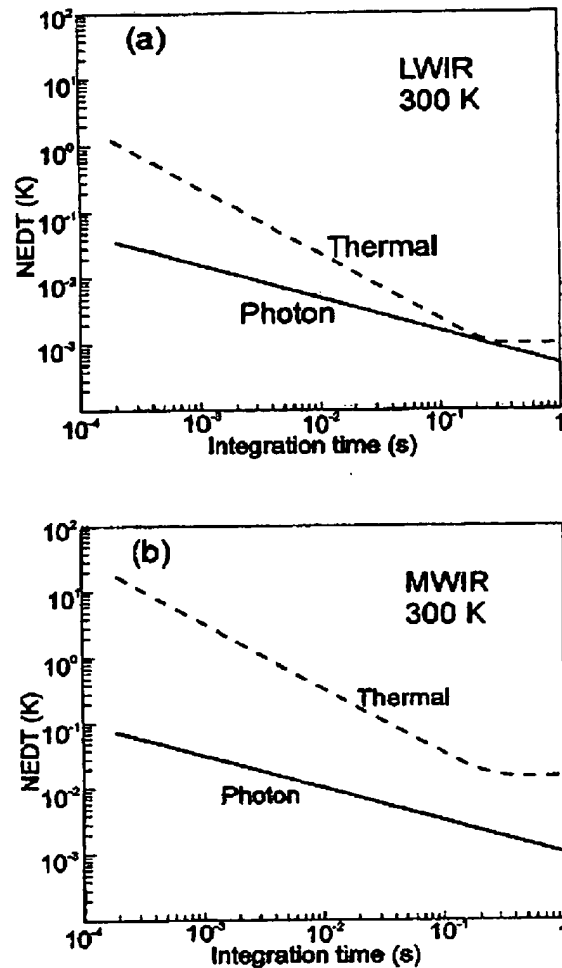

FIG. 5. Theoretical NEDT comparison of uncooled thermal and HgCdTe uncooled photon LWIR (a) and MWIR (b) detectors (after Ref. 20).

The relevant figure of merit for FPA's is the noise equivalent difference temperature (NEDT), which is the temperature change of a scene required to produce a signal equal to the rms noise (see Appendix A1). It is of interest to compare the performance of uncooled photon and thermal detectors in the MWIR ($\lambda = 5$ μm) and LWIR ($\lambda = 10$ μm) spectral range. We have followed the procedure used in a paper recently published by Kinch.[20]

Figure 5 compares the theoretical NEDT of detectors operating at 290 K for F/1 optics and a 1 mil pixel size. Parameter values typical of micromachined resonant cavity bolometers given in Appendix A1 are assumed in the calculations. A $N^+ - \pi - P^+$ HgCdTe photodiode, first proposed by Elliott and Ashley,[21] is chosen as a photon detector. The symbol π designates an intrinsic region containing a p-type background dopant concentration of 5×10^{14} cm^{-3} with carrier lifetime limited by the Auger 7 process. It is also assumed that the detector node capacity is capable of storing the inte-

TABLE II. Essential properties of LWIR HgCdTe photodiodes and QWIP's at $T = 77$ K.

Parameter	HgCdTe	QWIP (n-type)
IR absorption	Normal incidence	$E_{optical} \perp$ plane of well required Normal incidence: no absorption
Quantum efficiency	$\geqslant 70\%$	$\leqslant 10\%$
Spectral sensitivity	Wide-band	Narrow-band (FWHM ≈ 1–2 μm)
Optical gain	1	0.4 (30–50 wells)
Thermal generation lifetime	≈ 1 μs	≈ 10 ps
$R_0 A$ product ($\lambda_c = 10$ μm)	300 Ω cm^2	10^4 Ω cm^2
Detectivity ($\lambda_c = 10$ μm, FOV=0)	2×10^{12} cm Hz$^{1/2}$ W^{-1}	2×10^{10} cm Hz$^{1/2}$ W^{-1}

grated charge provided by the detector dark current.

Figure 5 shows that the ultimate performance of un-cooled HgCdTe photon detectors is far superior to that of thermal detectors at wide frame rates and spectral bands. Also any other tunable band gap alloy, such as type-II InAs/GaInSb superlattices, could be useful in the development of uncooled photon detector technology.[6,22] The ultimate performance of InAs/InGaSb strain layer superlattice photodiodes with optimally doped base regions is comparable with that of HgCdTe photodiodes in the temperature range between 300 K and 77 K.[23]

Comparing both curves for thermal detectors in Fig. 5, we can see that for long integration times excellent performance can be achieved in the LWIR region with NEDT values below 10 mK for frame rates of 30 Hz. However, for snapshot systems with an integration time below 2 ms, the available NEDT is above 100 mK even in the LWIR region. In the MWIR band thermal detectors has obvious performance limitations at any frame rate.

III. QWIP's VERSUS OTHER TYPES OF INFRARED PHOTODETECTORS

Current-cooled IR detector systems use materials such as HgCdTe, InSb, PtSi, and doped Si. As far as IR applications are concerned, QWIP is a relatively new technology. The first GaAs/AlGaAs QWIP was demonstrated by Levine et al.[24] in 1987. Among these cooled IR detector systems, PtSi FPA's are highly uniform and easy to manufacture but they have very low quantum efficiency and can only operate in the MWIR range. The InSb FPA technology is mature with very high sensitivity and it also can operate in the MWIR spectral range. Doped Si has a wide spectral range from 0.8 to 30 μm and operates only at very low temperatures. PtSi, InSb, and doped Si detectors do not have wavelength tunability or multicolor capabilities. Both QWIP's and HgCdTe offer high sensitivity together with wavelength flexibility in the MWIR, LWIR, and VLWIR regions, as well as multi-color capabilities. HgCdTe can also operate in the short-

TABLE III. HgCdTe photodiode architectures used for hybrid FPA's (after Ref. 25).

| Configuration	Junction formation	Company
n-on-p VIP	Ion implantation forms n-on-p diode in p-type HgCdTe, grown by Te-solution LPE on CdZnTe and epoxied to silicon ROIC wafer; over the edge contact	DRS Infrared Technologies (formerly Texas Instruments)
n-p loophole	Ion beam milling forms n-type islands in p-type Hg-vacancy-doped layer grown by Te-solution LPE on CdZnTe, and epoxied onto silicon ROIC wafer; cylindrical lateral collection diodes	GEC-Marconi Infrared (GMIRL)
n^+-on-p planar	Ion implant into acceptor-doped p-type LPE film grown by Te-solution slider	Sofradir (Societe Francaise de Detecteurs Infrarouge)
n^+-n^--p planar homojunctions	Boron implant into Hg-vacancy p-type, grown by Hg-solution tipper on 3" diam. sapphire with MOCVD CdTe buffer; ZnS passivation	Rockwell/Boeing
P-on-n mesa	1. Two-layer LPE on CdZnTe: Base: Te-solution slider, indium-doped Cap: Hg-solution dipper, arsenic-doped 2. MOCVD in situ on CdZnTe Iodine-doped base, arsenic-doped cap	IR Imaging Systems, Sanders – A Lockheed Martin Company (LMIRIS)
P-on-n mesa	1. Two-layer LPE on CdZnTe or Si: Base: Hg-solution dipper, indium-doped Cap: Hg-solution dipper, arsenic-doped 2. MBE in situ on CdZnTe or Si Indium-doped base, arsenic-doped cap	Raytheon Infrared Center of Excellence (RIRCoE, formerly SBRC) and Hughes Research Laboratories (HRLs)
P-on-n planar buried heterostructure	Arsenic implant into indium-doped N-n or N-n-N film grown by MBE on CdZnTe	Rockwell/Boeing
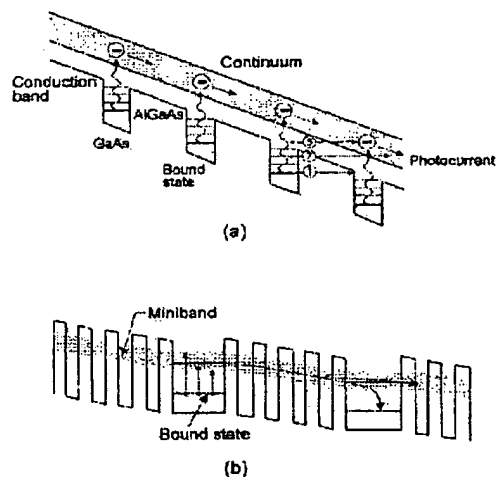
FIG. 6. Band diagram of demonstrated QWIP structures: (a) bound-to-extended and (b) bound-to-miniband. Three mechanisms creating dark current are also shown in (a): ground-state sequential tunneling (1), intermediate thermally assisted tunneling (2), and thermionic emission (3). The gray shading indicates extended states through which current flows.

FIG. 7. Absorption coefficient for various photodetector materials in spectral range of 1–14 μm.

wavelength IR (SWIR) region, while QWIP has to go to a direct band-to-band scheme for SWIR operation. Table II compares the essential properties of HgCdTe and QWIP devices at 77 K.

Different HgCdTe photodiode architectures have been fabricated that are compatible with backside and frontside illuminated hybrid FPA technology. The most important architectures are included in Table III which summarizes the applications of HgCdTe photodiode designs by the major FPA manufactures today.

All QWIP's are based on "band gap engineering" of layered structures of wide-band-gap (relative to thermal IR energies) materials. These structures are designed in such a way that the energy separation between two selected states in the structure matches the energy of the infrared photons to be detected. Several QWIP configurations have been reported based on transitions from bound-to-extended states, bound-to-quasicontinuum states, bound-to-quasibound states, and bound-to-miniband states.

Figure 6 shows two detector configurations used in the fabrication of two-color QWIP FPA's. The major advantage of the bound-to-continuum QWIP [Fig. 6(a)] is that the photoelectron can escape from the quantum well to the continuum transport states without being required to tunnel through a barrier. As a result, the voltage bias required to efficiently collect the photoelectrons can be reduced dramatically, thereby lowering the dark current. Furthermore, since photoelectrons do not have to tunnel through them, the AlGaAs barriers can be made thicker without reducing the photoelectron collection efficiency. It appears that the dark current decreases significantly when the first excited state is dropped from the continuum to the well top, bound-to-quasibound QWIP, without sacrificing the responsivity.
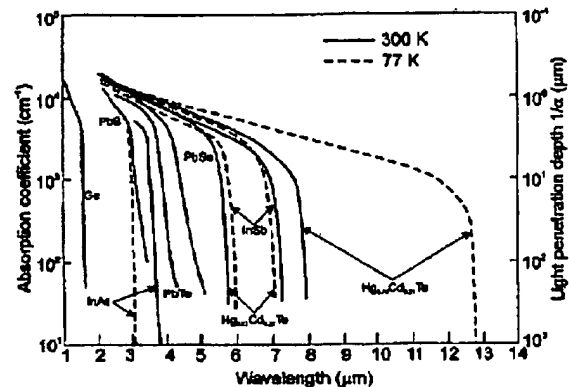
A miniband transport QWIP contains two bound states with the higher energy level being resonant with the ground state miniband in the superlattice barrier [see Fig. 6(b)]. In this approach, IR radiation is absorbed in the doped quantum wells, exciting an electron into the miniband and transporting it along the miniband until it is collected or recaptured into another quantum well. Thus, the operation of this miniband QWIP is analogous to that of a weakly coupled MQW bound-to-continuum QWIP. In this device structure, the continuum states above the barriers are replaced by a miniband of superlattice barriers. The miniband QWIP's show a lower photoconductive gain than bound-to-continuum QWIP's because photoexcited electron transport occurs in the miniband where electrons have to be transported through many thin heterobarriers resulting in a lower mobility.

The light-coupling scheme is a key factor in QWIP FPA performance. Different light-coupling mechanisms are used in QWIP's. A distinct feature of n-type QWIP's is that the optical absorption strength is proportional to an incident photon's electric-field polarization component normal to the quantum wells. This implies that a photon propagating in the direction normal to the quantum wells, whose polarization is entirely in the plane of the quantum wells, is not absorbed. Therefore, these detectors have to be illuminated through a 45° polished facet. For imaging, it is necessary to be able to couple light uniformly to two-dimensional (2D) arrays of these detectors, so a diffraction periodic grating[26] or other similar structure (such as random reflectors,[27] corrugated reflectors,[28] lattice mismatch strain material systems, and p-type materials[29]) is typically fabricated on one side of the detector to redirect a normally incident photon into propagation angles more favorable for absorption.

Kinch and Yariv[30] presented the first investigation ever of the fundamental physical limitations of individual multiple-quantum-well IR detectors as compared to ideal HgCdTe detectors at $\lambda_c = 8.3$ μm and 10 μm. The dark current in the QWIP is typically four to five orders of magnitude higher than in a direct-gap semiconductor with the same band gap and operating at the same temperature. For tactical background fluxes, this enables the operation of a direct-gap
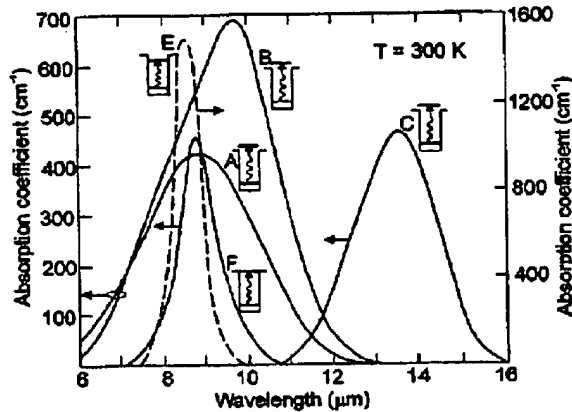
FIG. 8. Absorption coefficient spectra measured at $T=300$ K for different QWIP samples described in Table III.

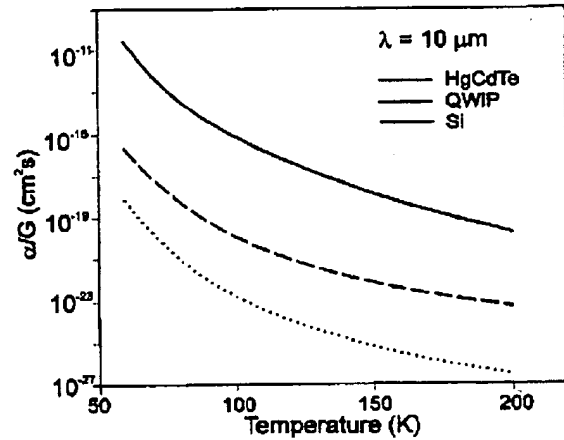

FIG. 9. α/G ratio versus temperature for LWIR ($\lambda_c = 10$ μm) photon detectors.

semiconductor at temperatures about 50° higher while offering the same performance as the QWIP. This issue can be alleviated somewhat by the use of resonant structures, which enable IR absorption for significantly thinner QWIP's at the expense of band spectral response, but the improvement is minimal. The dominant factor favoring HgCdTe in this comparison is the excess carrier lifetime, which for n-type HgCdTe is above 1 μs at 80 K, compared to about 10 ps for the AlGaAs/GaAs superlattice. Several other papers[20,31-34] have been devoted to this issue.

A. α/G_{th} ratio

The considerations presented in Sec. II A indicate that the ratio of the absorption coefficient to the thermal generation rate, α/G_{th}, is the fundamental figure of merit of any material intended for IR photodetectors because it directly determines the detectivity limits of the devices.

Figure 7 shows measured intrinsic absorption coefficients for various narrow-gap photodetector materials. The absorption coefficient and the corresponding penetration depth vary among different semiconductor materials. It is well known that the absorption curve for direct transitions between parabolic bands at a photon energy higher than the energy gap, E_g, obeys a square-root law

$$\alpha(h\nu) = \beta(h\nu - E_g)^{1/2}, \tag{22}$$

where β is a constant. As seen in Fig. 7, the absorption edge

value in the MWIR spectral region is between 2×10^3 cm^{-1} and 3×10^3 cm^{-1}; in the LWIR region it is about 10^3 cm^{-1}.

Since α is a strong function of the wavelength, the wavelength range in which an appreciable photocurrent can be generated is limited for a given semiconductor. Near the material's band gap, there is tremendous variation causing a three order of magnitude variation in absorption. In the region of the material's maximum usable wavelength the absorption efficiency drops dramatically. For wavelengths longer than the cutoff wavelength, the values of α are too small to give appreciable absorption.

Figure 8 shows the infrared absorption spectra obtained from different n-doped, 50-period GaAs/Al$_x$ Ga$_{1-x}$As QWIP structures. The measurements were carried out at room temperature using a 45° multipass waveguide geometry. The spectra of bound-to-bound continuum (B-C) QWIP's (samples A, B, and C) are much broader than those of bound-to-bound (B-B) (sample E) or bound-to-quasibound (B-QB) QWIP's (sample F). Correspondingly, the value of the absorption coefficient of B-C QWIP's is significantly lower than that of B-B QWIP's. This is due to the conservation of oscillator strength. The values of the absorption coefficient at 77 K, peak wavelength λ_p, cutoff wavelength λ_c, and spectral width $\Delta\lambda$ (full width at half-α_p) are given in Table IV. It appears that the low-temperature absorption coefficient $\alpha_p(77$ K$) \sim 1.3\alpha_p(300$ K$)$ and α_p $(\Delta\lambda/\lambda)/N_D$ is a constant

TABLE IV. Structure parameters for different n-doped, 50-period Al$_x$Ga$_{1-x}$As QWIP structures (after Ref. 2).

Sample	Well width (Å)	Barrier width (Å)	Composition x	Doping density (10^{18} cm^{-3})	Intersubband transition	λ_p (μm)	λ_c (μm)	$\Delta\lambda$ (μm)	$\Delta\lambda/\lambda$ (%)	$\alpha_p(77$ K$)$ (cm^{-1})	$\eta_a(77$ K$)$ (%)
A	40	500	0.26	1.0	B-C	9.0	10.3	3.0	33	410	13
B	40	500	0.25	1.6	B-C	9.7	10.9	2.9	30	670	19
C	60	500	0.15	0.5	B-C	13.5	14.5	2.1	16	450	14
E	50	500	0.26	0.42	B-B	8.6	9.0	0.75	9	1820	20
F	45	500	0.30	0.5	B-QB	7.75	8.15	0.85	11	875	14
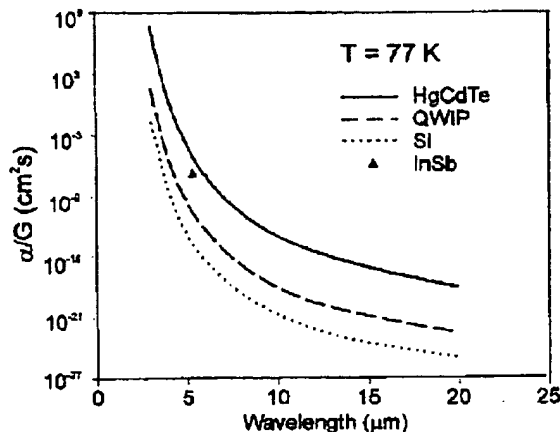
FIG. 10. α/G ratio versus cutoff wavelength for different types of photon detectors operated at 77 K.

FIG. 12. Current-voltage characteristics at various temperatures for a 12 μm cutoff HgCdTe photodiode (after Ref. 38).

(N_D is the well's doping).[2] Typical values of the absorption coefficient in the LWIR region are between 600 and 800 cm^{-1} at 77 K. Comparing Figs. 7 and 8 one may notice that the absorption coefficients for direct band-to-band absorption are higher than those for intersubband transitions.

The α/G ratio versus temperature is shown in Fig. 9 for different types of tunable materials with the hypothetical energy gap equal to 0.124 eV ($\lambda = 10$ μm). The procedures used in the calculations of α/G for different materials are given in Appendixes A2–A5. It is apparent that HgCdTe is by far the most efficient detector of IR radiation. One may also notice that QWIP is a better material than extrinsic silicon. Figure 9 is complimented by Fig. 10, where the α/G ratio in different materials is presented as a function of the wavelength at 77 K.

B. Quantum efficiency

HgCdTe has a direct-band-gap energy that translates to high radiative efficiency and may be tailored to absorb IR radiation at a wavelength of interest. When operating in the photovoltaic mode, the optical gain is close to unity and the responsivity is directly proportional to the quantum efficiency [see Eq. (1)] of the photodiode. In this section η is
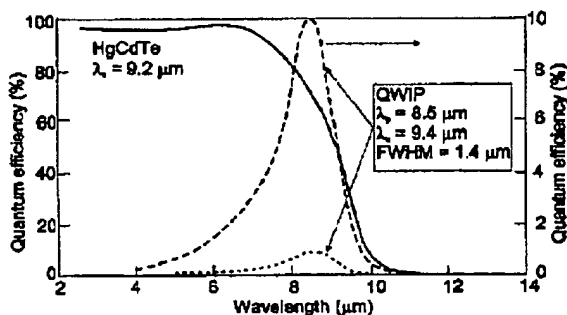

FIG. 11. Quantum efficiency versus wavelength for a HgCdTe photodiode and GaAs/AlGaAs QWIP detector with similar cutoffs.
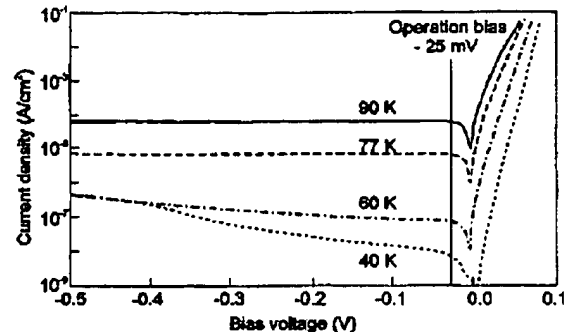
defined as the ratio of the number of photoexcited electrons collected by the readout integrated circuit (ROIC) to the number of photons incident at a detector surface. HgCdTe has high optical absorption and a wide absorption band irrespective of the polarization of the radiation, which greatly simplifies the detector array design. The quantum efficiency obtained routinely is around 70% without an antireflection (AR) coating and is in excess of 90% with an AR coating. Moreover, it is independent of the wavelength over the range from less than 1 μm to near the cutoff of the detector. The wide-band spectral sensitivity with a near-perfect η enables greater system collection efficiency and a smaller aperture to be obtained. This makes FPA's useful for imaging, spectral radiometry, and long-range target acquisition. It should be noticed, however, that the current LWIR staring array performance is mostly limited by the charge handling capacity of the ROIC and the background (warm optics).

Due to intersubband transitions in the conduction band, the n-type QWIP detection mechanism requires photons with a non-normal angle of incidence to provide proper polarization for photon absorption. The absorption quantum efficiency is relatively small (about 25%) with a 2D grating. Since QWIP is a photoconductive detector, the responsivity is proportional to the conversion efficiency—that is, the product of the absorption quantum efficiency and the optical gain. The optical gain of typical QWIP structures varies from 0.2 (in the case of 30–50 wells) to more than 1. This indicates that η is typically below 10% at the maximum response, rapidly falling off in the direction of both short and long wavelengths. Figure 11 compares the spectral η of a HgCdTe photodiode to that of a QWIP. A higher bias voltage is used to boost η. However, an increase in the reverse bias voltage also causes an increase of the leakage current. This limits any potential improvement in the system performance. New grating designs are under study to improve η, such as an enhanced QWIP, antenna gratings, and corrugated gratings.[3,4,32]

The strong dependence of the LWIR QWIP signal (and a weaker, but still significant dependence of the MWIR signal) on the polarization of the light is very important in future reconnaissance systems, because it offers the capability of discriminating between different polarization states.[35] The
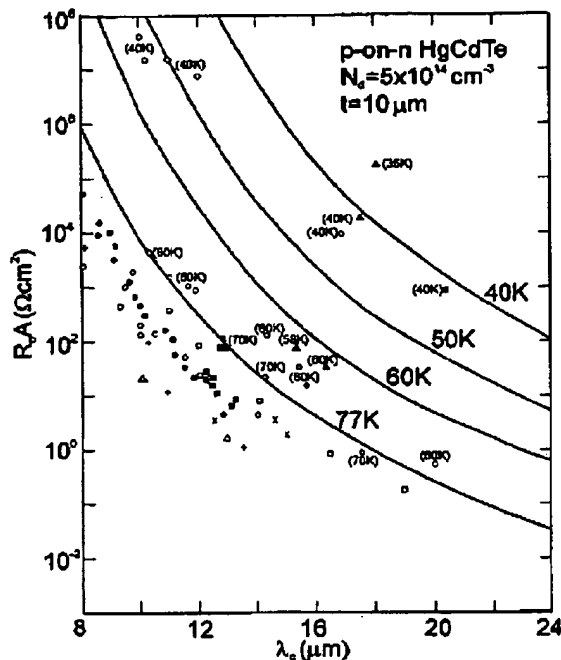
A. Rogalski

FIG. 13. Dependence of the R_0A product on the long wavelength cutoff for LWIR p-on-n HgCdTe photodiodes at temperatures $\leq$77 K. The solid lines are calculated on the assumption that the performance of photodiodes is due to thermal generation governed by the Auger mechanism in the base n-type region of photodiodes with thickness $t=10$ μm and doping $N_d=5\times10^{14}$ cm^{-3}. The experimental values are taken from different papers (after Ref. 39).

FIG. 14. Detailed analysis separates the cumulative distribution function of R_0A values of LWIR p-on-n HgCdTe photodiodes (fabricated by LPE) into three regions: good diodes, diodes affected by point defects, and diodes affected by metallurgical defects (after Ref. 42).

first polarization sensitive QWIP thermal imager has been assembled.[36]

It should be stressed that, so far, most efforts in the area of QWIP's are focused on tactical applications, where the structure designs and the doping are optimized to increase the operating temperature and suit the readout charge handling capacity. It is well known that using a smaller number of quantum wells and bound-to-continuum structures, increased optical gain and improved detector performance at low temperatures are possible. Tidrow presented[37] a high-performance QWIP consisting of only three quantum wells with the conversion efficiencies up to 29% at a bias voltage of −0.8 V and a peak wavelength of 8.5 μm.

C. Dark current and R_0A product

In ideal photodiodes the diffusion current is dominant, therefore their leakage current is very low and insensitive to the detector bias. Leakage current is the primary contribution of unwanted noise. Figure 12 shows typical current-voltage characteristics of a HgCdTe photodiode at temperatures between 40 and 90 K for a 12 μm cutoff detector at 40 K. The leakage current is less than 10^{-5} A/cm^2 at 77 K. The bias-independent leakage current makes it easier to achieve better FPA uniformity, as well as to reduce the detector bias-control requirements during changes in photocurrent.
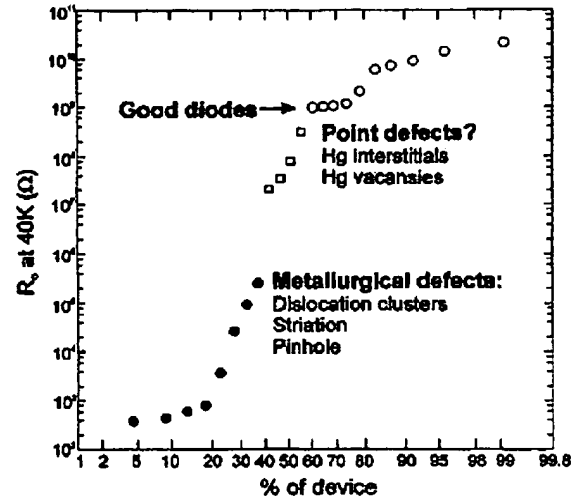
The dependence of the base region diffusion limited R_0A product on the long-wavelength cutoff for p-on-n HgCdTe photodiodes at temperatures $\leq$77 K is shown in Fig. 13. The solid lines are calculated by assuming that the performance of the photodiodes is determined by thermal generation governed by the Auger mechanism in the n-type base region with a thickness $t=10$ μm and doping $N_d=5\times10^{14}$ cm^{-3}. At 77 K, the highest experimental data are still about 5 times lower than the ultimate theoretical predictions. As the operating temperature of the photodiodes is lowered, the discrepancy between the theoretical curves and experimental data increases, which is due to additional currents in the junctions.

Many additional excess mechanisms affect the dark current of HgCdTe photodiodes.[8] They arise from nonfundamental sources located in the base and cap layer, the depletion region and the surface. As the operating temperature is lowered, the thermal dark current mechanisms become weaker and allow other mechanisms to prevail. In practice, nonfundamental sources dominate the dark current of the present HgCdTe photodiodes, with the exception of specific cases of near room temperature devices and the highest quality 77 K LWIR and 200 K MWIR devices. The main leakage mechanisms of HgCdTe photodiodes are: generation in the depletion region, interband tunneling, trap-assisted tunneling, and impact ionization. Some of them are caused by structural defects in the p-n junction. These mechanisms receive much attention now, particularly because they determine ultimately the array uniformity and yield and cost for some applications, especially those with lower operating temperatures.

In $Hg_{1-x}Cd_x$ Te photodiodes with $x\approx0.22$, the diffusion current in the zero-bias and low-bias regions is usually the dominant current down to 60 K.[39,40] At medium values of reverse bias, the dark current is mostly due to trap-assisted

                                                                  A. Rogalski   4367
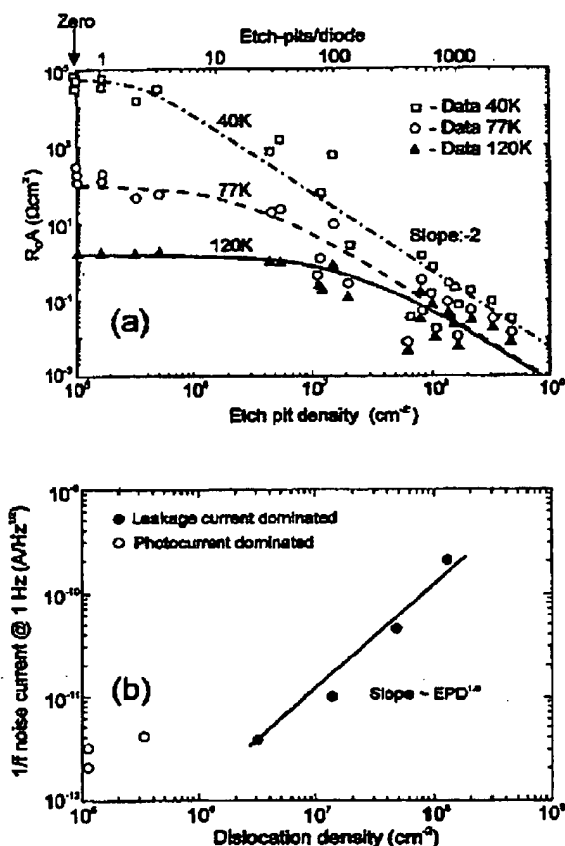

FIG. 15. Influence of the dislocation density on the parameters of HgCdTe photodiodes: (a) R_0A product versus EPD, showing the fit of model to data, for a 9.5-μm array (at 78 K), measured at 120, 77, and 40 K at zero FOV; (b) 1/f noise current at 1 Hz vs dislocation density measured at 78 K for a 10.3-μm HgCdTe photodiode array ($f/2$ FOV) (after Ref. 41).
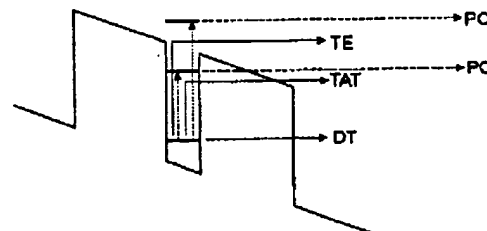

FIG. 16. The current mechanisms of QWIP: DT is the direct tunneling, TAT is the thermally assisted tunneling, and TE is the thermionic emission. The dashed lines show the photocurrent mechanism.

between 7×10^6 Ω and 1×10^9 Ω at 40 K contained no visible defects (Hg interstitials and vacancies). Dislocations, twins and subgrain boundaries in LWIR n^+-p HgCdTe photodiodes primarily produce bias dependent dark current, while Te precipitation and associated dislocation multiplication produces bias dependent noise.[43]

Dislocations are known to increase the dark current and the 1/f noise current. The reverse bias characteristics of HgCdTe diodes depend strongly on the density of dislocations intercepting the junction. Johnson et al.[41] showed that in the presence of high dislocations densities the R_0A product decreases as the square of the dislocation density; the onset of the square dependence occurs at progressively lower dislocation densities as the temperature decreases, which is shown in Fig. 15(a). At 77 K, R_0A begins to decrease at an etch-pit density (EPD) of approximately 10^6 cm^{-2}, while at 40 K R_0A is immediately affected by the presence of one or more dislocations in the diode. The scatter in the R_0A data at large EPD may be associated with the presence of an increased number of pairs of "interacting" dislocations in some of those diodes; these pairs are more effective in reducing the R_0A than individual dislocations.

In general, the 1/f noise appears to be associated with the presence of potential barriers at the contacts, interior, or surface of the semiconductor. Different models have been proposed to explain experimental data including the modulation of the surface generation current by the fluctuations of the surface potential and the influence of trap-assisted tunneling across a pinched-off depletion region.[8] Johnson et al.[41] presented the effect of dislocations on the 1/f noise. Figure 15(b) shows that, at low EPD, the noise current is dominated by the photocurrent, while at higher EPD the noise current varies linearly with EPD. It appears that dislocations are not the direct source of the 1/f noise, but rather increase this noise only through their effect on the leakage current. The 1/f noise current varies as $I^{0.76}$ (where I is the total diode current); similar to the fit of data taken on undamaged diodes.

The average value of the R_0A product at 77 K for a 10-μm cutoff HgCdTe photodiode at 77 K is around 300 Ω cm^2 and drops to 30 Ω cm^2 at 12 μm.[8,25,44–46] At 40 K, the R_0A product varies between 10^5 and 10^8 Ω cm^2 with 90% above 10^5 Ω cm^2 at 11.2 μm.

In comparison with HgCdTe photodiodes, the behavior of dark current of QWIP's is understood better. Figure 16 shows the current mechanisms in a QWIP. At low tempera-

tunneling. Trap-assisted tunneling dominates the dark current also at zero bias below 50 K. At high values of reverse bias, bulk band-to-band tunneling dominates. At low temperatures, such as 40 K, significant spreads in the R_0A product distributions are typically observed due to the onset of tunneling currents associated with localized defects. Moreover, HgCdTe photodiodes often have an additional surface-related component of the dark current,[8] particularly at low temperatures.

Chen et al.[42] carried out a detailed analysis of the wide distribution of the R_0 values of HgCdTe photodiodes operating at 40 K. Figure 14 shows the cumulative distribution function R_0 obtained in devices with a cutoff wavelength between 9.4 and 10.5 μm. It is clear that while some devices exhibit a fair operability with R_0 values spanning only two orders of magnitude, other devices show a poor operability with R_0 values spanning more than five to six orders of magnitude. Lower performance, with R_0 values below 7×10^6 Ω at 40 K, is usually due to gross metallurgical defects, such as dislocation clusters and loops, pin holes, striations, Te inclusions, and heavy terracing. However, diodes with R_0 values

A. Rogalski
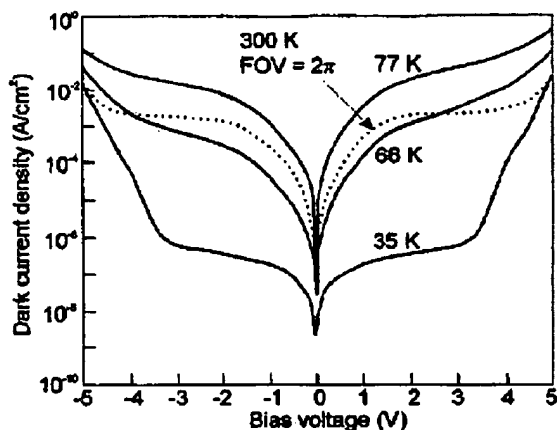

FIG. 17. Current-voltage characteristics of a QWIP detector having a peak response of 9.6 μm at various temperatures, along with the 300 K background window current measured at 30 K with an 180° FOV (after Ref. 48).

tures ($T<40$ K, $\lambda_c = 10$ μm), the dark current is mostly caused by defect-related direct tunneling. In the medium operating range between 40 and 70 K ($\lambda_c = 10$ μm), thermally assisted tunneling dominates. In this case, electrons are thermally excited and tunnel through the barriers with assistance from defects and the triangle part of the barrier at high bias. At temperatures higher than 70 K ($\lambda_c = 10$ μm), thermally excited electrons are thermionically emitted and transported above the barriers. It is difficult to block this dark current without sacrificing the photoelectrons (transport mechanisms of thermionically emitted current and photocurrent are similar). Minimizing thermionically emitted current is critical to the commercial success of the QWIP as it allows highly desirable high-temperature camera operation. Dropping the first
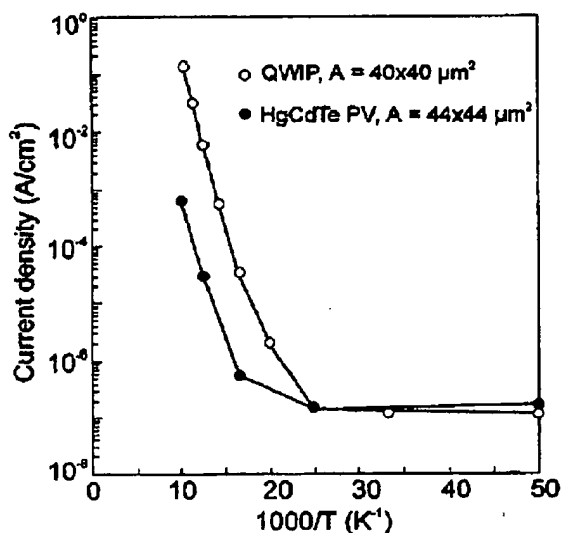

FIG. 18. Current density versus temperature for a HgCdTe photodiode and a GaAs/AlGaAs QWIP with $\lambda_c = 10$ μm (after Ref. 49).

excited state to the top theoretically causes the dark current to drop by a factor of ≈ 6 at 70 K. This compares well with the fourfold drop experimentally observed for 9-μm cutoff QWIP's.[47]

The value of the QWIP dark current could be adjusted using different device structures, doping densities, and bias conditions. Figure 17 shows the $I-V$ characteristics for temperatures ranging from 35 to 77 K, measured in a device at the 9.6-μm spectral peak. It shows typical operation at 2 V applied bias in the slowly varying region of current with bias between the initial rise in current at low voltage and the later rise at high bias. Typical LWIR QWIP dark current is about 10^{-4} A/cm^2 at 77 K. Thus, the same current in a 24×24 μm^2 pixel[47] will be in the nanoampere range. Comparing Figs. 12 and 17 we can see that a 9.6-μm QWIP must be cooled to 60 K to have a leakage current comparable to that of a 12-μm HgCdTe photodiode operating at the temperature higher by 25°.

Additional insight into the difference in the temperature dependence of the dark currents is given by Fig. 18. Figure 18 shows the current density versus inverse temperature for a GaAs/AlGaAs QWIP and a HgCdTe photodiode, both with $\lambda_c = 10$ μm. The current densities of both detectors at temperatures lower than 40 K are limited by tunneling (temperature independent). However, the current density of the QWIP is lower than that of the HgCdTe photodiode. The thermionic emission regime for the QWIP ($\geqslant 40$ K) is highly temperature dependent, and "cuts on" very rapidly. At 77 K, the QWIP has a dark current which is approximately two orders of magnitude higher than that of the HgCdTe photodiode.

A QWIP typically operates at a bias voltage from 1 to 3 V depending on the structure and the number of periods. For the voltage divided by the dark current density, the R_0A products are usually larger than 10^7 Ωcm^2 and 10^4 Ωcm^2 when operated at 40 K and 77 K, respectively.[32] These values indicate a very high impedance.

In low-background and low-temperature operating conditions, a QWIP operates very similarly to extrinsic bulk photoconductors. Electrons in the subbands of isolated quantum wells can be visualized as electrons attached to impurity states in bulk semiconductors. The photogenerated electrons depart from the doped, active QW region and leave behind a space-charge buildup. Thus, in order to operate a QWIP steadily, it requires a sufficient dark or background photocurrent to replenish the depleted QW's. This is not an issue for QWIP's operating at high background or high temperature conditions since refilling the space-charge buildup is easily provided. However, at a low operating temperature and a low background, the high resistivity of the barriers in the active region impedes electrons from entering the detector from the opposite electrode. As a result, a lower responsivity at high optical modulation is observed. To overcome this problem, a new detector structure, the blocked intersubband detector (BID) has been proposed.[50] In this structure, the active region of BID's consists of QW's separated by thin barriers, which creates subminibands due to the large overlap of sublevel wave functions. Thus, space-charge buildup will get quickly refilled by electrons via sequential resonant tunneling along the ground-state miniband from the emitter contact
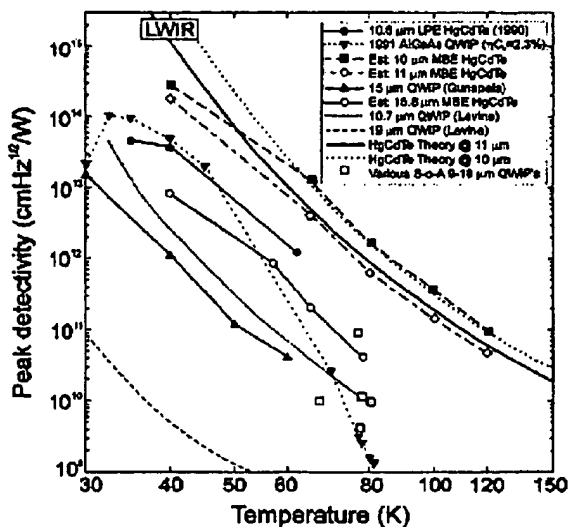
FIG. 19. LWIR detector detectivity versus temperature for GaAs/AlGaAs QWIP's and p–on–n HgCdTe photodiodes (after Refs. 2 and 51).

layer. To suppress the current of the device, a thick blocking barrier is placed between the active region and the collector.

D. Detectivity

We can distinguish two types of detector noise: radiation noise and intrinsic noise. Radiation noise includes signal fluctuation noise and background fluctuation noise. For infrared detectors, background fluctuation noise is higher compared to the signal fluctuation noise. In photodiodes, the shot noise is usually the major type of noise.

In the case of QWIP's, the major source of noise is the dark current, which is a generation-recombination one. Due to high levels of the dark current, the Johnson noise is neglected in most cases, especially at high temperatures of operation. At a lower temperature and at smaller pixel sizes, the Johnson noise becomes comparable to the dark noise. Owing to stable surface properties, very low $1/f$ noise is observed in QWIP's.

For FPA's pattern noise (which results from local variation of the dark current, photoresponse, and cutoff wavelength) is the major limitation of array performance, especially at low temperatures. This type of noise may be considered as a nonuniformity appearing across the array. This nonuniformity does not vary with time and reflects the intrinsic properties of an FPA. The fixed pattern noise is lower in QWIP arrays than in HgCdTe arrays due to a higher material quality and better-controlled cutoff wavelength.

Figure 19 compares the detectivities of p-on-n HgCdTe photodiodes with those of GaAs/AlGaAs QWIP's. The theoretical curves corresponding to HgCdTe photodiodes are calculated on the assumption of constant cutoff wavelengths of 10 μm and 11 μm. The VLWIR results for HgCdTe (14.8 μm at 80 K and 16.2 μm at 40 K) and QWIP at 16 μm show the intrinsic superiority of HgCdTe photodiodes. The detectivity of HgCdTe is roughly an order of magnitude higher,
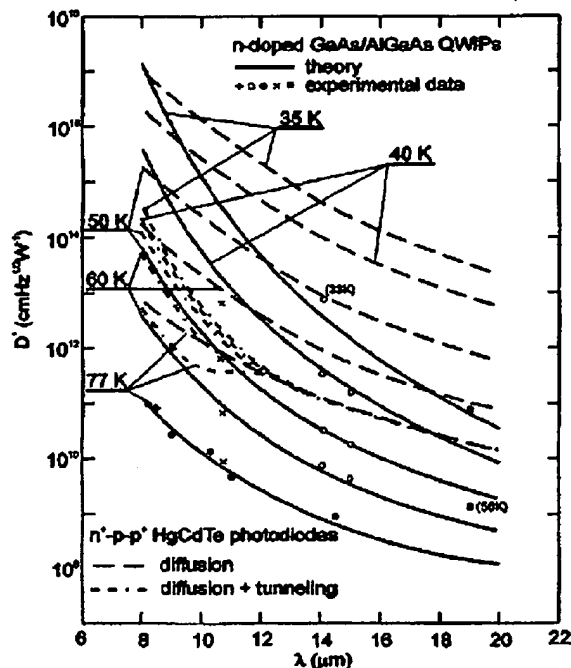

FIG. 20. Dependence of detectivity on the long wavelength cutoff for GaAs/AlGaAs QWIP's and n^+-p HgCdTe photodiodes at temperatures $\leqslant$77 K. The dashed lines are calculated for n-doped QWIP's. The theoretical lines for photodiodes are calculated assuming the Auger-limited diffusion current mechanism (dashed lines) and diffusion and tunneling mechanisms (dash-dotted lines) (after Refs. 2 and 51).

though the advantage decreases as the temperature is reduced. The best example of a region where QWIP's could have a performance advantage is low temperatures. As we can see from Fig. 19, at temperatures $\leqslant$45 K QWIP's offer superior performance at a 7.7 μm peak wavelength relative to HgCdTe at 10.6 μm.

Since 1987, rapid progress has been made in the detectivity of long-wavelength QWIP's, starting with bound-to-
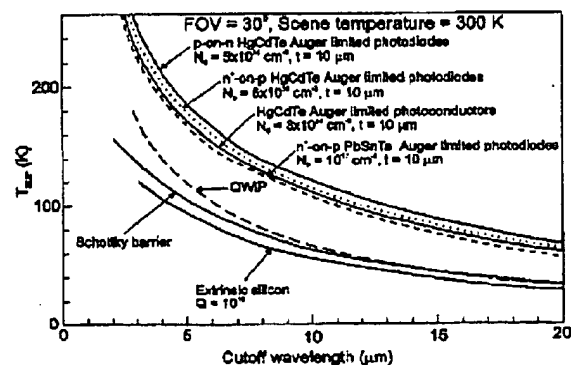

FIG. 21. Estimation of the temperature required for background limited operation of different types of photon detectors. In the calculations FOV =30° and T_B=300 K are assumed (after Ref. 31).
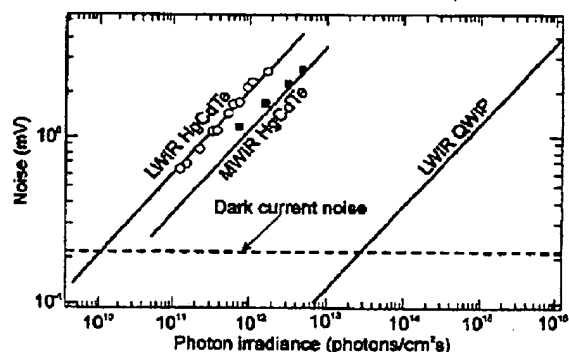
A. Rogalski

FIG. 22. Noise performance of typical HgCdTe photodiodes and QWIP (after Ref. 38).

bound QWIP's characterized by a relatively poor sensitivity and culminating in high performance bound-to-quasibound QWIP's with random reflectors. All the QWIP data are clustered between 10^{10} and 10^{11} cm $Hz^{1/2}$/W at operating temperatures of about 77 K. Gunapala and Bandara[3] assert that the highest possible D^* obtained using random gratings, for example, is about 2×10^{11} cm $Hz^{1/2}$/W. This appears to be consistent with the data including the enhanced QWIP formed by both patterning the multiple quantum wells and reducing the number of wells.

The above performance comparison of QWIP's with HgCdTe in the low temperature range is less favorable for photodiodes in the case of n^+-p structures. At low temperatures, the p-type HgCdTe material suffers from some nonfundamental limitations (contacts, surface, Schockley–Read

processes) more than the n-type one. Including the influence of tunneling, the comparison of detectivity is more advantageous for GaAs/AlGaAs QWIP's in the spectral region below 14 μm and at temperatures below 50 K (see Fig. 20).

E. Background-limited performance

The BLIP temperature is defined as the temperature at which the dark current equals the background photocurrent, at a given a FOV and background temperature. In Fig. 21, the calculated temperature required for background limited operation with a 30° FOV is shown as a function of the cutoff wavelength. We can see that the operating temperature of "bulk" intrinsic IR detectors (HgCdTe and PbSnTe) is higher than for other types of photon detectors. HgCdTe detectors with performance limited by background operate with thermoelectric coolers in the MWIR range. On the other hand, LWIR detectors ($8 \leq \lambda_c \leq 12$ μm) operate at ~100 K. HgCdTe photodiodes can operate at temperatures higher than extrinsic detectors, silicide Schottky barriers, and QWIP's can. However, the cooling requirements for QWIP's with cutoff wavelengths below 10 μm are less stringent than those for extrinsic detectors and Schottky barrier devices.

Figure 22 shows both photon and dark current noise voltage for an 8.5-μm cutoff QWIP and a 12-μm cutoff HgCdTe FPA. For the purposes of comparison, the measurements are normalized to the same dark current levels by adjusting the readout gain. Due to a lower quantum efficiency and higher dark current, QWIP detectors become BLIP only at photons fluxes in excess of 2×10^{13} photons/cm^2 s. By comparison, LWIR HgCdTe photodiodes are BLIP down to a photon flux of 1×10^{10} photons/cm^2 s. This indicates their
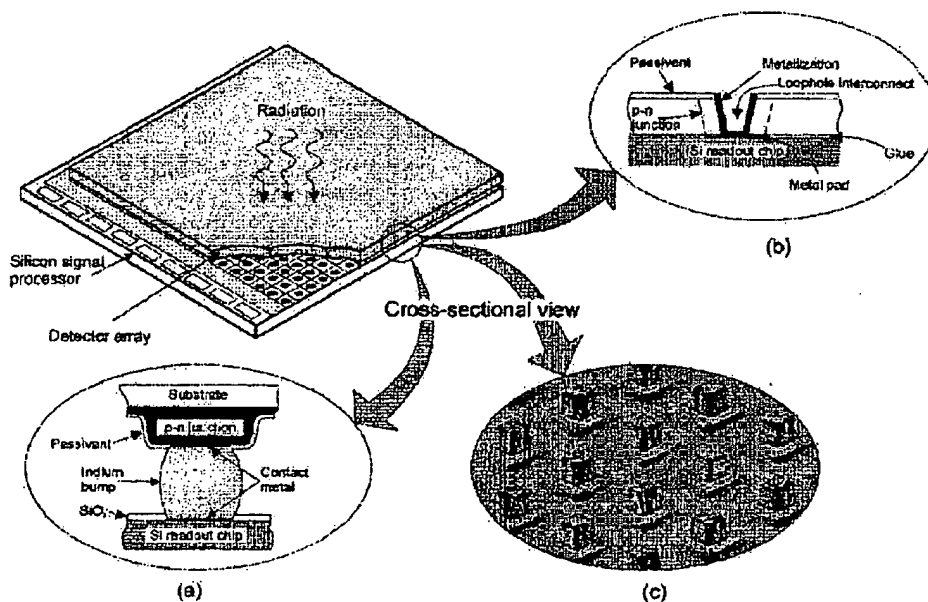

FIG. 23. Hybrid IR FPA interconnects technique between a detector array and silicon multiplexer: (a) indium bump technique, (b) loophole technique, and (c) scanning electronic microscopy photo of FPA.
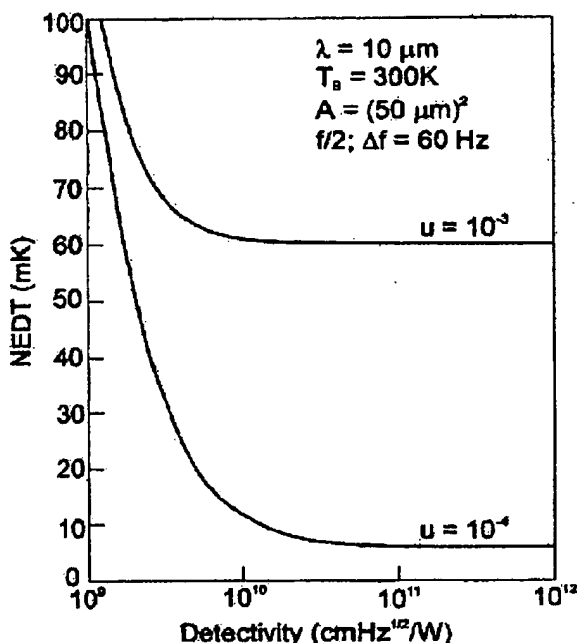
A. Rogalski   4371

FIG. 24. Noise equivalent difference temperature as a function of detectivity. The effects of nonuniformity are included for $u = 10^{-3}$ and 10^{-4} (after Ref. 2).

privileged position in the area of strategic and space applications, where longer-range detection at low backgrounds and sensitivity to longer wavelengths is required.

IV. FOCAL PLANE ARRAY PERFORMANCE

The combination of existing high-performance arrays and highly developed silicon integrated circuits in hybrid IR array/silicon planes have proved to be useful for thermal imaging systems with the thermal and spatial resolution unmatched by any competing technologies at present. In hybrid FPA's, detectors and multiplexers are fabricated on different substrates and mated with each other by flip-chip bonding (see Fig. 23). In this case the detector material and the multiplexer may be optimized independently. Other advantages of hybrid FPA's are the near 100% fill factor and the increased signal-processing area on the multiplexer chip. The detector array can be illuminated either from the frontside (with the photons passing through the transparent silicon multiplexer) or from the backside (with photons passing through the transparent detector array substrate). In general, the latter approach is most advantageous, as the multiplexer will typically have areas of metallization, as well another opaque regions that may reduce the effective optical area of the structure. In HgCdTe hybrid FPA's, photovoltaic detectors are formed in a thin HgCdTe epitaxial layer on transparent CdTe or ZnCdTe substrates. In HgCdTe flip-chip hybrid technology, the maximum chip size is on the order of 18 $\times 18$ mm^2.[52] In order to overcome this problem, the PACE (Producible Alternative to CdTe for Epitaxy) technology is being developed with sapphire or silicon as the substrate for

HgCdTe detectors. When using opaque materials, substrates must be thinned to 10–20 μm in order to obtain sufficient quantum efficiencies and to reduce the cross talk.

Progress in the area of LWIR HgCdTe photodiodes has been relatively slow. In October 1992, in the U.S.A, a consortium was formed (with DARPA's support) to develop p-on-n double-layer heterostructure HgCdTe photodiode FPA's and two color arrays.[53] MBE makes HgCdTe more favorable for producing high-quality FPA's.[54] Currently, 128×128, 256×256, and 320×256 LWIR arrays are commercially available, and such large formats as 640×480 on silicon substrate have been demonstrated.[55] Also prototype MWIR/LWIR two-color assemblies with 128×128 (Ref. 56) and 256×256 (Ref. 57) pixel formats have been produced to acquire IR imagery. It should be noted, however, that array size, uniformity, reproducibility, and yield are still difficult issues, especially for low-temperature and low-background operation.

The relatively new QWIP technology has been developed very quickly in the last decade. Large-size LWIR GaAs/AlGaAs FPA's with up to 640×480 (640×512) pixels have been demonstrated[3–5,58–64] with excellent uniformity and operability.

Among the cooled IR detector systems, only HgCdTe and QWIP offer wavelength flexibility and multicolor capabilities. Tables V and VI summarize the present status of the performance of both detector systems.

A. Uniformity

As was discussed by Levine,[2] at detectivities approaching values above 10^{10} cm Hz$^{1/2}$/W (see Fig. 24), FPA performance is uniformity limited and thus essentially independent of detectivity. An improvement in nonuniformity from 0.1% to 0.01% after correction could lower the NEDT (see Appendix 1) from 63 to 6.3 mK.

The nonuniformity value is usually calculated using the standard deviation over the mean, counting the number of operable pixels in an array. For a system operating in the LWIR band, the scene contrast is about 2%/K of the change in the scene temperature. Thus, to obtain a pixel to pixel variation in the apparent temperature less than, e.g., 20 mK, the nonuniformity in response must be less than 0.04%. This is nearly impossible to achieve in the case of an uncorrected response of the FPA; therefore, a two-point correction is typically used.

FPA uniformity influences the complexity of an IR system. Uniformity is important for accurate temperature measurements, background subtraction, and threshold testing. Nonuniformities require the development of compensation algorithms to correct the image; but, by consuming a number of analog-to-digital bits they also reduce the dynamic range of the system.

Tactical IR FPA's usually require operation in the LWIR window with a small number of applications in the 3–5 μm window. The distance between the sensor and the target is typically short, allowing the use of imaging sensors with large FPA's where precise radiometry is not critical. Imaging arrays can usually tolerate some percentage of dead or degraded pixels without the jeopardizing mission performance.

TABLE V. Performance specifications for LWIR HgCdTe FPA's (after SOFRADIR and SBRC data sheets).

Parameter	SOFRADIR		SBRC
Format	128×128	320×256	256×256
Cut on–cut off (μm)	7.7–10.3	7.7–9.0	8.5–11.0
FPA temperature (K)	< 85	< 90	77 (up to 100)
Detector pitch (μm)	50	30	30
Fill factor (%)	>70		
Charge handling capacity	>118×10^6 e^-	12 or 36	8×10^6 e^- (min)
Frame rate (Hz)	to 300	to 400	to 120
D^* peak rms/T_{int}/pitch (average) ($cm\,Hz^{1/2}\,W^{-1}$)	1.1×10^{11}		
Pixel NETD (average)	10 mK for 275 Hz	18	
NEI (photons/cm^2 s) (max)			1.52×10^{12}
Typical FOV	$f/2$	$f/2$	
Fixed pattern noise	7% RMS		
Crosstalk (optical and electrical) (%)	2		
Array operability (%)	99		99

Tactical backgrounds in the IR windows are relatively high with about 10^{16} photons/cm^2 s reaching the detector.

The admissible nonuniformity depends on the requirements of the operability. A higher requirement on the operability usually leads to a lower uniformity and vice versa. A typical uncorrected-response nonuniformity in QWIP FPA's is 1%–3% with the operability (the fraction of good pixels) higher than 99.9%. For a 128×128 15-μm array fabricated by Jet Propulsion Laboratory (see Table VI), the uncorrected standard deviation is 2.4% and the corrected nonuniformity is 0.05%. For a large 640×486 9-μm FPA the uncorrected noise nonuniformity is about 6%, and after a two-point correction improves to an impressive 0.04%.[60] For an FPA of the the same format demonstrated by Lockheed Martin, operability higher than 99.98% was described.[58] It is very hard for HgCdTe to compete with QWIP's in the area of high uniformity and operability of large-array formats, especially at low temperatures and in the VLWIR region.

High uniformity and high operability, as shown in the above examples, demonstrate the maturity of GaAs growth and processing technology. In this context, the nonuniformity and operability have been an issue for HgCdTe, although the values published recently for Sofradir and SBRC arrays are as high as 99%. As we compare the performance of both types of FPA's (see Table V and VI), the array operability is higher for QWIP's (above 99.9%).

Nonuniformity is a serious problem in the case of VLWIR HgCdTe detectors. The variation of x across a $Hg_{1-x}Cd_x Te$ wafer causes a much larger spectral nonuniformity (e.g., at 77 K the variation of $\Delta x = 0.2\%$ gives $\Delta\lambda_c = 0.064$ μm at $\lambda_c = 5$ μm, but $\Delta\lambda_c = 0.51$ μm at 14 μm), which cannot be fully corrected by two or three point corrections.[32] Therefore the required composition control is much more stringent for VLWIR than for MWIR.

In the case of QWIP's, extending the cutoff wavelengths to VLWIR is relatively easy since there is little change in the material properties, growth, and processing. However, a serious requirement for maintaining the device performance is to lower the operating temperature. Due to lower quantum well barriers, the dark current of thermionic emission dominates at lower temperatures. In order to achieve performance equivalent to that of a 10-μm cutoff QWIP at 77 K, the temperature needs to be lowered to 55 K for a 15-μm cutoff and to 35 K for a 19-μm cutoff (see Table VI and Fig. 19).

B. NEDT

The noise in HgCdTe photodiodes at 77 K is due to two sources: the shot noise from the photocurrent and the Johnson noise from the detector resistance. It can be expressed as[35]

TABLE VI. Properties of JPL 9-μm and 15-μm GaAs/AlGaAs QWIP FPA's (after Refs. 5 and 59–61).

Parameter	$\lambda_c = 9$ μm			$\lambda_c = 15$ μm
Array size	256×256 (Ref. 61)	320×256 (Ref. 5)	640×486 (Ref. 60)	128×128 (Ref. 59)
Pixel pitch (μm)	38×38	30×30	25×25	50×50
Pixel size (μm)	28×28	28×28	18×18	38×38
Optical coupling	2D periodic grating	2D periodic grating	2D periodic grating	2D periodic grating
Peak wavelength (μm)	8.5	8.5	8.3	14.2
Cutoff wavelength, 50% (μm)	8.9	8.9	8.8	14.9
Operability (%)	99.98	99.98	99.9	>99.9
Uncorrected nonuniformity (%)	5.4		5.6	2.4
Corrected uniformity, 17–27 °C (%)	0.03		0.04	0.05
Quantum efficiency (%)	6.4	6.9	2.3	3
D^* ($cm\,Hz^{1/2}\,W^{-1}$)	2.0×10^{11} (70 K)		2.0×10^{11} (70 K)	1.6×10^{10} (55 K)
NEDT with $f/2$ optics (mK)	23 (70 K)	33 (70 K)	36 (70 K)	30 (45 K)

A. Rogalski   4373

$$I_a = \sqrt{\left(2qI_{ph} + \frac{4kT_d}{R}\right)\Delta f},\qquad (23)$$

where k is the Boltzmann constant and R is the dynamic resistance of a photodiode. Assuming that the integration time τ_{int} is such that the readout node capacity is kept half full, we have

$$\Delta f = \frac{1}{2\tau_{int}}\qquad (24)$$

and then

$$I_n = \sqrt{\left(2qI_{ph} + \frac{4kT_d}{R}\right)\frac{1}{2\tau_{int}}}.\qquad (25)$$

At tactical background levels, the Johnson noise is much smaller than the shot noise from the photocurrent. In the case where the number of electrons collected in a frame is limited by the capacity of the ROIC charge well, which is often true, the signal to noise ratio is given by[35]

$$\frac{S}{N} = \frac{qN_w/2\tau_{int}}{\sqrt{2q\left(\frac{qN_w}{2\tau}\right)\frac{1}{2\tau_{int}}}} = \sqrt{\frac{N_w}{2}}.\qquad (26)$$

Assuming that the temperature derivative of the background flux Φ can be written to a good approximation as

$$\frac{\partial \Phi}{\partial T} = \frac{hc}{\bar{\lambda}kT_B^2}Q\qquad (27)$$

and using Eq. (26), the NEDT is equal to

$$NEDT = \frac{2kT_B^2\bar{\lambda}}{hc\sqrt{2N_w}}.\qquad (28)$$

In the last two equations, $\bar{\lambda} = (\lambda_1 + \lambda_2)/2$ is the average wavelength of the spectral band between λ_1 and λ_2.

If one assumes a typical storage capacity of 2×10^7 electrons, $\bar{\lambda} = 10~\mu m$, and $T_B = 300$ K, Eq. (28) yields NEDT of 19.8 mK.

The same estimate can be made for QWIP. In this case the Johnson noise is negligible compared to the generation-recombination noise therefore,

$$I_n = \sqrt{4qg(I_{ph} + I_d)\frac{1}{2\tau_{int}}},\qquad (29)$$

where the dark current may be approximated by

$$I_d = I_0 \exp\left(-\frac{E_a}{kT}\right).\qquad (30)$$

In the above expressions, I_d is the dark current, I_0 is a constant that depends on the transport properties and the doping level, and E_a is the thermal activation energy, which is usually slightly less than the energy corresponding to the cutoff wavelength of the spectral response. It should be also stressed that g, I_{ph}, and I_0 are bias dependent.

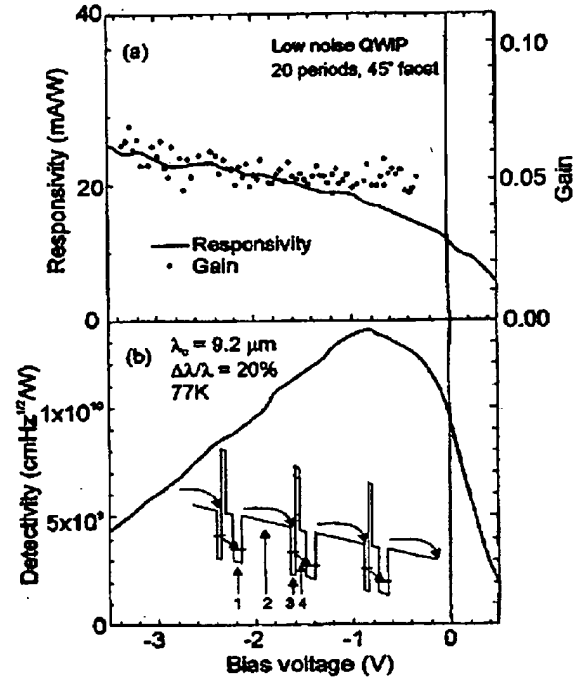The signal-to-noise ratio for a storage-capacity-limited QWIP is given by

FIG. 25. Peak responsivity, gain (a), and peak detectivity (b) of a low-noise QWIP versus bias voltage (after Ref. 62).

$$\frac{S}{N} = \frac{qN_w/2\tau_{int}}{\sqrt{4qg\left(\frac{qN_w}{2\tau}\right)\frac{1}{2\tau_{int}}}} = \frac{1}{2}\sqrt{\frac{N_w}{g}},\qquad (31)$$

and the NEDT is

$$NEDT = \frac{2kT_B^2\bar{\lambda}}{hc}\sqrt{\frac{g}{N_w}}.\qquad (32)$$

Comparing Eqs. (28) and (32) one may notice that the value of NEDT in a charge-limited QWIP detectors is better than that of HgCdTe photodiodes by a factor of $(2g)^{1/2}$ since a reasonable value of g is 0.4. Assuming the same operation conditions as for HgCdTe photodiodes, the value of NEDT is 17.7 mK. Thus, a low photoconductive gain actually increases the S/N ratio and a QWIP FPA can have a better NEDT than an HgCdTe FPA with a similar storage capacity.

The above deduction was confirmed experimentally by a research group at Fraunhofer IAF.[62–64] The photoconduction mechanism of a photovoltaic "low-noise" QWIP structure is indicated in the inset of Fig. 25(b), where four zones (1)–(4) of each period are shown. Because of the period layout, the detector structure has been called a four-zone QWIP.[65] The first two zones (1 and 2) are analogous to the barrier and well of a conventional QWIP [see Fig. 6(a)]. Two additional zones are present in order to control the relaxation of the photoexcited carriers: namely, a capture zone (3) and a tunneling zone (4). The tunneling zone has two functions; it blocks the carriers in the quasicontinuum (carriers can be

A. Rogalski
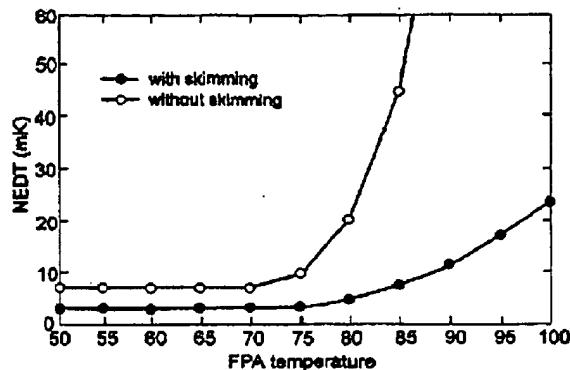
FIG. 26. NEDT improvement due to the skimming architecture ($f/1$, 25 μm pitch, $T_b = 300$ K).

FIG. 28. NEDT of a 320×256 QWIP FPA ($\lambda_c = 8.9$ μm, $f/2$ optics, 50% well fill, pitch 30 μm) as a function of operating temperature (after Ref. 5).

captured efficiently into a capture zone) and transmits the carriers from the ground state of the capture zone into the excitation zone of the subsequent period. In this way, the noise associated with the carrier capture is suppressed.

Figure 25 summarizes the performance of a typical 20-period low-noise QWIP with a cutoff wavelength of 9.2 μm. The peak responsivity is 11 mV at zero bias (photovoltaic operation) and about 22 mA in the range between −2 and −3 V. Between −1 and −2 V, a gain of about 0.05 is observed. The detectivity has its maximum around −0.8 V and about 70% of this value is obtained at zero bias. Due to the asymmetric nature of the transport process, the detectivity strongly depends on the sign of the bias voltage. This behavior is in strong contrast with a conventional QWIP where the detectivity vanishes at zero bias.

Based on the photovoltaic low-noise four-zone QWIP structure, the Fraunhofer group[62–64] has manufactured a 256×256 FPA camera operating at 77 K with the 9-μm cutoff wavelength. The camera exhibits record-low NEDT values of 7.4 mK with 20-ms integration time and 5.2 mK with

40 ms. It is the best temperature resolution ever obtained in the LWIR regime.

Considerations carried out in the Appendix 1 indicate that for a given frame time and maximum storable charge, the way to increase the performance of LW staring systems is to reduce the dark current in order to get photon limited system performance. Bois et al.[66] described their unique approach of using two stacks of identical QWIP's and a new skimmed architecture accommodating the large dark current of the detector. The QWIP at the top stack produced a higher photocurrent than that of the lower stack. Therefore, using a bridge readout arrangement, the dark current of the QWIP at the top stack may be subtracted by the bottom stack without sacrificing much of the photocurrent. With this detector structure, the FPA should be able to operate at much higher temperatures and with a longer integration time. After the selection of the optimum subtraction rates the expected NEDT is 10 mK at 85 K for $\lambda_c = 9.3$ μm and $f/1$ optics. This performance is usually achieved with standard QWIP's at 65 K (see Fig. 26)
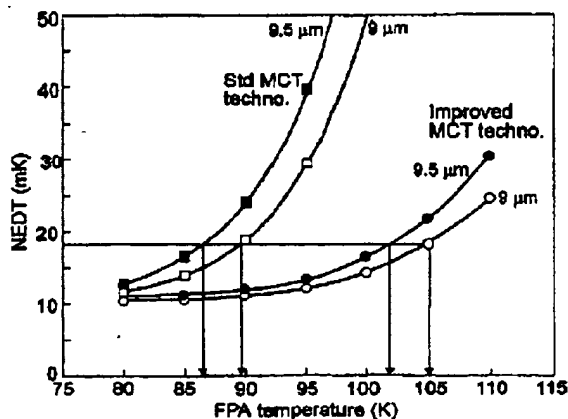

FIG. 27. NEDT of a 128×128 HgCdTe FPA ($f/2$ optics, 50% well fill, pitch 50 μm) as a function of operating temperatures (after Ref. 67).
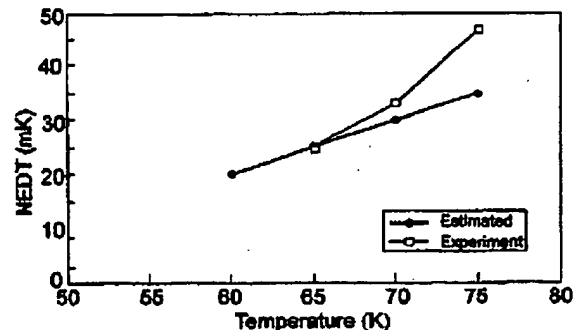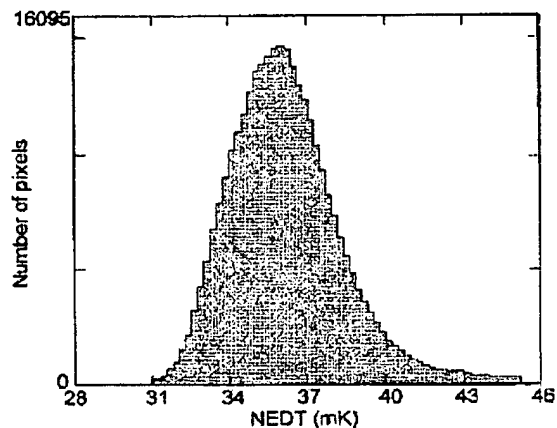

FIG. 29. NEDT histogram of a 640×486 QWIP FPA ($\lambda_c = 8.8$ μm) at operating temperature of 70 K, bias voltage of −2 V at 300 K background with $f/2$ optics (after Ref. 61).

Two other solutions can be envisaged for the reduction of the dark current: (i) to decrease the focal plane operating temperature, and (ii) to decrease the cutoff wavelength by adjusting the detector material composition. The second solution allows one to increase the focal plane operation temperature without degrading the performance.

Figure 27 compares the performance of two Sofradir HgCdTe staring arrays. One of these arrays is sensitive between 7.7 μm and 9 μm, the other between 7.7 μm and 9.5 μm. Higher performance with improved technology has been obtained using, on the one hand, the reduced-dark-current detector technology and, on the other hand, a new readout circuit architecture maximizing both the charge handling capacity and the responsivity.[68] At a constant temperature, the performance is higher for $\lambda_c = 9$ μm due to the fact that the dark current is lower and the integration time can be increased. As a consequence, the focal plane operation temperature of the improved arrays with $\lambda_c = 9$ μm can be increased up to 105 K and up to 102 K for arrays with $\lambda_c = 9.5$ μm (NEDT<18 mK in this example).

Figure 28 shows the measured and estimated NEDT as a function of the temperature for a 8.9-μm QWIP FPA. In comparison with a representative HgCdTe FPA (Fig. 27), this parameter exhibits a strong temperature dependence. At temperatures <70 K, the signal-to-noise (SNR) ratio of the system is limited by the multiplexer readout noise and the shot noise of the photocurrent. At temperatures >70 K, the temporal noise due to the QWIP's higher dark current becomes the limitation. As mentioned earlier, this higher dark current is due to thermionic emission and thus causes the charge storage capacitors of the readout circuitry to saturate.

Figure 29 presents a NEDT histogram of a 640×486 QWIP FPA ($\lambda_c = 8.8$ μm) at an operation temperature of 70 K, bias voltage of −2 V, background temperature of 300 K with $f/2$ optics. The mean value of the NEDT histogram is 36 mK. The uncorrected nonuniformity (standard deviation/mean) of this unoptimized FPA is only 5.6% including the 1% nonuniformity of the readout circuit and the 1.4% nonuniformity due to the fact that the cold stop is unable to give the same field of view to all the pixels in the FPA.

Comparing the values of NEDT for both types of FPA's (see also Tables V and VI), we can see that the performance of LWIR HgCdTe arrays is generally better. However, up to now the best temperature resolution in the LWIR band has been obtained with four zone QWIP structures.[62–64]

C. Charge handling capacity and integration time

One of the simplest and most popular readout circuits for IR FPA's is the direct injection (DI) input, where the dark current and photocurrent are integrated into a storage capacity. In this case, the bias varies across the array by about ±(5−10) mV due to the variations in the transistor thresholds. At 80 K, HgCdTe diodes show very small changes of the leakage current with small changes in reverse bias near zero volts (see Fig. 12). The goal is to fit a capacitor as large as possible into the unit cell, particularly for high tactical applications, where signal-to-noise ratios can be obtained through longer integration times. For high injection efficien-
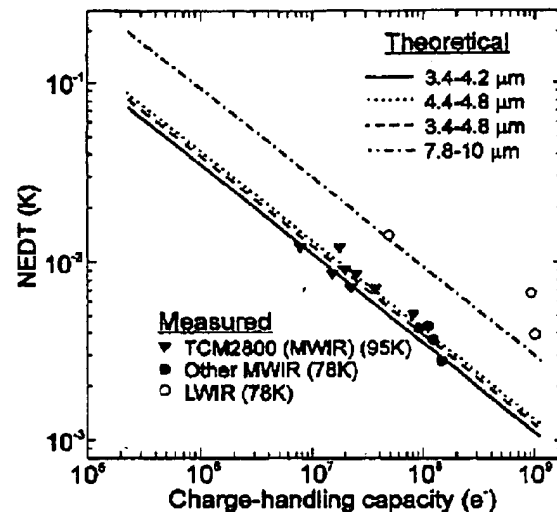

FIG. 30. NEDT versus charge handling capacity (after Ref. 72).

cies, the resistance of the field effect transistor (FET) should be small compared to the diode resistance at its operating point. Generally, it is not difficult to fulfill this inequality for MWIR HgCdTe staring designs where diode resistance is large ($R_0 A$ product in the range of more than 10^6 Ω cm^2), but it may be very important for LWIR designs where R_0 is small ($R_0 A$ product about 10^2 Ω cm^2). LWIR HgCdTe photodiodes operate with a small reverse bias near zero volts. In this case, a large bias is desirable but its value depends strongly on the material quality of the array. For very high-quality LWIR HgCdTe arrays a bias of −1 V is possible.

The bias applied to a QWIP array is usually higher than that applied to a HgCdTe array and is around 2–3 V. However, the readout power consumption is similar for QWIP and HgCdTe and is negligible compared with that of the readout electronics. The power dissipation in an imaging 640×480 QWIP FPA is, for example, lower than 150 mW.[58] It results from the very high impedance of the QWIP. This impedance is in the GΩ range at 77 K for a pixel size of 24×24 μm^2.[32] It makes the readout design very easy in terms of achieving high efficiency. The injection efficiency of a 9-μm cutoff 640×486 QWIP array is, for example, 99.5%.[58] However, Singh and co-workers[69,70] uncovered a possible problem connected with the offsets (up to ≈1 V) in the low-temperature current-voltage characteristics (nonzero current at zero bias). This observation indicates the presence of a time-constant effect due to the charging of a capacitance in the QWIP detector. QWIP's behave like RC circuits, with a resistance in series with a capacitance. The presence of large offsets or large dynamic resistance could cause difficulties in matching the impedances of the FPA and ROIC, especially at low biases and certainly at low temperatures.

The DI input circuit is not generally used for low backgrounds due to injection efficiency issues. The strategic applications often have low backgrounds and require low noise multiplexers interfaced to high-resistance detectors. The in-

A. Rogalski
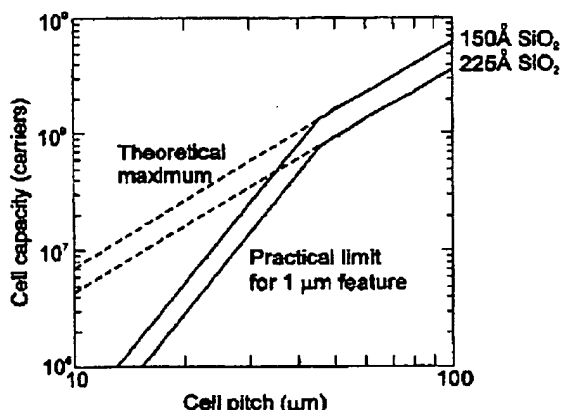
FIG. 31. Charge handling capacity versus cell pitch (after Ref. 73).

FIG. 32. Trends for design rule minimum dimensions and maximum bias voltage of silicon foundry requirements (after Ref. 52).

put circuit commonly used for strategic applications is the capacitative transimpedance amplification (CTIA) input circuit.[71] Increased injection efficiency is also possible with buffered DI. The latter two input circuits also accentuate the $1/f$ noise and the operability but they require higher power to operate.

At high backgrounds, it is often impossible to handle the large number of carriers generated over frame times that are compatible with the standard video frame rates. The user is forced to integrate for only a fraction of the full frame time. Off-FPA integration of subframes is then used to attain a level of sensor sensitivity commensurate with the detector-limited FPA detectivity and not the charge-handling-limited sensor detectivity.

Figure 30 shows the theoretical NEDT versus charge handling capacity for HgCdTe FPA's assuming that the integration capacitor is filled to half the maximum capacity (to preserve dynamic range) under nominal operating conditions in different spectral bandpasses: 3.4–4.2 μm, 4.4–4.8 μm, 3.4–4.8 μm, and 7.8–10 μm. The measured data for TCM2800 at 95 K, other PACE HgCdTe FPA's at 78 K and representative LWIR FPA's are also shown. We can see that the measured sensitivities agree with the expected values.

The well charge capacity is the maximum amount of the charge that can be stored in the storage capacitor of each cell. The size of the unit cell is limited to the dimensions of the detector element in the array. In the case of a large LWIR HgCdTe hybrid array, a mismatch between the thermal expansion coefficients of the detector array and the readout can force the cell pitch to 20 μm or less to minimize lateral displacement. However, the development of heteroepitaxial growth techniques for HgCdTe on Si has opened the possibility of a cost-effective production of significant quantities of large-area arrays through the utilization of large-diameter Si substrates.

Figure 31 shows the charge handling capacity versus cell pitch. We can see that for a 30×30 μm^2 pixel size, the storage capacities are limited to the range of 1 to 5×10^7 electrons depending on the design feature. At a 0.8-μm feature if the oxide is thinned to 150 Å to recoup capacity, the readout
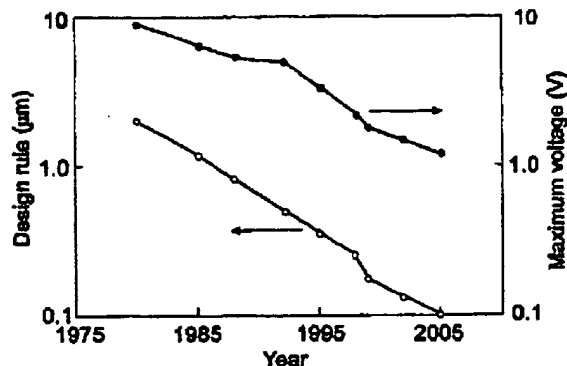
yield and device reliability may be reduced due to oxide damage from hot carriers.[73] For example, a storage capacity of 5×10^7 electrons requires that the total current density of a detector with a 30×30 μm^2 pixel size be lower than 27 μA/cm^2 with a 33-ms integration time.[32] If the total current density is in the 1 mA/cm^2 range, the integration time has to be reduced to 1 ms. In LWIR HgCdTe FPA's the integration time is usually below 100 μs. Since the noise power bandwidth $\Delta f = 1/2t_{int}$, a short integration time causes extra noise during integration.

LWIR QWIP FPA's using conventional ROIC's typically operate at 60–65 K. Due to the smaller quantum efficiency of a QWIP, filling the charge capacitor is not a problem in high-background applications. QWIP's allow a longer integration time, which yields relatively low values of NEDT. At higher temperatures, however, the dark current of QWIP's is high and fills the charge capacitor very quickly. The current subtraction and switched capacitor noise filtering capabilities of ROIC's permit a low NEDT at higher operating temperatures. In this case, however, the readout circuit is complicated, which limits the array size.

The goal of third-generation imagers is to achieve sensitivity improvement corresponding to a NEDT of about 1 mK. The analysis of Eq. (A2) (see Appendix A1) indicates that the required charge storage capacity in a 300 K scene in the LWIR region with the thermal contrast of 0.04, is above 10^9 electrons. This high charge-storage density within the small pixel dimensions probably cannot be obtained with standard CMOS capacitors.[52] Although the reduced oxide thickness of the submicrometer design rules gives a large capacitance per unit area, the reduced bias voltage, as illustrated in Fig. 32, largely cancels any improvement in the charge storage density. Ferroelectric capacitors may provide much higher charge storage densities than the oxide-on-silicon capacitors now used, however, such technology is not yet incorporated into standard CMOS foundries. Norton et al.[52] suggested using stacked hybrid structures as an interim solution at least to incorporate the desired charge storage density in the detector–readout–capacitor structures.

D. Cost

The cost of a FPA depends strongly on the maturity of the technology and varies with the production quantity in different companies. So far, large-size LWIR FPA's have been developed in R&D laboratories only, without mass production experience. According to Sofradir, a continuous effort in the industry has decreased the cost of HgCdTe detectors by a factor of 5 to 10.[74] The cost of making high-performance cooled components can be broken down into three parts of about equal weight: the chip (detector and ROIC), the Dewar, and the integration and tests.[75] In addition, the user must add the cryogenic machine cost. This cost is not negligible compared to the other ones. Even if the detection circuit is free of charge, the total cost would only be reduced by about 15%–20%. This explains why the cost of PtSi and QWIP detectors is not markedly less than that of photon detectors of the same complexity, even though the raw materials (Si or GaAs) are much cheaper than in the case of HgCdTe. Moreover, since a PtSi requires a very wide optical aperture to obtain acceptable performance and since a QWIP requires lower operating temperatures than other photon detectors, a possible reduction in the purchase price is counterbalanced by a significant increase in operating cost.

HgCdTe detectors have been the center of a major industry during the last three decades. The technology is relatively mature in the MWIR region with a size up to 1024×1024,[25] but it is not extended easily to LWIR. To make components with more pixels, a reduction of the pitch is required or the mastering of the thinning operation needed to withstand thermal cycling (differential thermal expansion between CdZnTe and silicon). It seems that, in the future, Si substrates will be used, because they offer many well-known advantages as compared to bulk CdZnTe substrates (a much larger size available at lower cost, a thermal expansion coefficient matching that of Si readout chips, higher purity, and compatibility with automated wafer processing/handling methodology due to their superior mechanical strength and flatness). Promising results have been achieved in the SWIR and MWIR spectral region. During the last four years the defect density for MWIR layers of HgCdTe grown by MBE on silicon substrates decreased from 2000 cm^{-2} to below 500 cm^{-2}.[52] Currently, MWIR arrays with pixel operability of 98% can be produced from this material. For comparison, the operability of CdZnTe is typically about 99% or higher. Defect densities in the LWIR material grown on silicon substrates continue to limit performance but they have been reduced by an order of magnitude in the past decade.[52,55]

In comparison with HgCdTe FPA's, the industry has much less experience in QWIP FPA's; therefore, improvements can be expected, especially since this technology is at an earlier stage of development. The major challenge is to improve the device performance by means of tuning the device and grating designs. Because of the maturity of GaAs growth technology and the stability of the material system, no investment is needed for developing QWIP substrates, MBE growth, and processing technology.[32] Four-inch QWIP wafers are commercially available.[76] Development of LWIR and multicolor HgCdTe detectors is extremely difficult, es-

pecially for low-background applications. It means that the cost of the development QWIP technology and QWIP production will be less than in the case of HgCdTe.

E. Reliability

In our discussion the reliability issue has been omitted due to the fact that statistical data on this subject are not available. In several applications, especially military systems, there is a considerable demand for high reliability to ensure both the success of the mission and minimal risk to the user. Two reliability challenges affect both FPA's: survival in high-temperature system-storage environments and withstanding repetitive thermal cycles between ambient and cryogenic temperatures. In HgCdTe, as well as in QWIP FPA's, indium bumps are used to hybridize both types of detectors with a silicon multiplexer. However, certain problems can be expected in the case of QWIP arrays, because indium bumps are known to form many different alloys with III–V compounds.

Very large FPA's may exceed the limits of hybrid reliability engineered into contemporary cooled structures. Hybrids currently use mechanical constraints to force the contraction of the two components to closely match each other. This approach may have limits when the stress reaches a point where the chip fractures. Three approaches offer an opportunity to resolve this issue:

(i) Elimination of the thick substrate that limits the detector active region from deforming at the slower rate of the silicon readout.

(ii) Subdivision of the array into a number of regions.

(iii) Use of silicon as the substrate for the growth of the detector material.

The process sequence for making HgCdTe photodiodes and QWIP's on silicon substrates would ultimately be simplified because of the maturity level of the existing silicon technology. However, the major difficulties inherent in this approach are the following:[52]

(i) Less area would be available for readout circuitry.

(ii) Microlens arrays would be required to regain the fill factor.

(iii) Material quality may not be adequate for low-leakage detectors, particularly in the case of LWIR HgCdTe photodiodes.

(iv) Silicon integrated circuits are processed on $\langle 100 \rangle$ oriented silicon, but the preferred orientation for HgCdTe growth on silicon is near the $\langle 211 \rangle$ orientation.

A less demanding approach to the elimination of the thick detector substrate is to use the loophole or high-density vertically-integrated photodetector device structures already practiced by GEC Marconi and DRS, respectively. In this approach, HgCdTe material is glued to the readout and contacts are made through a thin layer (10–20 μm) after the substrate is removed [see Fig. 23(b)]. Another approach is to remove the substrate after hybridization with indium bumps. Substrate removal is a standard practice with very large hybrid InSb arrays (1024×1024 pixels). This approach has been recently adopted for QWIP arrays.[4,5,77] After epoxy backfilling of the gaps between the array and the readout
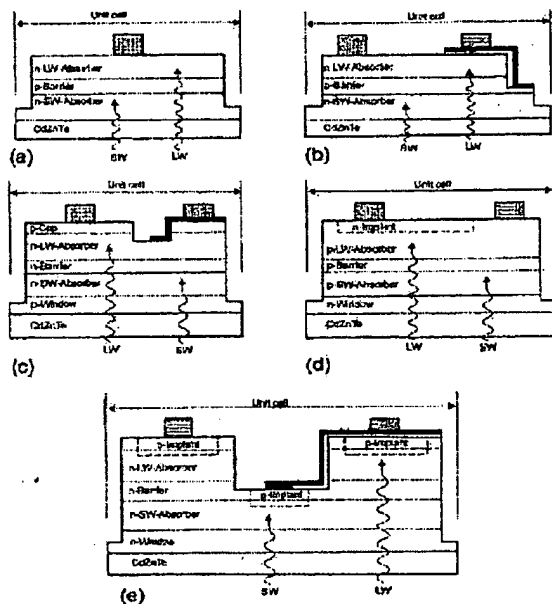
FIG. 33. Cross section views of unit cells for various back-illuminated dual-band HgCdTe detector approaches: (a) bias-selectable $n-p-n$ structure reported by Raytheon (Ref. 78), (b) simultaneous $n-p-n$ design reported by Raytheon (Ref. 80), (c) simultaneous $p-n-n-p$ reported by BAE Systems (Ref. 83), (d) simultaneous $n-p-p-p-n$ design reported by Leti (Ref. 85), and (e) simultaneous structure based on $p-on-n$ junctions reported by Rockwell (Ref. 56) (after Ref. 91).

multiplexer, the substrate is thinned to form a very thin membrane (≈ 1000 Å). This allows not only the elimination of the thermal mismatch between the silicon readout and the GaAs-based detector array but also the complete elimination of the pixel-to-pixel cross talk, and finally, significant enhancement of the optical coupling of IR radiation to QWIP pixels.

V. MULTIBAND FPA's

Multicolor capabilities are highly desirable for advance IR systems. Systems that gather data in separate IR spectral bands can determinate both the absolute temperature and the unique signatures of the objects in the scene. By providing this new dimension of contrast, multiband detection also enables advanced color processing algorithms to further improve the sensitivity above that of single-color devices. Multispectral detection permits rapid and efficient understanding of the scene in a variety of ways. In particular, two-color IR FPA's can be especially beneficial for threat-warning applications. By using two IR wave bands, spurious information, such as background clutter and sun glint, may be subtracted from the IR image, leaving only the objects of interest. Multispectral IR FPA's can also play many important roles in ground and planetary remote sensing, astronomy, etc. Thus, the effective signal-to-noise ratio of two-color IR FPA's greatly exceeds that of single-color IR FPA's for specific applications.

Currently, multispectral systems rely on cumbersome imaging techniques that either disperse the optical signal across multiple IR FPA's or use a filter wheel to spectrally select the image focused on a single FPA. These systems contain beam-splitters, lenses, and bandpass filters in the optical path to focus the images onto separate FPA's corresponding to different IR bands. Also complex alignment is required to map the multispectral image pixel for pixel. Consequently, these approaches are expensive in terms of size, complexity, and cooling requirements.

At present, the efforts are being made to fabricate a single FPA with multicolor capability to eliminate the spatial alignment and temporal registration problems that exist whenever separate arrays are used, to simplify optical design, and reduce size, weight, and power consumption.

Considerable progress has been recently demonstrated by research groups at Hughes Research Laboratory (Raytheon),[78-80] Lockheed Martin (BAE Systems),[81-84] Rockwell,[56] Leti,[85] and DRS[35] in multispectral HgCdTe detectors employing mainly MBE (although LPE and MOCVD are also used) for the growth of a variety of devices. The QWIP technology also demonstrates considerable progress in the fabrication of multicolor FPA's.[4,5,35,58,86-90] Devices for the sequential and simultaneous detection of two closely spaced subbands in the MWIR and LWIR radiation bands have been demonstrated.

A. Dual-band HgCdTe

In backilluminated dual-band detectors, the photodiode with the longer cutoff wavelength is grown epitaxially on top of the photodiode with the short cutoff wavelength. The shorter-cutoff photodiode acts as a long-wavelength-pass filter for the longer-cutoff photodiode.

Both sequential mode and simultaneous mode detectors are fabricated from multilayer materials. The simplest two-color HgCdTe detector, and the first to be demonstrated, is the bias-selectable $n-p-n$ back-to-back photodiode shown in Fig. 33(a). The sequential-mode detector has a single indium bump per unit cell that permits sequential bias selectivity of the spectral bands associated with the operating tandem photodiodes. When the polarity of the bias voltage applied to the bump contact is positive, the top (LW) photodiode is reverse biased and the bottom (SW) photodiode is forward biased. The SW photocurrent is shunted by the low impedance of the forward-biased SW photodiode, and the only photocurrent to emerge in the external circuit is the LW photocurrent. When the bias voltage polarity is reversed, the situation reverses; only the SW photocurrent is available. Switching times within the detector can be relatively short, on the order of microseconds, so the detection of slowly changing targets or imagers can be done by switching rapidly between the MW and LW modes.

One bump contact per unit cell, as for single-color hybrid FPA's, is a big advantage of a bias-selectable detector. It is compatible with existing silicon readout chips. The problems with bias selectable devices are the following: their construction does not allow independent selection of the optimum bias voltage for each photodiode, and there can be substantial MW crosstalk in the LW detector.
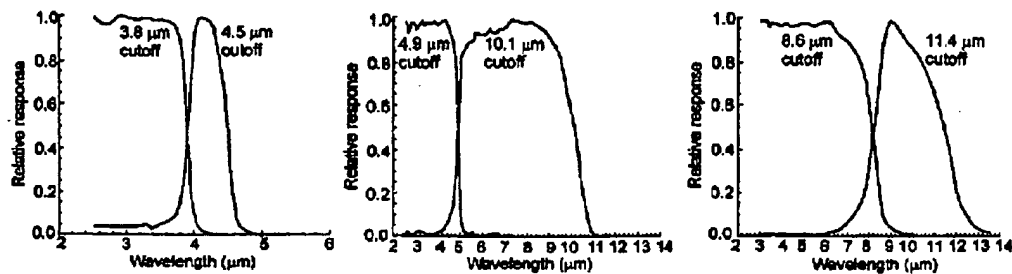
FIG. 34. Spectral response curves for two-color HgCdTe detectors in various dual-band combinations of MWIR and LWIR spectral bands (after Ref. 38).

Many applications require true simultaneity of the detection in the two spectral bands. This has been achieved in a number of ingenious architectures schematically shown, after Reine,[91] in Figs. 33(b)–33(e). All these simultaneous dual-band detector architectures require an additional electrical contact to the underlying layer in the multijunction structure of both the SW and LW photodiodes. The most important distinction is the requirement of a second readout circuit in each unit cell.

Integrated two-color HgCdTe technology has been under development for nearly a decade with steady progress and now boasts a wide variety of pixel sizes (30–61 μm), array formats (64×64 up to 320×240) and spectral-band sensitivity (MWIR/MWIR, MWIR/LWIR, and LWIR/LWIR). Figure 34 shows examples of the spectral response from different two-color devices. Note that there is minimal cross talk between the bands, since the short-wavelength band absorbs nearly 100% of the shorter wavelengths. One might question whether the additional processing and complexity of building a two-color detector structure might adversely affect the performance, yield, or operability of two-color devices. Test structure indicates that the separate photodiodes in a two-color detector perform exactly as single-color detectors in terms of the achievable R_0A product variation with wavelength at a given temperature. For example, fill factors of 128×128 MWIR/MWIR FPA's as high as 80% were achieved using a single mesa structure to accommodate two

indium bump contacts required for each unit cell with the size of 50 μm. Band 1 (2.5–3.9 μm) had the operability of 99.9%, with 23 inoperable pixels. Band 2 (3.9–4.6 μm) had the operability of 98.9%, with 193 inoperable pixels. Quantum efficiencies of 70% were observed in each band without the use of an antireflection coating. The R_0A values for the diodes ranged from 8.25×10^5 to 1.1×10^6 Ω cm^2 at $f/2$ FOV. The NEDT for both bands is shown in Fig. 35 as a function of temperature. The camera used for these measurements had a 50 mm, $f/2.3$ lens. Imagery was acquired at temperatures as high as 180 K with no visible degradation in image quality.

Recently, Rockwell has developed a novel simultaneous two-color MWIR/LWIR FPA technology based on a double-layer planar heterostructure (DLPH) MBE technology [see Fig. 33(e)]. To prevent the diffusion of carriers between two bands, a wide-band-gap 1-μm-thick layer separates these absorbing layers. The diodes are formed by implanting arsenic as a p-type dopant and activating it with an anneal. This results in a unipolar operation for both bands. The implanted area of band 2 is a concentric ring around the band 1 dimple. Because the lateral carrier-diffusion length is larger than the pixel pitch in the MWIR material and band 1 junction is shallow, each pixel is isolated by dry-etching a trench around it to reduce the carrier cross talk. The entire structure is capped with a layer of a material with a slightly wider band gap to reduce surface recombination and simplify passivation. Two-color 128×128 FPA's with low background lim-
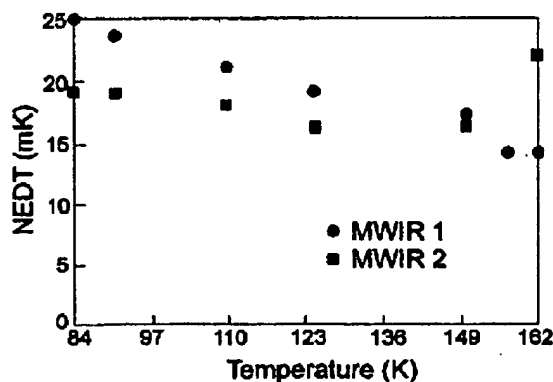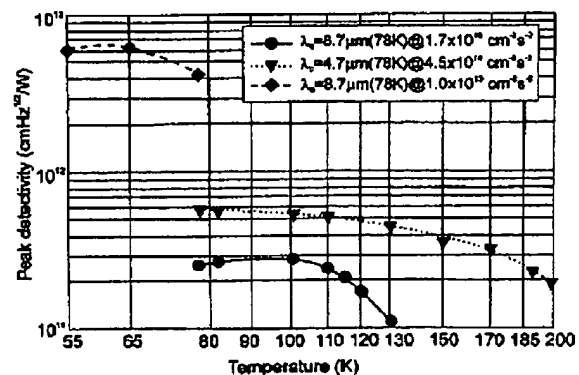

FIG. 35. NEDT for a two-color camera having 50 mm, $f/2.3$ lens, as a function of the operating temperature (after Ref. 38).

FIG. 36. Detectivity of two-color MWIR/LWIR 128×128 HgCdTe FPA (after Ref. 56).
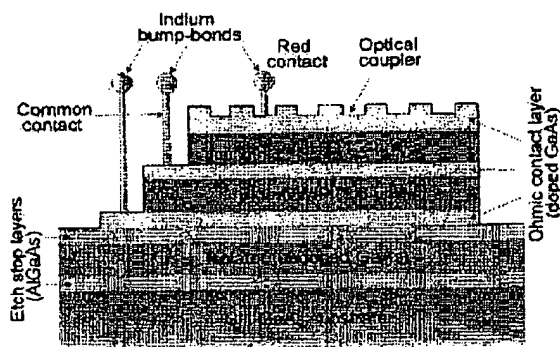
FIG. 37. Structure of a two-color stacked QWIP (after Ref. 86).

FIG. 39. Simultaneous images from 256×256 MWIR/LWIR QWIP FPA's. Note appearance of the filter and the soldering iron in the two bands (after Ref. 86).

ited detectivity performance (10^{13} cm^{-2} s^{-1}) have been obtained for the MWIR (3–5 μm) regime at $T < 130$ K and for LWIR (8–10 μm) at $T \approx 80$ K (see Fig. 36). The pixels exhibit BLIP performance up to 120 K for the two bands. The FPA also exhibits low NEDT values: 9.3 mK for the MW band and 13.3. mK for the LW band, similarly to good-quality single-color FPA's.

B. Multiband QWIP's

Sanders was the first to fabricate two-color, 256×256 bound-to-miniband QWIP FPA's in each of four important combinations: LWIR/LWIR, MWIR/LWIR, near IR (NIR)/LWIR, and MWIR/MWIR—with simultaneous integration.[58,86]

Devices capable of simultaneously detecting two separate wavelengths can be fabricated by vertically stacking different QWIP layers during epitaxial growth. Separate bias voltages can be applied to each QWIP simultaneously via the doped contact layers that separate the MQW detector heterostructures. Figure 37 shows schematically the structure of a two-color stacked QWIP with contacts to all three ohmic-contact layers. The device epilayers were grown by MBE on a 3-in. semi-insulating GaAs substrate. An undoped GaAs layer, called an isolator, was grown between two AlGaAs stop layers, followed by an Au/Ge ohmic contact of a 0.5-μm-thick doped GaAs layer. Next, two QWIP heterostruc-

tures were grown, separated by another ohmic contact. The stack sensitive to long wavelengths (red QWIP, $\lambda_c = 11.2$ μm) is grown above that sensitive to shorter wavelengths (blue QWIP, $\lambda_c = 8.6$ μm). Each QWIP is a 20-period GaAs/ Al$_x$Ga$_{1-x}$As MQW stack in which the thickness of the Si-doped GaAs QW's (with a typical electron concentration of 5×10^{17} cm^{-3}) and the Al composition of the undoped Al$_x$Ga$_{1-x}$As barriers ($\approx$550–600 Å) is adjusted to yield the desired peak position and spectral width. The gaps between FPA detectors and the readout multiplexer were backfilled with epoxy. The epoxy backfilling provides the necessary mechanical strength to the detector array and a readout hybrid prior to the array's thinning process.

Most QWIP arrays use a 2D grating, which is very wavelength dependent, and the efficiency gets lower when the pixel size gets smaller. Lockheed Martin used rectangular and rotated rectangular 2D gratings for their two-color LW/LW FPA's. Although random reflectors have achieved relatively high quantum efficiencies with a large test device structure, it is not possible to achieve similarly high quantum efficiencies with random reflectors on small FPA pixels due to the reduced width-to-height aspect ratios.[5] In addition, it is difficult to fabricate random reflectors for shorter-wavelength detectors, when compared to long-wavelength detectors, due to the fact that feature sizes of random reflectors are linearly proportional to the peak wavelength of the detectors. The quantum efficiency becomes a more difficult issue for QWIP multicolor FPA's than for single-color ones.

Typical operating temperatures for QWIP detectors are in the range of 40–100 K. The bias across each QWIP can be adjusted separately, although it is desirable to apply the same bias to both colors. As is shown in Fig. 38, the responsivity of both QWIP's is around 300–350 mA/W. The spectral response is relatively narrow so that a detector designed for the LWIR band only detects light in that band with little or no "spectral cross talk" with a detector in the MWIR band. It appears that the complex two-color processing has not compromised the electrical and optical quality of either color in the two-color device since the peak quantum efficiency for each of the 20-period QWIP's was estimated to be $\approx$10%. For comparison, a normal single-color QWIP with twice the number of periods has a quantum efficiency of around 20%. A pixel operability for each color is >97% in comparison to a value higher than 99.9% routinely achieved for single-color
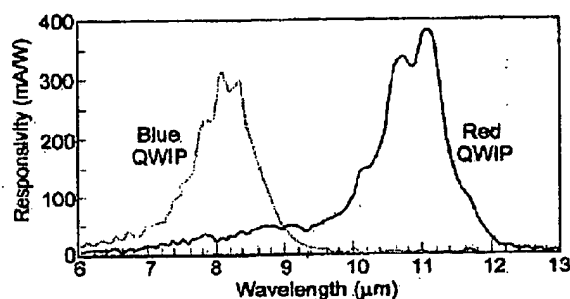

FIG. 38. Typical responsivity spectra at 40 K and a common bias of 1.5 V, recorded simultaneously for two QWIP's in the same pixel (after Ref. 86).

8-9 µm QWIP

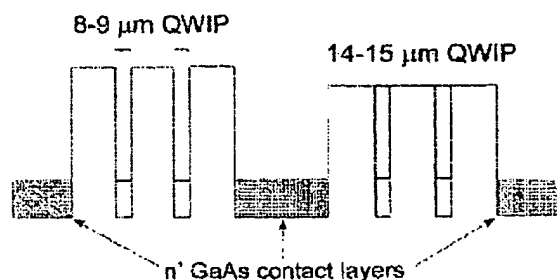**14-15 µm QWIP**

n' GaAs contact layers

FIG. 40. Conduction band diagram of a LWIR and a VLWIR two-color detector (after Ref. 93).

QWIP's. The NEDT value was 24 mK for the blue QWIP and 35 mK for the red QWIP. The difference was attributed to the poor transmission properties of the optics in the 11.2 µm band.

To cover the MWIR range, a strained layer of the InGaAs/AlGaAs material system is used. InGaAs in the MWIR stack produces a high, in-plane, compressive strain which enhances the responsivity.[86,92] The MWIR/LWIR FPA's fabricated by Sanders consist of an 8.6-µm GaAs/AlGaAs QWIP on top of a 4.7-µm strained InGaAs/GaAs/AlGaAs heterostructure. The fabrication process allowed fill factors of 85% and 80% to be achieved for the MW and LW detectors, respectively. The first FPA's with this configuration had an operability in excess of 97% and NETD values greater than 35 mK. The excellent imagery in each color is shown in Fig. 39. Note the appearance of the filter and the soldering iron in the two bands.

Recently, Gunapala et al.[77,93] have demonstrated the first 8–9 and 14–15 µm two-color imaging camera based on a 640×486 dual-band QWIP FPA, which can be equipped with dual or triple contacts to access the CMOS readout multiplexer. A single indium bump per pixel is usable only in the

case of the interlace readout scheme (i.e., odd rows for one color and even rows for the other), which uses a existing single-color CMOS readout multiplexer. However, the disadvantage is that it does not provide the full fill factor for both wavelength bands.

The device structure shown in Fig. 40 consists of a 30-period stack (500 Å AlGaAs barrier and a 60 Å GaAs well) of the VLWIR structure and a second 18-period stack (500 Å AlGaAs barrier and a 40 Å GaAs well) of the LWIR structure separated by a heavily doped 0.5-µm-thick intermediate GaAs contact layer. The VLWIR QWIP structure has been designed to have a bound-to-quasibound intersubband absorption peak at 14.5 µm, whereas the LWIR QWIP structure has been designed to have a bound-to-continuum intersubband absorption peak at 8.5 µm, because the photocurrent and the dark current of the LWIR device structure are relatively small compared to those of the VLWIR portion of the device structure.

Figure 41 shows a schematic side view of an interlace dual-band GaAs/AlGaAs FPA. Two different 2D periodic grating structures were designed to independently couple the 8–9 µm and 14–15 µm radiation to detector pixels in the even and odd rows of the FPA. The top 0.7-µm-thick GaAs cap layer was used to fabricate the light-coupling 2D periodic gratings for 8–9 µm detector pixels, whereas the light-coupling 2D periodic gratings of the 14–15 µm detector pixels were fabricated using LWIR MQW layers. In such a way, this grating scheme short circuited all the detector sensitive to the 8–9 µm radiation in all odd rows of the FPA. Next, the LWIR detector pixels were fabricated by dry etching the photosensitive GaAs/AlGaAs MQW layers into the 0.5-µm-thick doped GaAs intermediate contact layer. All VLWIR pixels in the even rows of the FPA were short-circuited. The VLWIR detector pixels were fabricated by dry etching both MQW stacks into the 0.5-µm-thick heavily doped GaAs bottom contact layer. After epoxy backfilling of

Rows

Columns

Light coupling gratings

Short circuited   14-15 µm VLWIR   Short circuited   14-15 µm VLWIR

Even   Odd   Even   Odd

22 µm
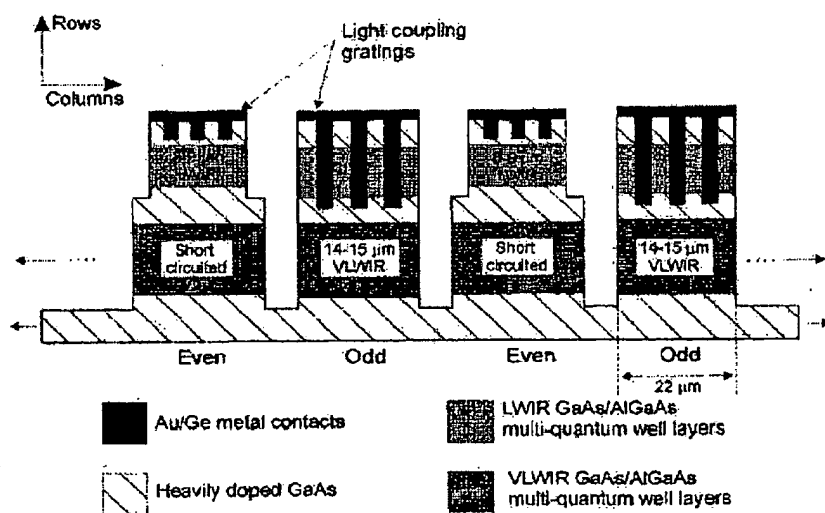
FIG. 41. Structure cross section of the interlace dual-band FPA (after Ref. 93).

■ Au/Ge metal contacts

▨ Heavily doped GaAs

▨ LWIR GaAs/AlGaAs multi-quantum well layers

▨ VLWIR GaAs/AlGaAs multi-quantum well layers

A. Rogalski

TABLE VII. Performance specifications for two-color long wavelength 640×486 QWIP FPA's (after Ref. 93).

Parameter	LWIR pixels (8–9 μm)	VLWIR pixels (14–15 μm)
Array size	640×486	
Pixel pitch (μm)	25×25	25×25
Pixel size (μm)	23×23	22×23
Optical coupling	2D periodic grating	2D periodic grating
Operating temperature (K)	40	40
Differential resistance (Ω) at f/2 FOV	2.0×10^{12}	7.0×10^{11}
Peak wavelength (μm)	8.4	14.4
Peak responsivity (mA/W) at $V_B = -2$ V	509	382
Cutoff wavelength, 50% (μm)	9.1	15.0
Operability (%)	99.7	98.0
Uncorrected nonuniformity (%)	5.4	
Corrected uniformity, 17–27 °C (%)	0.03	
Quantum efficiency (%)	12.9	8.9
Uncorrected nonuniformity of η (%)	2	1
D_{BB}^* (cm Hz$^{1/2}$ W^{-1}) at f/2 FOV	2.9×10^{10}	1.1×10^{10}
NEDT with f/2 optics (mK)	29	74

the gaps between FPA detectors and the readout multiplexer, the substrate was thinned and finally the remaining GaAs/AlGaAs material contained only the QWIP pixels and a very thin membrane ($\approx$1000 Å). This allows the whole structure to adapt to the thermal expansion, eliminates thermal mismatch between the silicon readout and the detector array, eliminates pixel-to-pixel crosstalk, and finally, significantly enhances the optical coupling of IR radiation to QWIP pixels. The FPA was back illuminated through a flat thinned substrate membrane.

The 640×486 GaAs/AlGaAs gave excellent images with 99.7% of the LWIR pixels and 98% of VLWIR pixels working, demonstrating the high yield of GaAs technology. The 8–9 μm detectors have shown background limited performance (BLIP) at 70 K (at a background temperature of 300 K with a f/2 cold stop). The 14–15 μm detectors show BLIP at 45 K with the other operating conditions unchanged. At temperatures below 70 K, the signal-to-noise ratio of the LWIR detector pixels is limited by the array nonuniformity, multiplexer readout noise, and photocurrent noise (for the f/2 cold stop). At temperatures above 70 K, the temporal noise due to the higher dark current of QWIP's (thermionic emission) becomes the limitation. At temperatures below 40 K,

the signal-to-noise ratio of the VLWIR detector pixels is limited by the array nonuniformity, multiplexer readout noise, and photocurrent noise.

The performance of these dual-band FPA's was tested at a background temperature of 300 K, with a f/2 cold stop, and at a 30 Hz frame rate The results are described in Table VII. The estimated NEDT of the LWIR and VLWIR detectors at 40 K is 36 and 44 mK, respectively. Due to BLIP, the estimated and experimentally obtained NEDT values of the LWIR detectors do not change significantly at temperatures below 65 K. The experimentally measured values of LWIR NEDT equal to 29 mK are lower than the estimated ones [see Fig. 42(a)]. This improvement is attributed to the light-coupling efficiency of the 2D periodic grating. However, the experimental VLWIR NEDT value [see Fig. 42(b)] is higher than the estimated value. It is probably the result of inefficient light coupling in the 14–15 μm region, readout multiplexer noise, and the noise of the proximity electronics. At 40 K, the performance of both types of detector pixels is limited by the photocurrent noise and the readout noise.

At present, a joint Goddard/Jet Propulsion Laboratory/Army Research Laboratory proposal to develop a four band, hyperspectral, 640×512 QWIP array is funded by the Earth
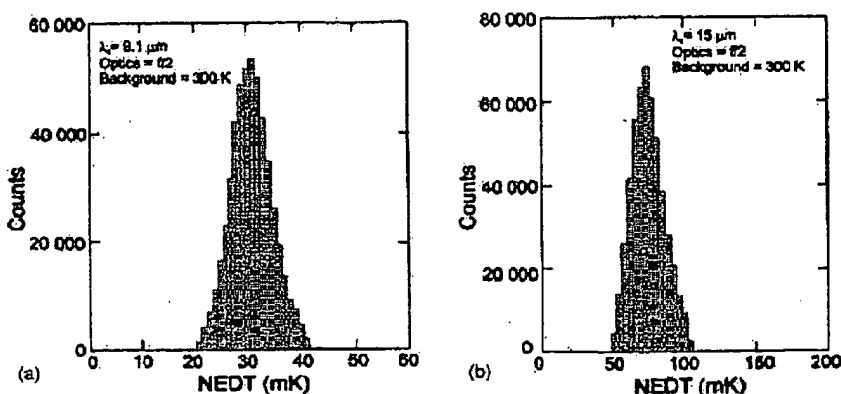

FIG. 42. The uncorrected NEDT histograms of 8–9 μm detector pixels (a) and 14–15 μm detector pixels (b) of 640×486 dual-band FPA. The mean NEDT are 29 mK for LWIR FPA and 74 mK for VLWIR FPA (after Ref. 93).

A. Rogalski   4383

Science Technology Office of NASA.[90] The four bands of the QWIP array are fabricated in a manner similar to the two-band system described above (see Fig. 41). The four-detector bands are delineated by a deep groove etch to contact a specific band, while shorting out the other three-band layers. Experiments are in progress to determine the optimum coupling surface treatment and both grating and corrugation methods are being considered.

The three-year effort will focus on expanding the spectral imaging capability of the integrated QWIP, utilizing a new Sunpower, Inc. Cryocooler, and developing a linear variable etalon to produce a hyperspectral image from 3 to 15.4 μm. The four IR bands are 3–5 μm, 8.5–10 μm, 10–12 μm, and 14–15.4 μm. These bands are spectrally subdivided into approximately 200 bands. The technical goals are listed below:

    (i) array size: 512×640, 23 μm pixels,

    (ii) 4 IR bands: (1) 3–5 μm, (2) 8.5–10 μm, (3) 10–12 μm, (4) 14–15.4 μm,

    (iii) format: each band contains 128×640 pixels,

    (iv) operating temperature: 43 K (mechanical cryocooler),

    (v) f/4, fully reflective optics,

    (vi) FOV: 25.7°,

    (vii) wavelength resolution: 0.02 μm at 3 μm to 0.05 μm at 15.4 μm,

    (viii) resolving power, $\lambda/\Delta\lambda$: >100 in all bands,

    (ix) NEDT<0.020 K,

    (x) frame rates up to 30/s, variable integration time,

    (xi) $D^* > 10^{13}$ cm Hz$^{1/2}$/W at 3 μm to $D^* > 2 \times 10^{11}$ cm Hz$^{1/2}$/W at 14 μm.

Assuming successful development of the Hyperspectral QWIP Imager, this instrument is intended to fly on the NASA ER-2 (U2 Plane) to perform high altitude remote sensing of a variety of earth science parameters.

The presented results indicate that QWIP's have shown much progress in recent years in terms of their applications in the multiband imaging problem. It is the niche in which they have an intrinsic advantage due to the relative ease of growing multiband structures by MBE with very low defect density.
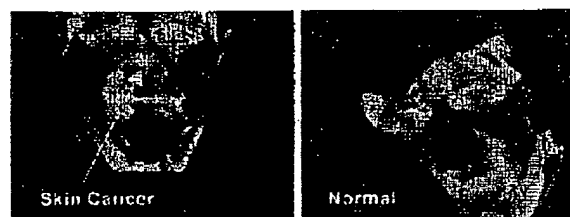
VI. QWIP APPLICATIONS

FIG. 43. (a) This clearly shows the tip of the nose is warmer than the surrounding tissue due to the enhanced metabolic activity (angiogenesis) of a skin cancer. (b) Shows a face with no skin cancer on the nose. Usually, nose and ears are cooler relative to the other parts of the face, because those extend out of the body (after Ref. 5).

where r is the ratio of the photocurrent to the dark current and u is the nonuniformity. The first term in the square brackets is the temporal noise and the second term is the fixed pattern noise.

In general, higher quantum efficiency improves all of these figures of merit. The minimum NEDT can be achieved by having a smaller g. Higher gain increases the photocurrent and, therefore, the speed. However, the resulting higher $g-r$ noise reduces the sensitivity. Since the gain is given by the ratio of the electron lifetime to the transit time, higher lifetime increases the photocurrent with respect to the dark current (i.e., the value of r) and therefore is able to increase the operating temperature (T_{BLIP} is its value when $r=1$). A short transit time, in turn, increases the photocurrent and the dark current in equal proportion, and therefore does not affect the operating temperature. If high speed and high operating temperature are essential, high quantum efficiency and gain is required. However, high quantum efficiency does not reduce NEDT once the detection is background limited (e.g., $r>1$).

QWIP technology is accepted as the commercial standard for high-performance and large-format LWIR detection. Gunapala et al.[5,87] presented large-format QWIP cameras holding forth a promise for many applications in the 6–18 μm wavelength range in science, medicine, defense, and industry. Possible applications are medical imaging,[5,87,95] fire fighting,[5,87] monitoring volcano activities,[5,87] IR astronomy,[5,87,96] national and tactical missile defense,[5,87,97] monitoring heat emission in certain geological areas, hyper-
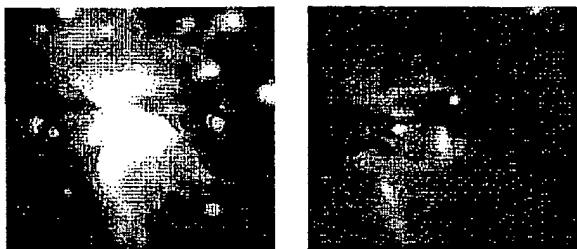
FIG. 44. Comparison of a composite near-infrared image obtained by 2MASS (a), with an 8.5-μm LWIR image (b) obtained with a QWIP FPA at primary focus of the Palomar 5-m hale telescope. The S106 region displays vigorous star formation obscured behind dense molecular gas and cold dust, and extended nebular emission from dust heated by starlight. Thermal-infrared imaging can be used to assess the prevalence of warm (≈300 K) dusty disks surrounding the stars in such regions. Formation of these disks is an evolutionary step in the development of planetary systems (after Ref. 5).

about 15 mK measured with a $f/2$ 50 mm lens at a 20-ms integration time. QWIP is the only large format detector with great stability that fulfills this requirement. Moreover, the cost of a similar HgCdTe array is at least 10 times the cost of a comparable QWIP detector. The overall camera system cost will, as a result, increase by a factor of 2, which becomes very important from the point of view of producing a cost-effective medical imaging system.

It has been found that cancer cells exude nitric oxide, which causes changes of the blood flow in the tissue surrounding a cancer that can be detected by a sensitive thermal sensor. Recently, a midformat QWIP has been used in an instrument called BioScan System for dynamic area telethermometry (DAT).[5,87] DAT involves the accumulation of hundreds of consecutive IR images and fast Fourier transform analysis of the biomodulation of skin temperature and micro-homogeneity of skin temperature, which measures the perfusion of the skin's capillaries. The BioScan System can be also used in breast tumor detection, brain surgery, skin cancer detection, and leprosy treatment. In general, cancerous cells have a high metabolic rate and these cancerous cells recruit new blood supply; one of the characteristic of a malignant lesion. Therefore cancerous tissues are slightly warmer than the neighboring healthy tissues. Thus, a sensitive thermal imager can easily detect malignant skin cancers (see Fig. 43).

B. Astronomy

QWIP's are attractive for use in astronomy because they offer good sensitivity, are very stable, are large-size devices that can be easily manufactured, and their operating temperatures are relatively high when compared to standard extrinsic silicon photoconductors used for astronomy goals (e.g., Si:As). Because of the narrow spectral range, QWIP's with a cutoff wavelength of 10 μm operate at 25–30 K and are able to satisfy stringent dark current requirements, such as those imposed on the Next Generation Space Telescope (NGST).[96] Other important properties of QWIP's are (i) extremely low 1/f noise and (ii) easy mating to existing CMOS multiplexers

(since QWIP's are thin-layer structures, thermal mismatch may cause certain difficulties; 1024×1024 pixel devices are planned).

The first astronomical observations with a QWIP FPA were described by Gunapala et al.[5,87] An 8–9-μm 256 ×256 QWIP-based astronomical wide-field multicolor camera built at the Jet Propulsion Laboratory (JPL) has been designated for operation at the $f/3$ prime focus of the Palomar 5-m telescope. Operation at the prime focus affords a very wide FOV; 2 minutes of arc compared to 10–30 seconds of arc for traditional ground-based MWIR instruments. Figure 44 compares the composite near-infrared image (a) obtained by 2MASS, with an 8.5 μm LWIR image (b) obtained with a QWIP FPA at the primary focus of the Palomar 5-m hale telescope. These images demonstrate the advantage of large format, stable (low 1/f noise) LWIR QWIP FPA's in surveying obscured regions in search for embedded or reddened objects such as young forming stars.

The JPL camera is designated to house up to three QWIP devices:[96] the existing 256×256 pixel 8.5-μm device, a 640×512 pixel, 12.5-μm device, and a 10.3-μm device of unspecified format. This arrangement will allow simultaneous three-color imaging and enable rapid selection of interesting objects based on their MWIR colors. The selection of three bands is motivated by the properties of both the astronomical objects and the Earth's atmosphere. It has been found that many objects enshrouded in dust, exhibit a strong silicate absorption. The strength of this absorption peaks at 9.7 μm. The transmission of the atmosphere is, in turn, characterized by a strong ozone feature at 9.5–10.0 μm. Water vapor produces strong absorption at wavelengths <8 μm and CO_2 absorbs wavelengths >13 μm. To obtain the best sensitivity, a compromise solution has been chosen to design QWIP's with the peak response at 8.5, 10.3, and 12. 5 μm.

It is expected that QWIP's may have an even greater role to play in space-borne missions because of their higher operating temperatures. Examples of such missions (NGST and Interstellar Probe) were described by Ressler et al.[96]

An impressive program of QWIP FPA's applications at the NASA/Goddard Space Flight Center was presented by Jhabvala.[90] The future of QWIP's at Goddard is diverse and still unfolding. The Hyperspectral QWIP Imager was developed to perform high altitude remote sensing.

C. Defense

The missile defense systems performed either in the endoatmosphere or exoatmosphere. Endoatmospheric interceptors and airborne surveillance sensors used for tactical applications typically observe warm targets with high background irradiance. Such applications require accurate measurement and subtraction of background irradiance to detect the target signal. In contrast, exoatmospheric interceptors and space-based surveillance sensors used for strategic applications typically engage cool targets with low-background irradiance levels. The targets are often far away and unresolved at the early stage of detection. In strategic applications, where the scene is a space background and the targets are at relatively low temperatures, LWIR and VLWIR are very important

A. Rogalski   4385
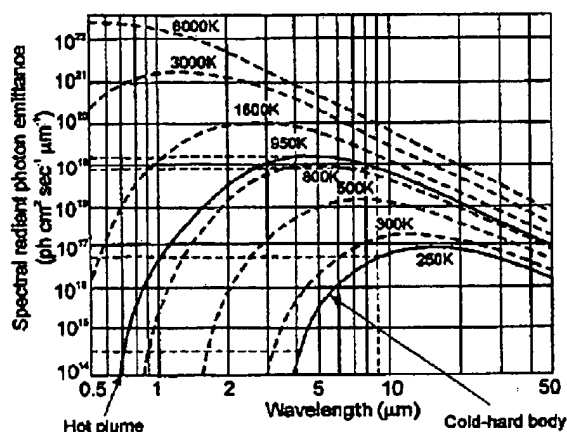
FIG. 45. Blackbody spectral radiant emittance at various temperatures (after Ref. 5).

FIG. 47. Schematic of the IR heterodyne and microwave mixing experiment. The measured signals, in general, consist of all possible mixing frequencies of two infrared and one microwave frequency (after Ref. 100).

bands. Improvement in surveillance sensors and interceptor seekers requires highly uniform large-area, multispectral IR FPA's covering the LWIR and VLWIR regions. The restrictions imposed on pixel uniformity in strategic IR FPA's are much more severe, because dead or degraded pixels could cause the target to be missed completely, and absolute radiometry, not imagery, is the method by which most target information is obtained. The space-based FPA's are usually designed with larger pixels, roughly equal to the blur spot of the optics. Taking into account the advantages of QWIP technology (large and uniform arrays), the Ballistic Missile Defense Organization (BMDO) supported extensive efforts to develop highly sensitive large FPA's based on QWIP's.[32,33,97]
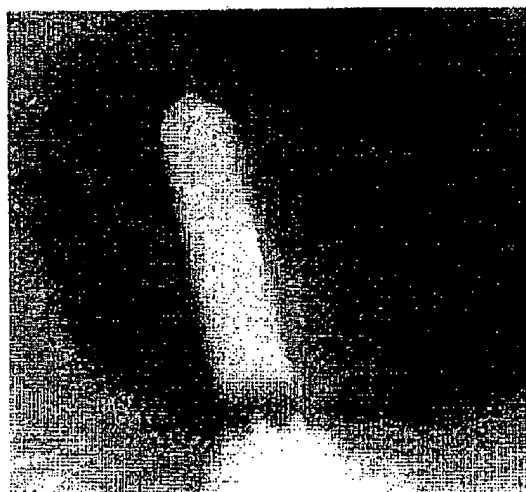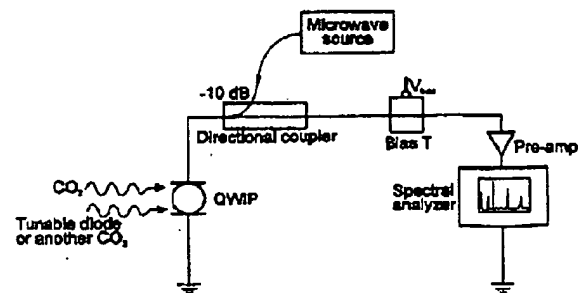

FIG. 46. Image of a Delta-II launch vehicle taken with the LW QWIP RADIANCE during the launch. This clearly indicates the advantage of LW QWIP cameras in the discrimination and identification of a cold-launch vehicle in the presence of a hot plume during early stages of launch (after Ref. 5).

The operating temperature and cooldown time constitute a major consideration in such systems as missile seekers. Reconnaissance systems, however, require medium to large format FPA's and use closed-cycle cooling to reach operating temperatures of 77 K. The extra time and power needed to lower the temperature (e.g., 65 K for LWIR QWIP operation) is not significant if the integrated dewar/cooler assembly is designed well. In spite of theoretical speculations, it has not been shown conclusively that running a modern closed-cycle cooler at temperatures below 77 K degrades the life expectancy of the cooler.

A QWIP RADIANCE camera was used by the researchers at BMDO in a unique experiment to discriminate and identify clearly a cold-launch vehicle against its hot plume emanating from rocket engines. The temperature of cold-launch vehicles is usually about 250 K, whereas the temperatures of the hot plume emanating from the launch vehicle may reach 950 K. Figure 45 indicates that the 4-μm photon flux ratio of blackbodies at 250 K and 950 K, respectively is about 25 000, whereas the same photon flux ratio at 8.5 μm is about 115. Therefore it is very clear that one must explore longer wavelengths for better discrimination between cold-body and hot plume because the highest instantaneous dynamic range of IR cameras is usually 12 bits (i.e., 4096) or less. Figure 46 shows the image of Delta-II launch taken with a QWIP RADIANCE camera.

D. High-frequency detection

Certain applications that were previously not feasible with HgCdTe detectors, the maximum electrical bandwidth of which remains approximately at 3 GHz,[7,98] are now possible with QWIP's. When a CO_2-laser local oscillator (LO) with HgCdTe detector is used for molecular spectroscopy, for example, the molecular line of interest must be within roughly 3 GHz of a CO_2 emission line. Because these emission lines are typically separated by at least 30 GHz, the vast majority of the frequency space between 9 and 11 μm is undetectable. A similar problem occurs when a HgCdTe detector is used as a front-end mixer in coherent laser communications, where the maximum digital transmission rate is approximately 1 Gb/s.

In comparison with HgCdTe-based technology, GaAs/AlGaAs QWIP's offer several advantages: higher electrical
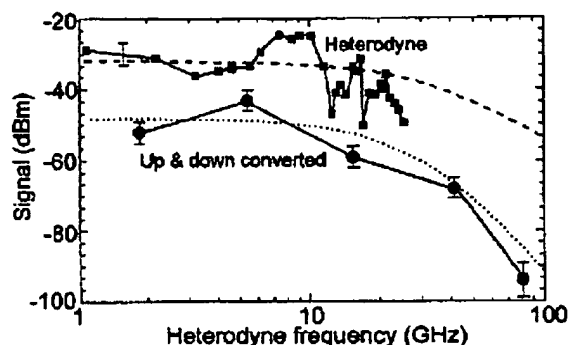
A. Rogalski

FIG. 48. Direct infrared heterodyne (squares) and mixed heterodyne frequency with microwave frequency (dots) signal vs heterodyne frequency for a bias voltage of 2 V. The dashed and dotted lines show the expected roll-off behavior. The incident power from the two infrared sources and the microwave source is normalized to about 0.2 and 0.3 mW, respectively. The device temperature is 80 K (after Ref. 100).

bandwidth, greater robustness and tolerance to high levels of LO power, and monolithic compatibility with GaAs HEMT amplifiers.[99,100] The intrinsic high-speed capability is due to the inherently short carrier lifetime $\tau \sim 5$ ps.

In optical mixing experiments described in Ref. 101, a CO_2 laser and a lead-salt tunable diode laser (TDL) were used as the sources of IR radiation. The CO_2 laser frequency was fixed, while the TDL frequency was tuned by varying its operating temperature. Liu et al.[102] carried out experiments with an intermediate frequency (IF) of up to 26.5 GHz.

Far beyond 26.5 GHz a direct measurement of the IF signal is very difficult because of two impediments; namely, the lack of a sufficiently sensitive preamplifier-analyzer combination and the difficulty in making a low-loss, broadband circuit that can be used to couple the weak IF signal from the QWIP. To extend the frequency range, Liu et al.[103] used a microwave mixing technique shown schematically in Fig. 47. The technique is based on the nonlinearity present in the $I-V$ curves of QWIP's associated with the transport of electrons in the absence of IR radiation. Because of this nonlinearity, the microwave signal is rectified and the measured change of the bias voltage is the response. As is shown in Fig. 47, apart from two IR beams (as in conventional hetero-

dyne experiments), an additional microwave excitation is applied to the QWIP. Let f_{IR1} and f_{IR2} denote the two IR frequencies and $f_{\mu wave}$ the microwave frequency. The IR heterodyne frequency is then $f_{het} = |f_{IR1} - f_{IR2}|$, while the downconverted signal frequency is $|f_{het} - f_{\mu wave}|$. In this heterodyne detection technique very high f_{het} frequencies up to 82.16 GHz have been achieved. The measured optical heterodyne signal (squares) and the up- and downconverted mixing signal (dots) are shown in Fig. 48 as a function of heterodyne frequency (f_{het}) for a bias voltage of 2 V. The dashed and dotted lines are the expected roll-off behaviors due to the resistance-capacitance (RC) time constant of the device and the photocarrier lifetime.

E. Market data

From a market perspective, the QWIP technology is still in its infancy, although it is on the brink of acceptance.[104] The QWIP detector process methodology developed at JPL, culminating in the fabrication of midformat (256×256), portable LWIR cameras, has been transferred to the commercial environment through QWIP Technologies LLC under agreement with Caltech. At present, QWIP Technologies LLC is involved in high-volume III-V-material processes developed for the cellular communications industry. The first product is the QWIP-Chip, a 320×256 format QWIP FPA spectrally centered at 8.5 μm with a 30-μm pitch. Production ramped up to 100 QWIP-Chips per month by the first quarter of 2001. Also QWIP Technologies has begun low rate initial production of its second product in the QWIP-Chips line, a 640×512 QWIP FPA.

The high-performance military market is currently dominated by other, more expensive technologies. This stance is, however, changing in favor of larger staring arrays and less expensive imagers, like those using QWIP FPA's.

In the U.S. alone, billions of dollars are spent annually on various types of imaging systems. In 2001, over $2 billion was spent on IR imaging systems, and the market is forecast to grow by 31% annually between 1999 and 2004 (see Fig. 49). In 1996, IR FPA market was predominantly military (80% compared to 20% commercial). It is expected to change to 66% military and 34% commercial by 2004.

VII. CONCLUSIONS

The intention of this paper has been to compare the achievements of QWIP technology with those of competitive technologies, with the emphasis on the material properties, device structure, and their impact on FPA performance, especially in LWIR and VLWIR spectral regions.

At present, HgCdTe is the most widely used variable-gap semiconductor that has a privileged position both in the LWIR as well as VLWIR spectral ranges. The above discussion leads to a conclusion that LWIR QWIP cannot compete with HgCdTe photodiode as single devices, especially at higher operation temperatures (>70 K), due to the fundamental limitations associated with intersubband transitions. However, the advantage of HgCdTe is less distinct at temperatures below 50 K due to the problems inherent in the
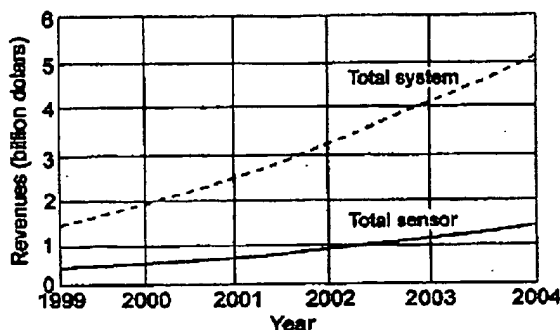

FIG. 49. Sensors and systems revenues from 1999 to 2004 (after Ref. 104).

HgCdTe material (p-type doping, Shockley-Read recombination, trap-assisted tunneling, surface and interface instabilities).

Comparing photovoltaic HgCdTe and QWIP technologies, we arrive at the following conclusions:

(i) Two major issues that impede the performance of QWIP's should be overcome: optical conversion efficiency and dark current.

(ii) In the case of HgCdTe, the improvement in the array uniformity is necessary.

(iii) QWIP seems to have more potential for LWIR and VLWIR FPA operation (also with multicolor detection).

The main drawback of LWIR QWIP FPA technology is that the device performance is limited to long integration time applications and low operating temperature. The main advantages are linked to the performance uniformity and to the ease of fabrication of large size arrays. The large industrial infrastructure in III-V material/device growth, processing, and packaging brought about by the extensive application of GaAs-based devices in the telecommunications industry gives QWIP's a potential advantage in producibility and cost. The only known use of HgCdTe, to date, is IR detectors. The main drawback of LWIR HgCdTe FPA technology is the unavailability of large size arrays necessary for TV and larger format.

Even though QWIP is a photoconductor, several of its properties, such as high impedance, fast response time, long integration time, and low power consumption, comply well with the requirements imposed on the fabrication of large FPA's. Due to a high material quality at low temperatures, QWIP has potential advantages over HgCdTe in the area of VLWIR FPA applications in terms of the array size, uniformity, yield, and cost of the systems. QWIP FPA's combine the advantages of PtSi Schottky barrier arrays (high uniformity, high yield, radiation hardness, large arrays, lower cost) with the advantages of HgCdTe (high quantum efficiency and long-wavelength response). It is also anticipated that the inherent QWIP polarization sensitivity can be exploited in IR imaging systems to discriminate between targets and decoys.

The performance figures of merit of state-of-the-art QWIP and HgCdTe FPA's are similar because the main limitations come from the readout circuits. Performance is, however, achieved with very different integration times. The very short integration time of LWIR HgCdTe devices (typically below 300 μs) is very useful to freeze a scene with rapidly moving objects. Due to excellent homogeneity and low photoelectrical gain, QWIP devices achieve an even better NEDT; the integration time, however, must be 10–100 times longer and typically is between 5 and 20 ms. The choice of the best technology is therefore driven by the specific needs of a system. Observation of the global market for the last few years indicates that even though LWIR HgCdTe photodiodes exhibit intrinsically higher performance than that of QWIP detectors, the market tendencies for the future are (i) HgCdTe for small formats (e.g., 128×128), small pitch, high frame rates, and low integration times, and (ii) QWIP for large formats (e.g., 640×480 and larger), low frame rates, and large integration time.

Powerful possibilities of the QWIP technology are associated with VLWIR FPA applications and multicolor detection. Three-band and four-band FPA's have been demonstrated.

Until now, efforts in the area of QWIP technology have been limited to increasing the operation temperature for tactical applications. The discussion presented in this paper indicates, however, that more effort should be directed toward developing QWIP for VLWIR strategic applications.

Despite serious competition from alternative technologies and progress slower than expected, HgCdTe is unlikely to be seriously challenged as far as high-performance applications (requiring multispectral capability and fast response) are concerned. The recent successes of competing detectors cooled cryogenically are due to technological, not fundamental issues. The steady progress in epitaxial technology can make HgCdTe devices much more affordable in the future. The much higher operation temperature of HgCdTe, compared to low-dimensional solid devices, may become a decisive argument in this case.

APPENDIX

1. Noise equivalent difference temperature

Detectivity provides only a limited insight into the suitability of IR detectors for specific IR systems. The objective criterion of performance of imaging devices is the noise equivalent difference temperature (NEDT); i.e., the difference in temperature of an object required to produce an electric signal equal to the rms noise voltage. While normally thought of as a system parameter, detector NEDT and system NEDT are the same except for system losses. NEDT is defined as

$$\text{NEDT} = \frac{V_n(\partial T/\partial Q)}{(\partial V_s/\partial Q)} = V_n \frac{\Delta T}{\Delta V_s}, \tag{A1}$$

where V_n is the rms noise and ΔV_s is the signal measured for the temperature difference ΔT. It can be shown that[105]

$$\text{NEDT} = (\tau C \eta_{BLIP} \sqrt{N_w})^{-1}, \tag{A2}$$

where C is the thermal contrast which in the MWIR band at 300 K is 3.5%–4% compared to 1.6% for the LWIR band. N_w is the number of photogenerated carriers integrated for one integration time t_{int}:

$$N_w = \eta A_d t_{int} Q_B. \tag{A3}$$

The percentage of BLIP, η_{BLIP}, is simply the ratio of photon noise to composite FPA noise:

$$\eta_{BLIP} = \left(\frac{N_{photon}^2}{N_{photon}^2 + N_{FPA}2} \right)^{1/2}. \tag{A4}$$

It results from the above formulas that the charge handling capacity of the readout, the integration time linked to the frame time, and dark current of the sensitive material become the major issues of IR FPA's. The NEDT is inversely proportional to the square root of the integrated charge, and therefore the greater the charge, the higher the performance.

A. Rogalski

The distinction between integration time and FPA's frame time must be noted. At high backgrounds it is often impossible to handle the large amount of carriers generated over a frame time compatible with standard video rates. Off-FPA frame integration can be used to attain a level of sensor sensitivity that is commensurate with the detector-limited D^* and not the charge-handling-limited D^*.

a. Photon detectors

The sensitivity of an IR system can be expressed in a variety of ways.[106] In this paper we follow the paper recently published by Kinch.[20]

The limiting factor of detector sensitivity is the fluctuation in the relevant carrier concentration since this determines the minimum observable signal. This fluctuation is envisioned by assuming that the detector current is integrated on a capacitive node, giving a variance

$$N^{1/2} = g\left[\frac{(I_d + I_B)\tau_{\text{tot}}}{q}\right]^{1/2},\qquad (A5)$$

where g is the gain, I_d is the detector dark current, I_B is the background flux current, and τ_{int} is the integration time.

The noise equivalent flux (also named as the minimum observable signal) is given by

$$g\Delta\Phi\,\eta\tau_{\text{int}}A = N^{1/2},\qquad (A6)$$

where η represents the overall quantum efficiency of the detector, including the internal quantum efficiency. Using last two equations, the noise equivalent flux can be described as

$$\Delta\Phi = \frac{g(1 + I_d/I_\Phi)\Phi_B}{N^{1/2}}.\qquad (A7)$$

Because

$$\Delta\Phi = \frac{\Delta T}{d\Phi_B/dT},\qquad (A8)$$

if we substitute the above, we have for the noise equivalent difference temperature

$$NEDT = \frac{g(1 + I_d/I_\Phi)\Phi_B}{(d\Phi_B/dT)N^{1/2}},\qquad (A9)$$

where $(d\Phi_B/dT)/\Phi_B = C$ is the scene contrast. For unlimited available capacity, $N^{1/2}$ varies as g, and $\Delta\Phi$ and NEDT are independent of the gain g. However, for a limited maximum well capacity N, both bandwidth (Δf) and NEDT will vary as g. These parameters depend on specific system and detector quantities such as area and bandwidth, where bandwidth is defined as $\Delta f = 1/2\tau$.

b. Thermal detectors

In the case of a thermal detector, the limiting temperature fluctuation is given by[16,18]

$$\Delta T_n = \left(\frac{4kT^2 R_{th}\Delta f}{1 + \omega^2\tau_{th}^2}\right)^{1/2}.\qquad (A10)$$

At low frequencies $\Delta T_n = (4kT^2 R_{th}\Delta f)^{1/2}$. It appears that correlated double sampling of this limitation with an integrated time τ_{int}, gives[20]

$$\Delta T_n = \left[\frac{2kT^2[1 - \exp(-\tau_{int}/R_{th}C_{th})]}{C_{th}}\right]^{1/2},\qquad (A11)$$

where it is assumed $\Delta f = 1/R_{th}C_{th}$. Comparing Eq. (A11) with a signal fluctuation change given by

$$\Delta T_s = \left(\frac{dP}{dT}\right)\Delta T\left[1 - \exp\left(-\frac{\tau_{int}}{R_{th}C_{th}}\right)\right]R_{th},\qquad (A12)$$

one obtains

$$NEDT = \left[\frac{2kT^2}{C_{th}[1 - \exp(-\tau_{int}/R_{th}C_{th})]}\right]^{1/2}\frac{1}{(dP/dT)R_{th}},\qquad (A13)$$

where (dP/dT) is the differential change in radiated power per scene temperature change in the spectral region of interest. The integration time should fulfill the condition $\tau_{int} \approx 2R_{th}C_{th}$ to avoid image smearing. The maximum value of R_{th} is given by the radiative coupling with the upper limit equal 4×10^8 K/W for a 1 mil pixel size. For micromachined resonant cavity bolometers with $f/1$ optics, there is a finite limit of detector thickness. Typically $t = 3000$ Å. For 1 mil pixel size a volumetric specific heat is about 2 J/cm^3 K.

2. GaAs/AlGaAs QWIP's

a. Thermal generation

The carrier generation rate from the QW's due to optical phonons may be obtained as[107]

$$G_{phon} = N_{QW}\frac{n_{s2}}{\tau},\qquad (A14)$$

where N_{QW} is the number of QW's, n_{s2} is the 2D density of carriers originating from the excited subband state, and τ is the lifetime of electrons in the upper state. It can be shown that

$$n_{s2} = L_p 2\left(\frac{2\pi m^* kT}{h^2}\right)^{3/2}\exp\left(-\frac{V_b - E_F}{kT}\right),\qquad (A15)$$

$$\tau = \frac{4h\epsilon_p\Delta E_{co}L_p}{q^2 E_{phon}I_1}.\qquad (A16)$$

In these equations, L_p is the mean well spacing, m^* is the electron effective mass, k is the Boltzmann constant, E_{phon} is the phonon energy, and I_1 is a dimensionless integral close to 2 in the 8–12 μm range for a quasibound upper state. Moreover, ΔE_{co} is the cutoff energy defined as $\Delta E_{co} = hc/\lambda_c = V_b - E_1$ (V_b is the barrier energy of the QW, and λ_c is the cutoff wavelength), $1/\epsilon_p = 1/\epsilon_\infty - 1/\epsilon_0$ (ϵ_∞ and ϵ_0 is the dielectric permittivity at infinite and zero frequency, respectively),

$$E_F - E_1 = \frac{n_{s1}h^2}{4\pi m^*},\qquad (A17)$$

is the Fermi energy of the well, and n_{s1} is the 2D carrier density in the ground state. It should be noted that G_{phon}

does not depend on L_p and is therefore a more fundamental quantity of a QWIP, in contrast to n_{s2} and τ. The following parameters have been assumed: $m^* = 0.067 m_0$, $\epsilon_p = 63 \epsilon_0$, $E_{phon} = 36$ meV, $n_s = 2 \times 10^{11}$ cm^{-2}, and $N_{QW} = 50$.

b. Quantum efficiency

An unpolarized double-pass quantum efficiency (at a 45° angle of incidence) is equal to

$$\eta = \frac{1 - \exp(-2\alpha l)}{2},$$

(A18)

where l is the total active superlattice length. The factor of 2 in the exponent of Eq. (A18) accounts for a double pass and the factor 2 in the denominator accounts for the unpolarized beam.

As Levine has discussed, the behavior of η results from the fact that the net quantum efficiency is composed of two components. One is the optical absorption quantum efficiency η_a (e.g., the fraction of the unpolarized incident photons which are absorbed by the intersubband transition). The other factor is the probability p_e that a photoexcited electron will escape from the quantum well and contribute to the photocurrent, rather than being recaptured by the originating well. That is, we can express the total (net) quantum efficiency η as

$$\eta = \eta_a p_e.$$

(A19)

For bound-to-continuum transitions, p_e varies from 34% to 52% at low bias and increases toward unity at high bias.

3. HgCdTe photodiodes

The Auger mechanism is more likely to impose fundamental limitations to the LWIR HgCdTe detector performance.[108] Assuming a nondegenerate statistic, the Auger generation rate is equal to

$$G_A = \frac{n}{2\tau_{A1}^j} + \frac{p}{2\tau_{A7}^j} = \frac{1}{2\tau_{A1}^j}\left(n + \frac{p}{\gamma}\right),$$

(A20)

where n and p are the electron and hole concentrations, τ_{A1}^j and τ_{A7}^j are the intrinsic Auger 1 and Auger 7 recombination times, and $\gamma = \tau_{A7}^j/\tau_{A1}^j$ is the ratio of Auger 7 an Auger 1 intrinsic recombination times. τ_{A1}^j is given by

$$\tau_{A1}^j = \frac{3.8 \times 10^{-18} \epsilon_s^2 (1+\mu)^{1/2}(1+2\mu)\exp\left[\left(\frac{1+2\mu}{1+\mu}\right)\frac{E_g}{kT}\right]}{(m_e^*/m)|F_1 F_2|^2 (kT/E_g)^{3/2}},$$

in s,

(A21)

where $\mu = m_e^*/m_h^*$ is the ratio of the conduction to the heavy-hole valence-band effective masses, ϵ_s is the relative static dielectric constant, and F_1 and F_2 are the overlap integrals of the periodic part of the electron wave functions. The value of $|F_1 F_2|$ is taken as a constant equal to 0.2. The γ term is of high uncertainty. According to Casselman and Petersen[109] for Hg$_{1-x}$Cd$_x$Te over the range $0.16 \leqslant X \leqslant 0.40$ and 50 K $\leqslant T \leqslant 300$ K, $3 \leqslant \gamma \leqslant 6$.

The Auger-dominated detectivity is equal to

$$D^* = \frac{\lambda}{2^{1/2}hc} \frac{\eta}{t^{1/2}}\left(\frac{\tau_{A1}^j}{n + p/\gamma}\right)^{1/2}.$$

(A22)

The resulting Auger generation achieves its minimum for $p = \gamma^{1/2}n_i$. Since $\gamma > 1$, the highest detectivity of Auger limited photodetectors can be achieved with a light p-type doping.

The required $\gamma^{1/2}n_i$ p-type doping is difficult to achieve in practice for low-temperature photodetectors (the control of hole concentration below the 5×10^{15} cm^{-3} level is difficult) and the p-type material suffers from some nonfundamental limitations such as contacts, surface, and Shockley–Read processes. These are the reasons why the low-temperature detectors are typically produced from lightly doped n-type materials. In contrast, p-type doping is clearly advantageous for LWIR and near room-temperature detectors.

Rogalski and Ciupa[39] have compared the performance of $n^+ - p$ and $P^+ - n$ LWIR HgCdTe photodiodes. It appears, that for the lowest doping levels achievable in a controllable manner in the base regions of photodiodes ($N_a = 5 \times 10^{15}$ cm^{-3} for n^+-p structure, and $N_d = 5 \times 10^{14}$ cm^{-3} for P^+ $-n$ structure) the performance of both types of photodiodes is comparable for a given cutoff wavelength and temperature.

4. InSb photodiodes

InSb photodiodes are generally fabricated by impurity diffusion and ion implantation. Epitaxy is not used; instead, the standard manufacturing technique begins with bulk n-type single-crystal wafers with a donor concentration of about $N_d = 10^{15}$ cm^{-3}. The Shockley–Read recombination centers are an intrinsic characteristic of n-type InSb. The electron and hole lifetimes are equal because in n-type material there is a single set of recombination centers. The electron and hole carrier lifetimes of high-quality material at temperatures below 130 K obey the expression[110]

$$\tau = \frac{4.4 \times 10^8}{N_d}, \quad \text{in s}$$

(A23)

The thermal generation can be described by

$$G_{th} = \frac{n_i^2}{N_d \tau}.$$

(A24)

5. Extrinsic photoconductors

At the low temperature of operation of impurity photoconductors (when $kT \ll E_d$ and $n \ll N_d$, N_a), the thermal equilibrium free-charge carrier in an n-type extrinsic semiconductor with a partially compensated singly ionized level is equal to[111,112]

$$n_{th} = n_{maj} = \frac{N_c}{2}\left(\frac{N_d - N_a}{N_a}\right)\exp\left(-\frac{E_d}{kT}\right).$$

(A25)

Here N_c is the density of states in the conduction band, N_d is the donor concentration, N_a is the compensating acceptor concentration, and E_d is the bonding energy of the donor relative to the conduction band.

The majority carrier lifetime is determined by the density of empty (ionized) donor levels and, for low temperatures, such that $n_{maj} < N_a < N_d$, is given by

$$\tau = (\sigma_c v_{th} N_a)^{-1}, \tag{A26}$$

where σ_c is the capture cross section for electrons into the donor level, and $v_{th} = (8kT/\pi m^*)^{1/2}$ is the carrier thermal velocity. For shallow-level impurities (B and As) typically, $\sigma_c \approx 10^{-11}$ cm^2, while for the deep-level impurities (In, Au, Zn) show, $\sigma_c = 10^{-13}$ cm^2. By comparison, the σ_c of intrinsic photoconductors is about 10^{-17} cm^2.

Practical values of α for optimized extrinsic silicon photoconductors are in the range 10–50 cm^{-1}. To maximize the quantum efficiency, the thickness of the detector crystal should be not less than about 0.1 cm. Typical quantum efficiencies are in range of 10%–50% at the response peak.

[1] L. Esaki and R. Tsu, IBM J. Res. Dev. 14, 61 (1970).
[2] B. F. Lovine, J. Appl. Phys. 74, R1 (1993).
[3] S. D. Gunapala and K. M. S. V. Bandara, in Thin Films, edited by M. H. Francombe and J. L. Vossen (Academic Press, New York, 1995), Vol. 21, p. 113.
[4] S. D. Gunapala and S. V. Bandara, in Handbook of Thin Devices, edited by M. H. Francombe (Academic Press, San Diego, 2000), Vol. 2, p. 63.
[5] S. D. Gunapala, S. V. Bandara, J. K. Liu, E. M. Luong, S. B. Rafol, J. M. Mumolo, D. Z. Ting, J. J. Bock, M. E. Ressler, M. W. Werner, P. D. LeVan, R. Chehayeb, C. A. Kukkonen, M. Ley, P. LeVan, and M. A. Fauci, Opto-Electron. Rev. 8, 150 (2001).
[6] M. Razeghi, Opto-Electron. Rev. 6, 155 (1998).
[7] A. Rogalski, Infrared Detectors (Gordon and Breach, Amsterdam, 2000).
[8] A. Rogalski, K. Adamiec, and J. Rutkowski, Narrow-Gap Semiconductor Photodiodes (SPIE Press, Bellingham, 2000).
[9] A. Rogalski, Sens. Mater. 12, 233 (2000).
[10] R. A. Wood and N. A. Foss, Laser Focus World, 101 (1993).
[11] P. W. Kruse, Uncooled Thermal Imaging: Arrays, Systems, and Applications (SPIE Press, Bellingham, 2001).
[12] A. Rose, Concepts in Photoconductivity and Allied Problems (Interscience, New York, 1963).
[13] J. Piotrowski and W. Gawron, Infrared Phys. Technol. 38, 63 (1997).
[14] J. Piotrowski and A. Rogalski, Sens. Actuators A 67, 146 (1998).
[15] R. G. Humphreys, Infrared Phys. 26, 337 (1986).
[16] P. W. Kruse, L. D. McGlauchlin, and R. B. McQuistan, Elements of Infrared Technology (Wiley, New York, 1962).
[17] P. W. Kruse, in Optical and Infrared Detectors edited by R. J. Keyes (Springer-Verlag, Berlin, 1977), p. 5.
[18] A. Smith, F. E. Jones, and R. P. Chasmar, The Detection and Measurement of Infrared Radiation (Clarendon, Oxford, 1968).
[19] R. Ciupa and A. Rogalski, Opto-Electron. Rev. 5, 257 (1997).
[20] M. A. Kinch, J. Electron. Mater. 29, 809 (2000).
[21] T. Ashley and C. T. Elliott, Electron. Lett. 21, 451 (1985).
[22] F. Fuchs, L. Bürkle, R. Hamid, N. Herres, W. Pletschen, R. E. Sah, R. Kiefer, and J. Schmitz, Proc. SPIE 4288, 171 (2001).
[23] J. Piotrowski and A. Rogalski, J. Appl. Phys. 80, 2542 (1996).
[24] B. F. Levine, K. K. Choi, C. G. Bethea, J. Walker, and R. J. Malik, Appl. Phys. Lett. 50, 1092 (1987).
[25] M. B. Reine, in Infrared Detectors and Emitters: Materials and Devices, edited by P. Capper and C. T. Elliott (Chapman and Hall, London, 2000), p. 279.
[26] J. Y. Andersson, L. Lundqvist, and Z. F. Paska, Appl. Phys. Lett. 58, 2264 (1991).
[27] G. Sarusi, B. F. Levine, S. J. Pearton, K. M. S. V. Bandara, and R. E. Leibenguth, Appl. Phys. Lett. 64, 960 (1994).
[28] C. J. Chen, K. K. Choi, M. Z. Tidrow, and D. C. Tsui, Appl. Phys. Lett. 68, 1446 (1997).
[29] S. S. Li and Y. H. Wang, in Quantum Well Intersubband Transition Physics and Devices, edited by H. C. Liu, B. F. Levine, and J. Y. Anderson (Kluwer Academic, Dordrecht, 1994), p. 29.
[30] M. A. Kinch and A. Yariv, Appl. Phys. Lett. 55, 2093 (1989).
[31] A. Rogalski, Infrared Phys. Technol. 38, 295 (1997).
[32] M. Z. Tidrow, in Proceedings of the 6th Annual AIAA/BMDO Technology Readiness Conference and Exhibit, San Diego, CA, 1997.
[33] M. Z. Tidrow, W. A. Beck, W. W. Clark, H. K. Pollehn, J. W. Little, N. K. Dhar, P. R. Leavitt, S. W. Kennerly, D. W. Beekman, A. C. Goldberg, and W. R. Dyer, Opto-Electron. Rev. 7, 283 (1999).
[34] A. Rogalski, Infrared Phys. Technol. 40, 279 (1999).
[35] A. C. Goldberger, S. W. Kennerly, J. W. Little, H. K. Pollehn, T. A. Shafer, C. L. Mears, H. F. Schaake, M. Winn, M. Taylor, and P. N. Uppal, Proc. SPIE 4369, 532 (2001).
[36] D. W. Beekman and J. Van Anda, Infrared Phys. Technol. 42, 323 (2001).
[37] M. Z. Tidrow, Proc. SPIE 2999, 109 (1996).
[38] P. R. Norton, Proc. SPIE 3379, 102 (1998).
[39] A. Rogalski and R. Ciupa, J. Appl. Phys. 77, 3505 (1995).
[40] A. Rogalski and R. Ciupa, J. Appl. Phys. 80, 2483 (1996).
[41] S. M. Johnson, D. R. Rhiger, J. P. Rosbeck, J. M. Peterson, S. M. Taylor, and M. E. Boyd, J. Vac. Sci. Technol. B 10, 1499 (1992).
[42] M. C. Chen, R. S. List, D. Chandra, M. J. Bevan, L. Colombo, and H. F. Schaake, J. Electron. Mater. 25, 1375 (1996).
[43] R. S. List, J. H. Tregilgas, A. M. Turner, J. D. Beck, and J. C. Ehmke, Proc. SPIE 2228, 274 (1994).
[44] W. E. Tennant, C. A. Cockrum, J. B. Gilpin, M. A. Kinch, M. B. Reine, and R. P. Ruth, J. Vac. Sci. Technol. B 10, 1359 (1992).
[45] M. B. Reine, K. R. Maschhoff, S. P. Tobin, P. W. Norton, J. A. Mroczkowski, and E. E. Krueger, Semicond. Sci. Technol. 8, 788 (1993).
[46] J. Bajaj, J. M. Arias, M. Zandian, J. G. Pasko, L. J. Kozlowski, R. E. De Wames, and W. E. Tennant, J. Electron. Mater. 24, 1067 (1995).
[47] S. D. Gunapala, J. K. Liu, J. S. Park, M. Sundaram, C. A. Shott, T. Hoelter, T. L. Lin, S. T. Massie, P. D. Maker, R. E. Muller, and G. Sarusi, IEEE Trans. Electron Devices 44, 51 (1997).
[48] M. Z. Tidrow, J. C. Chiang, S. S. Li, and K. Bacher, Appl. Phys. Lett. 70, 859 (1997).
[49] A. Singh and M. O. Manasreh, Proc. SPIE 2397, 193 (1995).
[50] S. V. Bandara, S. D. Gunapala, S. Rafol, D. Ting, J. Liu, J. Mumolo, T. Trinh, A. W. K. Liu, and J. M. Fastenau, Infrared Phys. Technol. 42, 237 (2001).
[51] L. J. Kozlowski, K. Vural, J. M. Arias, W. E. Tennant, and R. E. DeWames, Proc. SPIE 3182, 2 (1997).
[52] P. Norton, J. Campbell, S. Horn, and D. Reago, Proc. SPIE 4130, 226 (2000).
[53] J. D. Benson, J. H. Dinan, J. Waterman, C. J. Summers, R. D. Benz, B. K. Wagner, S. D. Pearson, A. Parikh, J. J. Jensen, O. K. Wu, R. D. Rajavel, G. S. Kamath, K. A. Harris, S. R. Jost, J. M. Arias, L. J. Kozlowski, M. Zandian, J. Bajaj, K. Vural, R. E. DeWames, C. A. Cockrum, G. M. Venzor, S. M. Johnson, H. D. Shih, M. J. Bevan, J. A. Dodge, and A. Simmons, Proc. SPIE 2744, 126 (1996).
[54] O. K. Wu, T. J. DeLyon, R. D. Rajavel, and J. E. Jensen, in Narrow-Gap II–VI Compounds for Optoelectronic and Electromagnetic Applications, edited by P. Capper (Chapman and Hall, London, 1997), p. 97.
[55] T. J. DeLyon, J. E. Jensen, M. D. Gorwitz, C. A. Cockrum, S. M. Johnson, and G. M. Venzor, J. Electron. Mater. 28, 705 (1999).
[56] W. E. Tennant, M. Thomas, L. J. Kozlowski, W. V. McLevige, D. D. Edwall, M. Zandian, K. Spariosu, G. Hildebrandt, V. Gil, P. Ely, M. Muzilla, A. Stoltz, and J. H. Dinan, J. Electron. Mater. 30, 590 (2001).
[57] S. M. Johnson, J. L. Johnson, W. J. Hamilton, D. B. Leonard, T. A. Strand, A. E. Patten, J. M. Peterson, J. H. Durham, V. K. Randall, T. J. de Lyon, J. E. Jensen, and M. D. Gorwitz, J. Electron. Mater. 29, 680 (2000).
[58] W. A. Beck and T.S. Faska, Proc. SPIE 2744, 193–206 (1996).
[59] S. D. Gunapala, J. S. Park, G. Sarusi, T. L. Lin, J. K. Liu, P. D. Maker, R. E. Muller, C. A. Shott, and T. Hoelter, IEEE Trans. Electron Devices 44, 45 (1997).
[60] S. D. Gunapala, S. V. Bandara, J. K. Liu, W. Hong, M. Sundaram, P. D. Maker, R. E. Muller, C. A. Shott, and R. Carralejo, IEEE Trans. Electron Devices 45, 1890 (1998).
[61] S. D. Gunapala, S. V. Bandara, J. K. Liu, E. M. Luong, N. Stetson, C. A. Shott, J. J. Bock, S. B. Rafol, J. M. Mumolo, and M. J. McKelvey, IEEE Trans. Electron Devices 47, 326 (2000).
[62] H. Schneider, M. Walther, C. Schönbein, R. Rehm, J. Fleissner, W. Pletschen, J. Braunstein, P. Koidl, G. Weimann, J. Ziegler, and W. Cabanski, Physica E (Amsterdam) 7, 101–107 (2000).
[63] H. Schneider, M. Walther, J. Fleissner, R. Rehm, E. Diwo, K. Schwarz, P. Koidl, G. Weimann, J. Ziegler, R. Breiter, and W. Cabanski, Proc. SPIE 4130, 353 (2000).
[64] H. Schneider, P. Koidl, M. Walther, J. Fleissner, R. Rehm, E. Diwo, K. Schwarz, and G. Weimann, Infrared Phys. Technol. 42, 283 (2001).

[65] H. Schneider, C. Schönbein, M. Walther, K. Schwarz, J. Fleissner, and P. Koidl, Appl. Phys. Lett. 71, 246 (1997).

[66] P. Bois, E. Costard, X. Marcadet, and E. Herniou, Infrared Phys. Technol. 42, 291 (2001).

[67] A. Manissadjian, P. Costa, P. Tribolet, and G. Destefanis, Proc. SPIE 3436, 150 (1998).

[68] G. Destefanis, P. Audebert, E. Mottin, and P. Rambaud, J. Cryst. Growth 184/185, 1288 (1998).

[69] A. Singh and D. A. Cardimona, Proc. SPIE 2999, 46 (1997).

[70] D. A. Cardimona, A. Singh, D. Huang, C. Morath, and P. Varangis, Infrared Phys. Technol. 42, 211 (2001).

[71] L. J. Kozlowski, S. A. Cabelli, D. E. Cooper, and K. Vural, Proc. SPIE 1946, 199 (1993).

[72] L. J. Kozlowski, Proc. SPIE 3179, 200 (1997).

[73] L. J. Kozlowski, R. B. Bailey, S. E. Cooper, I. S. Gergis, A. C. Chen, W. V. McLevige, G. L. Bostrup, K. Vural, W. E. Tennant, and P. E. Howard, Opt. Eng. (Bellingham) 33, 54 (1994).

[74] J. P. Chatard, Proc. SPIE 3698, 407 (1999).

[75] P. Bertrand, J.T. Tissot, and G. Destefanis, in Physics of Semiconductor Devices, edited by V. Kumar and S.K. Agarwal (Narosa Publishing House, New Delhi, 1998), Vol. II, p. 713.

[76] J. M. Fastenau, W. K. Liu, X. M. Fang, D. I. Lubyshev, R. I. Pelzel, T. R. Yurasits, T. R. Stewart, J. H. Lee, S. S. Li, and M. Z. Tidrow, Infrared Phys. Technol. 42, 407 (2001).

[77] S. D. Gunapala, S. V. Bandara, A. Singh, J. K. Liu, B. Rafol, E. M. Luong, J. M. Mumolo, N. Q. Tran, D. Z. Ting, J. D. Vincent, C. A. Shott, J. Long, and P. D. LeVan, IEEE Trans. Electron Devices 47, 963 (2000).

[78] R. D. Rajavel, D. M. Jamba, O. K. Wu, J. E. Jensen, J. A. Wilson, E. A. Patten, K. Kosai, P. Goetz, G. R. Chapman, and W. A. Radford, J. Cryst. Growth 175, 653 (1997).

[79] R. D. Rajavel, D. M. Jamba, J. E. Jensen, O. K. Wu, P. D. Brewer, J. A. Wilson, J. L. Johnson, E. A. Patten, K. Kasai, J. T. Caulfield, and P. M. Goetz, J. Cryst. Growth 184, 1272 (1998).

[80] R. D. Rajavel, D. M. Jamba, J. E. Jensen, O. K. Wu, J. A. Wilson, J. L. Johnson, E. A. Patten, K. Kasai, P. M. Goetz, and S. M. Johnson, J. Electron. Mater. 27, 747 (1998).

[81] M. B. Reine, P. W. Norton, R. Starr, M. H. Weiler, M. Kestigian, B. L. Musicant, P. Mitra, T. Schimert, F. C. Case, I. B. Bhat, H. Ehsani, and V. Rao, J. Electron. Mater. 24, 669 (1995).

[82] P. Mitra, S. L. Barnes, F. C. Case, M. B. Reine, P. O'Dette, R. Starr, A. Hairston, K. Kuhler, M. H. Weiler, and B. L. Musicant, J. Electron. Mater. 26, 482 (1977).

[83] M. B. Reine, A. Hairston, P. O'Dette, S. P. Tobin, F. T. J. Smith, B. L. Musicant, P. Mitra, and F. C. Case, Proc. SPIE 3379, 200 (1998).

[84] H. K. Pollehn and J. Ahearn, Proc. SPIE 3698, 420 (1999).

[85] J. P. Zanatta, P. Ferret, R. Loyer, G. Petroz, S. Cremer, J. P. Chamonal, P. Bouchut, A. Million, and G. Destefanis, Proc. SPIE 4130, 441 (2000).

[86] T. Whitaker, Compound Semicond. 5(7), 48 (1999).

[87] S. D. Gunapal, S. V. Bandara, J. K. Liu, E. M. Luong, S. B. Rafol, J. M.

Mumolo, D. Z. Ting, J. J. Bock, M. E. Ressler, M. W. Werner, P. D. LeVan, R. Chehayeb, C. A. Kukkonen, M. Levy, P. LeVan, and M. A. Fauci, Infrared Phys. Technol. 42, 267 (2001).

[88] M. Sundaram, S. C. Wang, M. F. Taylor, A. Reisinger, G. L. Milne, K. B. Reiff, R. E. Rose, and R. R. Martin, Infrared Phys. Technol. 42, 301 (2001).

[89] A. Goldberg, T. Fischer, S. Kennerly, W. Beck, V. Ramirez, and K. Garner, Infrared Phys. Technol. 42, 309 (2001).

[90] M. Jhabvala, Infrared Phys. Technol. 42, 363 (2001).

[91] M. B. Reine, Proc. SPIE 4288, 266 (2001).

[92] Ph. Bois, E. Costard, J. Y. Duboz, and J. Nagle, Proc. SPIE 3061, 764 (1997).

[93] S. D. Gunapala, S. V. Bandara, A. Sigh, J. K. Liu, S. B. Rafol, E. M. Luong, J. M. Mumolo, N. Q. Tran, J. D. Vincent, C. A. Shott, J. P. LeVan, Proc. SPIE 3698, 687 (1999).

[94] K. K. Choi, Proc. SPIE (to be published).

[95] M. A. Fauci, R. Breiter, W. Cabanski, W. Fick, R. Koch, J. Ziegler, and S. D. Gunapala, Infrared Phys. Technol. 42, 337 (2001).

[96] M. E. Ressler, J. J. Bock, S. V. Bandara, S. D. Gunapala, and M. W. Werner, Infrared Phys. Technol. 42, 377 (2001).

[97] M. Z. Tidrow and W. R. Dyer, Infrared Phys. Technol. 42, 333 (2001).

[98] I. McIngailis, W. E. Keicher, C. Freed, S. Marcus, B. E. Edwards, A. Sanchez, T. Yee, and D. L. Spears, Proc. IEEE 84, 227 (1996).

[99] E. R. Brown and K. A. McIntosh, in Thin Films, edited by M. H. Francombe and J. L. Vossen (Academic Press, San Diego, 1998), Vol. 23, p. 173.

[100] H. C. Liu, in Handbook of Thin Devices, edited by M. H. Francombe (Academic Press, San Diego), 2000 Vol. 2, p. 101.

[101] E. R. Brown, K. A. McIntosh, F. W. Smith, and M. J. Manfra, Appl. Phys. Lett. 62, 1513 (1993).

[102] H. C. Liu, G. E. Jenkins, E. R. Brown, K. A. McIntosh, K. B. Nichols, and M. J. Manfra, IEEE Electron Device Lett. 16, 253 (1995).

[103] H. C. Liu, J. Li, E. R. Brown, K. A. McIntosh, K. B. Nichols, and M. J. Manfra, Appl. Phys. Lett. 67, 1594 (1995).

[104] C. A. Kukkonen, M. N. Sirangelo, R. Chehayeb, M. Kaufmann, J. K. Liu, S. B. Rafol, and S. D. Gunapala, Infrared Phys. Technol. 42, 397 (2001).

[105] L. J. Kozlowski and W. F. Kosonocky, in Handbook of Optics, edited by M. Bass, E. W. Van Stryland, D. R. Williams, and W. L. Wolfe (McGraw-Hill, New York 1995), Chap. 23.

[106] J. M. Lloyd, Thermal Imaging Systems (Plenum Press, New York, 1975).

[107] J. Y. Andersson, J. Appl. Phys. 78, 6298 (1995).

[108] P. E. Petersen, in Semiconductors and Semimetals, edited by R. K. Willardson and A. C. Beer (Academic Press, New York, 1981), Vol. 18, p. 121.

[109] T. N. Casselman and P. E. Petersen, Solid State Commun. 33, 615 (1980).

[110] R. Schoolar and E. Tenescu, Proc. SPIE 686, 2 (1986).

[111] P.R. Bratt, in Semiconductors and Semimetals, edited by R.K. Willardson and A.C. Beer (Academic Press, New York, 1977), Vol. 12, p. 39.

[112] N. Sclar, Prog. Quantum Electron. 9, 149 (1984).

EXHIBIT B

For

Declaration Under 37 CFR 1.132

US Application No. 09/836,464
Reply to Final Official Action mailed on April 16, 2004

Dark curr nt m chanism and condition of background radiation limitation f n-dop d AlGaAs/GaAs quantum-w ll infrared d t ctor

J. Y. Andersson
Industrial Microelectronic Center (IMC), P.O. Box 1084, S-164 21 Kista, Sweden

The most important mechanism of dark current in n-doped quantum-well infrared photodetectors (QWIPs) is due to interaction of electrons with longitudinal optical phonons. Theoretical expressions are derived for the carrier lifetime, and for generation currents originating from both photoexcitation as well as from thermal excitation in a single quantum well. Detector gain is discussed briefly. Calculated values of thermal generation currents and the ratio of photocurrent to thermal current are found to accord well with experimental data. Finally the conditions of background radiation limitation of QWIPs are investigated and the theory gives a temperature of background radiation limitation $T_{\text{BLIP}}=81$ K for a 9 μm cutoff detector with a two-dimensional grating and optical cavity, for 300 K background temperature, optics f number=1 with 100% optical transmission, provided that a photocurrent to dark current ratio of 1 criterion is used. © *1995 American Institute of Physics.*

I. INTRODUCTION

There is a a lot of theoretical as well as practically oriented interest in long-wavelength infrared detectors based on intersubband transitions in quantum wells (QWIPs).[1,2] Usually the conduction band of n-doped AlGaAs/GaAs quantum wells (QW) has been exploited, due to the maturity of the GaAs processing technology including epitaxy of AlGaAs/GaAs, as well as the heat and radiation hardness of GaAs.

A drawback is the fairly large dark current at the desirable operating temperature around 80 K,[3] in conjunction with a low absorption coefficient. The dark current competes with photocurrent, making completely background-limited infrared photodetector (BLIP) operation possible only at temperatures around 70 K for a detector with a maximum response at about 9 μm. A large dark current is detrimental for detector array applications, due to the limited charge capacity of complementary metal–oxide–semiconductor (CMOS) readout circuits, as well as to the sensitivity to temperature fluctuations. In contrast, the signal to noise ratio is usually sufficient for the most common imaging applications. In order to improve the performance of QWIPs a thorough understanding of the dark current and gain mechanisms is essential, as well as further work on coupling of radiation into detectors.[4,5] Another detector concept which has emerged recently is the infrared hot electron transistor (IHET);[6] however, its use is hampered by the need for three terminals, which complicates both fabrication and operation. It is not discussed further in this text.

The dark current in QWIPs may have different origin such as:

(i)   phonon excitation;
(ii)   defect-assisted tunneling; and
(iii) coherent tunneling from the ground state of the QWs.

Dark current due to the last two mechanisms can be reduced or eliminated by proper design of the QW structure, e.g., by using pure materials and thick enough barriers separating the QWs. The first mechanism still remains and is the major source of dark current for 8–12 μm detectors at temperatures>50 K.

The most prominent mechanism of electron–phonon interaction in n-doped direct-gap III–V bulk materials such as GaAs or AlAs, as well as in heterostructures consisting of such layers, is due to polar longitudinal-optical (LO) phonons. The mechanism is the Fröhlich interaction, where the lattice displacements resulting from phonons create strong electric fields which in turn interact with the electrons and cause transitions between electron states.[7,8]

The objective of this work is to find simple analytical expressions for detector parameters describing both photocurrent as well as dark current behavior. Analytical expressions are more transparent than simulation results in describing general trends, but usually more approximative than the latter. The original equations can also be used as starting points for computerized numerical simulation.

II. INTERSUBBAND RELAXATION LIFETIME AND CARRIER GENERATION RATE DUE TO POLAR OPTICAL (LO) PHONONS

Starting from basic quantum mechanics an expression for the generation rate of phonon-excited electrons (No. of excited electrons from the ground state to the extended states of the QW per unit time and QW area) is found after some approximations.

A coordinate system is defined according to Fig. 1, with the x–y plane defined by the QW plane. Starting from the golden rule of Fermi,

$$W(\mathbf{k})=\int \frac{2\pi}{\hbar}\,|\langle \mathbf{k}'|H|\mathbf{k}\rangle|^{2}[1-f(\mathbf{k}')]\delta(E'-E)\,dN', \quad (1)$$

where $W(\mathbf{k})$ is the scattering rate from the initial state, $\mathbf{k}$ and $\mathbf{k}'$ are wave vectors (of electron or phonon, or other quantum entities) describing the states, E and E' the energies, H is the perturbation Hamiltonian, $f(\mathbf{k}')$ is the occupation probability of the final state, and N' the number of final states. The
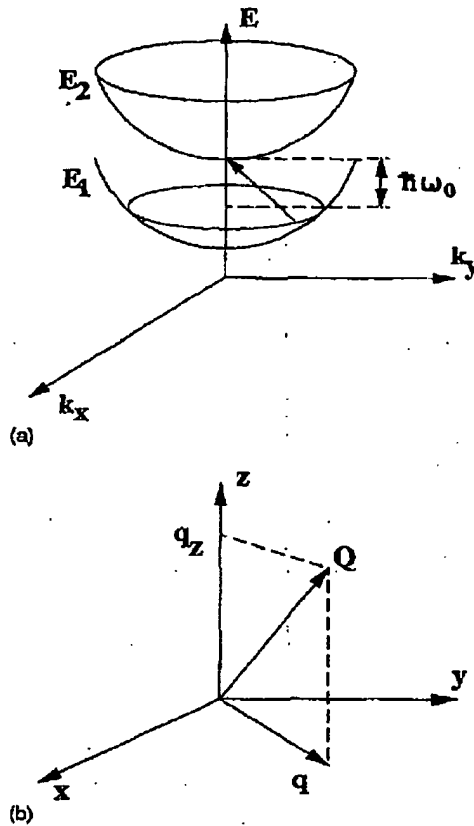
FIG. 1. (a) Scheme of the band structure of a quantum well, with a LO phonon transition from a QW ground state to an excited state subband indicated. (b) The components of the phonon wave vector Q.

primed and unprimed entities denote final and initial states of the transition, respectively. For emission processes from an upper state in a QW, $1-f(k')$ is henceforth assumed to be unity. At equilibrium conditions this is equivalent to assuming that the initial state is located far above the Fermi level, and a low enough operating temperature.

For the case of LO phonon scattering one obtains[7,8]

$$W_k = \frac{\pi e^2 \omega_0}{\Omega \epsilon_p} \int \frac{1}{Q^2} \delta_{\bar{k}\pm\bar{q}-\bar{k}',0} \cdot |M(n', \pm q_z, n)|^2$$

$$\times \left(g(\omega_0) + \frac{1}{2} \mp \frac{1}{2}\right) \delta(E' - E \mp \hbar\omega_0) dN', \quad (2)$$

where W_k is the number of transitions per unit time from the initial state described by the electron state $\bar{k}$, ω_0 the optical phonon frequency, e the electron charge, Ω the phonon cavity volume, Q the modulus of the phonon wave vector, $\bar{k}$ and $\bar{k}'$ wave vectors for electrons in the initial and final states, and g the occupation probability of phonons. It is here assumed that the latter is defined by the equilibrium Bose–Einstein distribution. Q has components q_z in the z direction and q in the $x-z$ plane. In the double signs the upper sign is for phonon absorption and the lower one for emission. This convention is retained throughout below.

It is here assumed that phonons are unconfined. A more elaborate theory would include confinement introduced by the different elastical properties of the well and barrier materials of the QWs.[9,10] Considering that for AlGaAs/GaAs QW detectors operating in the 8–12 μm range the $Al_xGa_{1-x}As$ aluminum content is usually low (x=0.2–0.3), this should be a reasonable approximation. In addition, no screening of the phonon–electron interaction is allowed for. $1/\epsilon_p = 1/\epsilon(\infty) - 1/\epsilon(0)$, where $\epsilon(\infty)$ and $\epsilon(0)$ is the dielectric permittivity at infinite and zero frequency, respectively. M is a transition matrix element between electron states, defined as

$$M(n', \pm q_z, n) = \int_{-\infty}^{\infty} f_{n'}(z)\exp(\pm i q_z z) f_n(z) dz, \quad (3)$$

where $f_{n'}$ and f_n are electron wave functions for final and initial envelope states in the z direction.

As a result of the momentum conservation expressed by the Kronecker delta in Eq. (2), a summation over the number of final states N' is equivalent to a summation over the number of states of phonon wave vectors $\bar{q}$. This number is obtained as

$$dN_{qx} \, dN_{qy} \, dN_{qz} = \frac{\Omega}{8\pi^3} q \, dq \, d\theta \, dq_z, \quad (4)$$

expressing the phonon vector $\bar{q}$ in cylindrical coordinates with θ measured with reference to the wave vector $\bar{k}$. One obtains upon substitution of Eq. (4) into Eq. (2) that

$$W_k = \frac{e^2 \omega_0}{8\pi^2 \epsilon_p} \int \int \int \frac{1}{Q^2} \delta_{\bar{k}\pm\bar{q}-\bar{k}',0} |M(n', \pm q_z, n)|^2$$

$$\cdot \left(g(\omega_0) + \frac{1}{2} \mp \frac{1}{2}\right) \delta(E' - E \mp \hbar\omega_0) q \, dq \, d\theta \, dq_z. \quad (5)$$

The energy conservation is expressed by the delta function. By integrating over the variable q, this delta function can be eliminated. Consider a transition between two QW envelope states of energies E_1, E_2 and $\Delta E = E_2 - E_1$, where E_1 is the ground-state energy. Introducing a new variable s according to

$$s = E' - E \mp \hbar\omega_0 = \frac{\hbar^2 k^2}{2m^*} - \Delta E - \frac{\hbar^2 k'^2}{2m^*} \mp \hbar\omega_0, \quad (6)$$

where

$$k'^2 = k^2 + q^2 \pm 2kq \cos\theta, \quad (7)$$

and thus

$$s = \frac{\hbar^2 q^2}{2m^*} \pm \frac{\hbar^2 kq}{m^*} \cos\theta - \Delta E \mp \hbar\omega_0, \quad (8)$$

and finally integrating over s, one obtains for the phonon emission process

$$W_k = \frac{e^2 \omega_0 m^*}{8\pi^2 \epsilon_p \hbar^2} \int_{-\infty}^{\infty} |M(q_z)|^2$$

$$\times \left(\int_0^{2\pi} \frac{1}{q(\theta)^2 + q_z^2} \frac{q(\theta)}{q(\theta) + k \cos \theta} d\theta \right) dq_z. \quad (9)$$

where

$$q(\theta) = -k \cos \theta + k \left(\cos^3 \theta + \frac{2m^*}{\hbar^2 k^2}(\Delta E - \hbar \omega_0) \right)^{1/2}. \quad (10)$$

The approximation $g(\omega_0) + 1 \approx 1$ has been used, which implies that spontaneous phonon emission dominates over stimulated. The innermost integral of Eq. (9) may be approximated by Taylor expansion in powers of k up to the third power, and finally integration. Since all terms containing odd powers of k cancel upon integration, one obtains

$$\int_0^{2\pi} \frac{1}{q(\theta)^2 + q_z^2} \cdot \frac{q(\theta)}{q(\theta) + k \cos \theta} d\theta$$

$$\approx \frac{2\pi}{q_0^2 + q_z^2} \left(1 + \frac{q^2 k^2}{2q_0^2(q_0^2 + q_z^2)} \right), \quad (11)$$

with $q_0 = \sqrt{2m^*(\Delta E - \hbar \omega_0)}/\hbar$.

Assuming equilibrium conditions, detailed balance prevails, and the number of electrons transferred from the ground state to an excited state (by phonon absorption) equals the number transferred from this excited state to the ground state (by phonon emission). The former quantity is of importance for determining the detector dark current, and can be assumed not to depend on whether the system is shifted out from equilibrium to a small extent. The latter quantity, however, is easier to calculate. It is a good approximation to assume that $k \approx 0$ or equivalently $k \ll q_0$. The major number of carriers is located within the energy interval $V_b, V_b + 2k_B T$ and at 80 K $2k_B T = 14$ meV. For detectors responding to radiation of wavelength ~ 9 μm, one obtains $(k/q_0)^2 < 0.005$. A simple estimation then gives for the second term of the expression in large parenthesis in Eq. (11) that

$$\frac{q_z^2 k^2}{2q_0^2(q_0^2 + q_z^2)} < \frac{1}{2} \left(\frac{k}{q_0} \right)^2 < 0.0025 \ll 1. \quad (12)$$

It can consequently be neglected; however, for very high electron kinetic energies it may become important. Such hot-electron effects are possible far from equilibrium conditions, e.g., at large bias voltages.

One obtains finally

$$W_{2 \to 1} = \frac{1}{\tau} \approx W_0 = \frac{e^2 \omega_0 m^*}{4\pi e_p \hbar^2} \int \frac{|M(q_z)|^2}{q_0^2 + q_z^2} dq_z, \quad (13)$$

where τ is the lifetime of electrons in the upper state.

We now consider a simple rectangular QW at zero bias conditions. We further assume that the dimensions of the QW have been chosen so that the upper state is quasibound, i.e., equal to the barrier energy V_b of the QW (see Fig. 2). The upper-state wave functions $f_{n'}(z)$ are normalized according to the assumption of a large (compared with the QW width) but finite one-dimensional box of width L, i.e., $f_{n'}(z) = (1/\sqrt{L})\hat{f}_{n'}(z)$, where $\hat{f}_{n'}$ has unity amplitude in the barrier layers. The bound ground-state wave function is normalized in the conventional manner. We further introduce
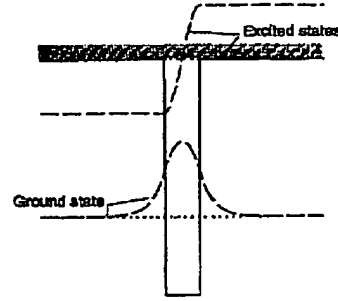

FIG. 2. Scheme of a simple quantum well of rectangular cross section, with the upper state wave functions quasibound. The ground-state and excited-state wave functions are shown (a.u.).

dimensionless variables according to $\zeta = \beta z$, $r = q_z/\beta$, $r_0 = q_0/\beta = \sqrt{1 - \hbar \omega_0/\Delta E_{co}}$, $F(\zeta) = f(\zeta/\beta)$, where β is a dimensionless parameter defined as $\beta^2 = 2m^* \Delta E_{co}/\hbar^2$. The cutoff energy E_{co} is defined as $E_{co} = V_b - E_1$. The parameter β is selected to put the Schrödinger equation into the normalized form

$$\frac{d^2 F(\zeta)}{d\zeta^2} + \frac{E - V(\zeta)}{\Delta E_{co}} F(\zeta) = 0, \quad (14)$$

with V the potential energy profile of the QW. In this way it is easier to compare similarly shaped QWs differing in their energy level spacings (i.e., different cutoff energy). One obtains from Eq. (13) for the lifetime

$$\tau = \frac{4 \hbar e_p \Delta E_{co} L}{e^2 E_{phon} I_1}, \quad (15)$$

where E_{phon} is the phonon energy (=36 meV for GaAs) and I_1 a dimensionless integral

$$I_1 = \int_{-\infty}^{\infty} \frac{|\langle \hat{F}_{n'}(\zeta)| \exp(-ir\zeta)|F_n(\zeta)\rangle|^2}{(r_0^2 + r^2)|\langle F_n(\zeta)\rangle|^2} dr. \quad (16)$$

I_1 depends slightly on r_0, but is close to 2 in the 8–12 μm range for a QW with a quasibound upper state, irrespective of the detailed shape of the QW. The dependence of I_1 on ΔE_{co} is presented in Fig. 3. The dependence of lifetime on ΔE_{co} is also included in this figure. It should be noted, however, that the unconfined phonon approximation does only hold for small ΔE_{co}, i.e., for detectors responding in the 8–12 μm range.

The majority of the upper-state electrons is located within the energy interval $V_b, V_b + 2k_B T$ ($2k_B T = 14$ meV at 80 K). It can be shown that for a QW of rectangular shape the upper-state wave function changes negligibly in this interval, and consequently I_1 (and therefore τ) is constant. One obtains from Eq. (15) that if $\Delta E = 140$ meV (corresponding to a cutoff wavelength of 9 μm) $E_{phon} = 36$ meV, and if $e_p = 63 e_0$ that $\tau = 1.1 \times 10^{-4} L$. $L = 500$ Å gives a lifetime of 5.5 ps.

The proportionality of lifetime to the box width L should be noted. Since the latter quantity is not well defined, one may instead introduce a QW capture velocity[11-13] $v_{QW} = L/\tau$,
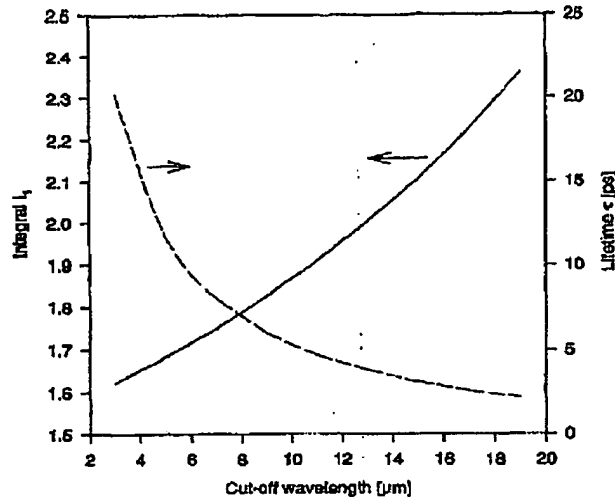
FIG. 3. Calculated values of the integral I_1 and the carrier lifetime τ vs the cutoff wavelength of the QWIP. A box width $L=500$ Å is assumed.

and obtains for the simple QW at zero bias $v_{QW}=9\times10^5$ cm/s. It should be noted that v_{QW} does not depend on L.

The 2D density of carriers originating from the E_2 subband is

$$n_{s2}=L\cdot2\left(\frac{2\pi m^* k_B T}{\hbar^2}\right)^{3/2}\exp\left(-\frac{V_b-E_F}{k_B T}\right),\qquad(17)$$

where E_F is the Fermi energy of the well equal to

$$E_F-E_1=\frac{n_{s1}\hbar^2}{4\pi m^*},\qquad(18)$$

with n_{s1} the 2D carrier density in the ground state. The carrier generation rate from a QW due to optical phonons may be obtained as

$$R_{phon}=\frac{n_{s2}}{\tau}.\qquad(19)$$

It could be noted that R_{phon} does not depend on L and is therefore a more basic parameter of the QWIP, in contrast to n_{s2} and τ.

III. DETECTOR DARK CURRENT AND CURRENT GAIN

The detector dark current in QW detectors is well described by thermal emission out from the QW, including tunneling through the barrier edge as well as direct emission above it. This directly implies that the current does not depend on the number of QWs in the structure, provided that contact injection effects do not have an influence and that all wells are identically biased. The current density from one single unbiased QW can be written, if quantum-mechanical reflection due to the barrier is neglected, as

$$J=e\frac{4\pi m^* k_B^2 T^2}{h^3}\exp\left(-\frac{V_b-E_F}{k_B T}\right).\qquad(20)$$

For an unbiased QW the current injected on either side of the QW is equal due to symmetry. For a biased QW this is not longer the case. In addition tunneling may be important in the latter case.

Th detector dark current gain g_{dark} can be obtain as the ratio of the detector dark current to the total generation current according to the expression,

$$J=eR_{phon}N_{QW}g_{dark},\qquad(21)$$

where N_{QW} is the number of QWs. One ends up with

$$g_{dark}N_{QW}=\frac{v_{cont}}{v_{QW}},\qquad(22)$$

where v_{cont} is the mean carrier velocity in the continuum,

$$v_{cont}=\left(\frac{k_B T}{2\pi m^*}\right)^{1/2}.\qquad(23)$$

One obtains for a detector with a cutoff wavelength of 9 μm consisting of 50 QWs, at 77 K, that $g_{dark}=0.12$. Experimental values are in the range 0.1–0.3.

Especially at BLIP conditions the gain g does not depend on temperature, and the electrons attain their energy distribution largely from the photon field combined with optical phonon relaxation between continuum states. In this case Eq. (22) can be used with $v_{cont}=v_{cont}(T_{hot})$, where T_{hot} is the temperature of the hot electrons. In the extreme case of $T_{hot}=300$ K one obtains $g=0.24$. Larger values of gain may result if v_{QW} is smaller, which is the case for detectors with fully extended upper states where the wave function overlap between ground state and excited states is smaller.

IV. THEORY OF PHOTOEXCITATION OF CARRIERS

Starting from basic quantum mechanics one can show that for a single QW the transition rate of photon-generated electrons from the ground state to the excited states, per unit QW area, becomes

$$R_{phot}=\frac{\tau_{opt}A_{coupler}}{4(f\#)^2}\cdot\frac{n_{s1}e^2h}{4nc\epsilon_0 m^*}$$
$$\times\int P(\Delta E)f_{osc}(\Delta E)\rho(\Delta E)d\Delta E,\qquad(24)$$

with the exitance (number of photons per unit photon energy and time striking unit area of the detector, and for 2π sr) given by

$$P(\Delta E)=\frac{2\pi\Delta E^2}{h^3c^2[\exp(\Delta E/k_B T_B)-1]}\approx\frac{2\pi\Delta E^2}{h^3c^2}\exp\left(\frac{-\Delta E}{k_B T_B}\right).$$
$$(25)$$

The oscillator strength

$$f_{osc}=2m^*\Delta E|\langle f_n|z|f_n\rangle|^2/\hbar^2.$$

The efficiency of the coupler used to couple radiation into the detector $A_{coupler}=\frac{1}{4}\sin^2\varphi$ for a polished edge detector, φ being the angle of incidence within the GaAs with respect to the QW plane. τ_{opt} is the optical transmission, and $f\#$ the optics f number. One obtains $A_{coupler}=0.25$ for a 45° polished edge detector. For a detector with a crossed grating and dielectric mirror one obtains (Refs. 4 and 5) $A_{coupler}\approx1$. It is
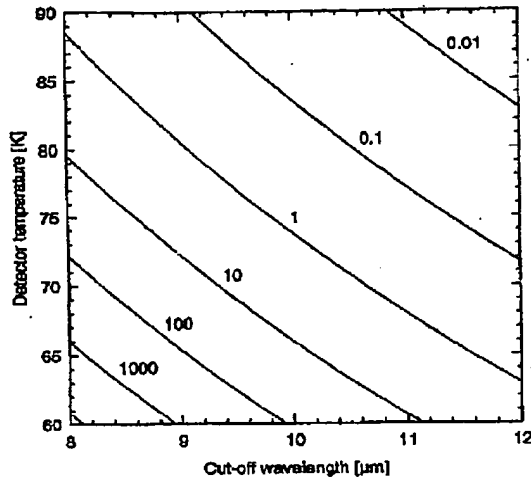
FIG. 4. Contour plot displaying calculated values of the ratio of photoexcited to thermal generation rates vs cutoff wavelength and detector operating temperature. Assumptions: detector with two-dimensional grating and optical cavity, optics $f\# =1$ and transmission 100%, background temperature 300 K.

assumed that the detector operates in the low absorption regime characterized in that R_{phot} is proportional to n_{s1}. Furthermore, the QW structure is assumed to be appreciably sensitive to photons close to the energy ΔE_{∞} only, as a result of the large value of the density of states close to the barrier band edge. T_B is the temperature of a blackbody photon source, and $\rho(\Delta E)$ the one-dimensional density of states,

$$\rho(E_2)=\frac{1}{h}\left(\frac{2m^*}{(E_2-V_b)}\right)^{1/2}. \tag{26}$$

Assuming that $|\langle f_{n'}|z|f_n\rangle|^2$ does not depend considerably on the energy E_2 it can be moved outside the integral sign. Simplifying one obtains

$$R_{phot}=\frac{\tau_{opt}A_{coupler}}{(f\#)^2}\frac{n_{s1}e^2 I_2(k_BT_B)^3\sqrt{\pi k_BT_B}}{128\,\epsilon_0 c^3 nh^2\Delta E_{\infty}^{3/2}m^*}\,G$$

$$\times\left(\frac{V_b-E_1}{k_BT_B}\right)\exp\left(-\frac{V_b-E_1}{k_BT_B}\right), \tag{27}$$

where

$$G(s)=8s^3+12s^2+18s+15. \tag{28}$$

I_2 is a dimensionless integral,

$$I_2=\frac{|\langle\hat{F}_{n'}(\zeta)|\zeta|F_n(\zeta)\rangle|^2}{|\langle F_n(\zeta)\rangle|^2}. \tag{29}$$

For a simple QW of rectangular shape and with the upper state quasibound one has $I_2=5.25$.

V. CALCULATION OF BLIP TEMPERATURE

From Eqs. (19) and (27) the ratio of the generation rates of photoexcited to phonon-excited carriers R_{phot}/R_{phon} is calculated and presented in Fig. 4 in a contour plot versus cutoff wavelength and detector operating temperatures. An optics
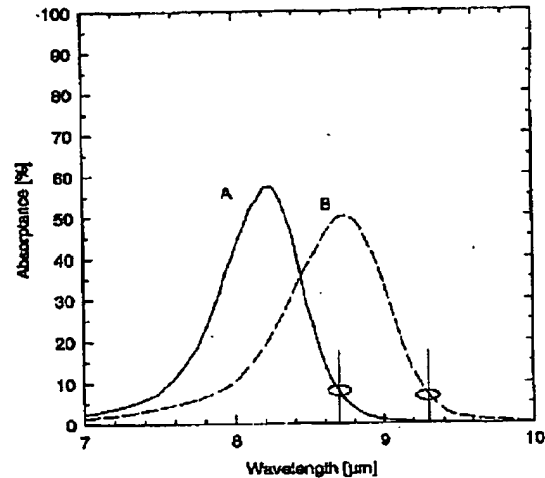
FIG. 5. The measured absorptance vs wavelength for the detectors A and B which were experimentally investigated. The cutoff wavelengths are indicated by solid vertical lines.

transmission of 100%, $f\# =1$, the optical coupling factor $A_{coupler}=1$, the background temperature $T_B=300$ K, and a sheet concentration of 2×10^{11} cm^{-2} are assumed. The latter value corresponding to $E_F=2k_BT$ optimizes the signal-to-noise ratio of the detector. The BLIP temperature is conveniently calculated using either the $R_{phot}/R_{phon}=1/1$, or$=10/1$ criterion. One obtains $T_{BLIP}=81$ K and 73 K, respectively for a 9 μm cutoff detector. In general it is found that for such a detector the thermal generation current increases by a factor of 2 when the temperature increases by 2.5 K. Increasing the $f\#$ from 1 to 2 decreases the BLIP temperature by 5 K, and increasing the cutoff wavelength by 1.0 μm leads to a 7 K decrease of T_{BLIP}.

VI. COMPARISON OF THEORY WITH EXPERIMENTAL DATA

In order to compare the theoretical findings with experimental data, two types of QWIP detector structures (here denoted A and B) corresponding to the cutoff wavelengths 8.7 and 9.3 μm, respectively, were fabricated by low-pressure metalorganic vapor-phase epitaxy (MOVPE). The structure consisted of 50 QWs of: (QW width (Å), barrier width (Å), Al content x)=(49, 340, 29.8) for structure A, and (52, 348, 29.0) for B. The sheet carrier concentration was 2×10^{11} cm^{-2}. Detector elements of size 150×150 μm^2 were processed by mesa etching, and finally a two-dimensional grating was fabricated by dry etching into the top contact. The grating constants were 2.7 and 2.8 μm for A and B, respectively. Figure 5 displays the absorptance versus wavelength for the two types of detectors.

The ratio R_{phot}/R_{phon} of the detectors A and B at 77 K was measured at a bias voltage of 2 V, with $\tau_{opt}=70$%, $f\#=2$, with the results 0.84 and 0.42, respectively. These values should be compared with the theoretical values 0.88 (A) and 0.27 (B) assuming $A_{coupler}=1$. The agreement is evidently fairly good. In fact, the quantities accessible for direct mea-

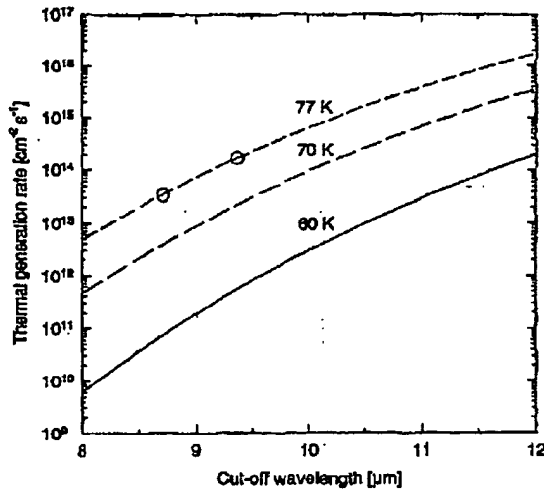<div align="right">J. Y. Andersson</div>

FIG. 6. Theoretically obtained thermal generation current vs cutoff wavelength for three different detector temperatures. Assumptions: detector with two-dimensional grating and optical cavity, optics $f\# = 2$ and transmission 70%, background temperature 300 K. Experimental results for the detectors A and B obtained at 77 K and otherwise similar conditions are indicated by circles.

surement are the detector photocurrent and thermal current, as well as their ratio. However, if the detector gain is assumed to be the same for photo- and thermal current, the ratio of the detector currents can be set equal to the corresponding generation rates. In view of Sec. III above this is a reasonable assumption.[14]

The thermal generation rate R_{phon} of a detector can be extracted from the dark current and the generation-recombination (GR) noise according to

$$I_{dark} = eR_{phon}A_d N_{QW} g_{dark},$$ (30)

and

$$i_{GR}^2 = 4eI_{dark} g_{dark} \Delta f,$$ (31)

where I_{dark} is the detector dark current, i_{GR} the GR noise current, A_d the detector area, and Δf the noise bandwidth. R_{phon} is obtained from Eqs. (30) and (31) by the elimination of g_{dark},

$$R_{phon} = \frac{\Delta f}{N_{QW}A_a} \frac{4 I_{dark}^2}{i_{GR}^2}.$$ (32)

Experimental values of R_{phon} obtained at 77 K and a bias voltage=2 V are presented for detectors A and B in Fig. 6, together with theoretical curves. The bias voltage was selected to ascertain that the escape probability of carriers in the QW was nearly unity. The values of R_{phon} were 3.7×10^{13} and 1.5×10^{14} cm^{-2} s^{-1} for detectors A and B, respectively. According to Fig. 6 the agreement between theory and experiment is excellent. It should be noted that the expression Eq. (18) does not contain any extra fitting parameters except for the cutoff wavelength. It turned out that the best fit to experimental data was obtained for a cutoff wavelength corresponding to where the response is 10% of the maximum value (see Fig. 5).

The theory presented above assumes that the major contribution to the generation rate stems from single phonon processes. It may be argued that in certain cases multiphonon processes may become important. If such processes contribute, the value of generation rate will be even larger than if only single phonon processes is taken into consideration. In view of the fact that theoretical and experimental results agree, the single phonon approximation is valid, at least under the conditions prevailing during the experiment.

VII. SUMMARY AND CONCLUSIONS

The most prominent mechanism of dark current in infrared detectors based on intersubband transitions in quantum wells is due to interaction of electrons with longitudinal optical (LO) phonons. The interaction is of the Fröhlich type where lattice displacements due to phonons create strong electric fields which in turn interact with the electrons and cause transitions between electron states.

Starting from basic quantum mechanics, expressions are derived for the carrier lifetime, as well as for the generation rates of photoexcited and thermally excited electrons (number of excited electrons from the ground state to the extended states of the QW per unit time and QW area). The lifetime τ for a detector with quasibound upper states can be written

$$\tau = (4h e_p \Delta E_{co} L)/(e^2 E_{phon} I_1),$$

where ΔE_{co} is the detector cutoff energy, E_{phon} the optical phonon energy (=36 meV for GaAs), h Planck's constant, e the electron charge, I_1 a constant close to 2, and L a characteristic length along the growth direction of the QW approximately equal to the period length of the QW. $1/e_p = 1/e(\infty) - 1/e(0)$, where $e(\infty)$ and $e(0)$ is the dielectric permittivity at infinite and zero frequency, respectively. The thermal generation rate of electrons from a QW R_{phon} can be written $R_{phon} = n_{s2}/\tau$, where n_{s2} is the two-dimensional carrier concentration in the continuum. In contrast to τ and n_{s2}, R_{phon} does not contain the somewhat arbitrarily defined length L, and is therefore a more fundamental quantity of the QW.

The temperature of background radiation limitation (BLIP) can be deduced from the temperatures T_{BLIP} where the ratio R_{phot}/R_{phon} takes suitable values such as e.g., 10/1 or 1/1. One obtains for these different criteria $T_{BLIP} = 81$ and 73 K respectively, for a 9 μm cutoff detector with a two-dimensional grating and optical cavity. The f number is 1 and the optics transmission is 100%. In general it is found that for such a detector the thermal generation current increases by a factor of 2 when the temperature increases by 2.5 K. Increasing the $f\#$ from 1 to 2 decreases the BLIP temperature by 5 K, and increasing the cutoff wavelength by 1.0 μm leads to a 7 K decrease of T_{BLIP}.

Calculated values of thermal generation currents and the ratio of photocurrent to thermal current are found to accord well with experimental data.

ACKNOWLEDGMENTS

[1] See, for example, *Quantum Well Intersubband Transition Physics and Devices*, edited by H. C. Liu, B. F. Levine, and J. Y. Andersson, NATO ASI Series Vol. B 270 (Kluwer, Dordrecht, 1994).

[2] B. F. Levine, J. Appl. Phys. 74, R1 (1993).

[3] M. A. Kinch and A. Yariv, Appl. Phys. Lett. 55, 2093 (1989).

[4] J. Y. Andersson and L. Lundqvist, J. Appl. Phys. 71, 3600 (1992).

[5] L. Lundqvist, J. Y. Andersson, Z. F. Paska, J. Borglind, and D. Haga, Appl. Phys. Lett. 63, 3361 (1993).

[6] K. K. Choi, C. Y. Lee, M. Z. Tidrow, W. H. Chang, and S. D. Gunapala, Appl. Phys. Lett. 65, 1703 (1994).

[7] R. A. Riddoch and B. K. Ridley, J. Phys. C 16, 6971 (1983).

[8] O. Madelung, *Introduction to Solid State Theory*, Springer Series in Solid-State Sciences Vol. 2 (Springer, Berlin, 1981), p. 175.

[9] B. K. Ridley, Phys. Rev. B 39, 5282 (1989).

[10] B. K. Ridley, in Ref. 1, p. 443.

[11] E. Rosencher, F. Luc, L. Thibaudeau, B. Vinter, and P. Bois, in Ref. 1, p. 97.

[12] E. Rosencher, F. Luc, P. Bois, J. Nagle, and Y. Cordier, Appl. Phys. Lett. 63, 3312 (1993).

[13] E. Rosencher, B. Vinter, F. Luc, L. Thibaudeau, P. Bois, and J. Nagle, IEEE Trans. Quantum Electron. QE-30, 2875 (1994).

[14] H. C. Liu, Appl. Phys. Lett. 60, 1507 (1992).

EXHIBIT C

For

Declaration Under 37 CFR 1.132

US Application No. 09/836,464
Reply to Final Official Action mailed on April 16, 2004

Nois gain and p rating temp ratur of quantum well infrared photod t ctors

H. C. Liu

Institute for Microstructural Sciences, National Research Council, Ottawa, Ontario K1A 0R6, Canada

The difference between the noise gain associated with dark current and the photoconductive gain in quantum well infrared photodetectors is discussed in light of recent experiments. The theoretical model is based on a single key parameter: the electron trapping probability. An empirical expression for the trapping probability or, alternatively, the electron escape probability is proposed. Using the dark current, the gain, the trapping probability expressions, and the device operating temperature for achieving background limited infrared performance is discussed.

One of the success stories in applications of quantum well structures is the use of intersubband transitions between effective mass envelope states for long wavelength infrared detection. Levine and coworkers have undoubtedly made the most contributions to this field.[1] The recent book[2] provides a relatively complete and up-to-date collection of papers. Various physical aspects of quantum well infrared photodetectors (QWIPs) are still under active and intense investigation.[3–7] Here, we discuss the physical difference between the noise gain associated with dark current and the photoconductive gain, in light of recent experiments.[6] We employ the dark current model given in Refs. 1 and 8 and the model for the photoconductive gain in Ref. 5. We propose an empirical expression for the key parameter: the carrier trapping probability. We then discuss the detector operating temperature for background limited infrared performance (BLIP). The purpose of the letter is to present a coherent model for evaluating QWIP performance and to provide realistic estimates for the detector operating temperature and the detectivity.

We first list the expression for the photoconductive gain:

$$g_{photo}=(1-p)/Np, \qquad (1)$$

where N is the number of wells in the QWIP, and p is the trapping probability for an electron (with energy larger than the barrier height) traversing a well. The derivation of Eq. (1) and the mechanism of the photoconductive gain have been discussed in detail in Ref. 5. Reference 5 also explains the somewhat counter-intuitive result[9–11] that the detector current responsivity is *independent* of the number of wells. This, however, does not mean that the detector performance is independent of N as shown later.

For practical purposes, the dark current noise and the background photon noise often limit the detector ultimate performance in photoconductive QWIPs. Here we concentrate on these two mechanisms. In deriving noise expressions, the author has found the simple physical picture given by Rose (see pp. 97–99 of Ref. 12) to be extremely convenient. One identifies the source α of the noise and the magnification factor F in observation. Then the noise (square-average) is

$$I_n^2=2F^2\alpha\Delta f, \qquad (2)$$

where Δf is the measurement bandwidth.

Because the escaping and the trapping processes control the dark current,[8] the noise associated with dark current is generation-recombination (g-r) in nature. The noise current therefore should be given by the standard expression for g-r noise[12]

$$i_{n,dark}^2=4eg_{noise}I_{dark}\Delta f, \qquad (3)$$

where I_{dark} is the device dark current and g_{noise} is the noise gain associated with dark current. In a conventional photoconductor, the noise gain equals the photoconductive gain $g_{noise}=g_{photo}$ (at least as a very good approximation for all practical purposes). We show in the following that the two gains are, strictly speaking, not identical, and direct evidence for QWIPs has been reported in Ref. 6. The best dark current model thus far is that proposed by Levine *et al.*[1] A detailed derivation and discussions of the physical mechanism have been carried out in Ref. 8, in which the current "emitted" from a well (i_{em}) was calculated and then the dark current was found by multiplying by $1/p$ (which takes into account trapping and injection). The dark current is written as[8]

$$I_{dark}=i_{em}/p=(Ni_{em})/(Np), \qquad (4)$$

where (Ni_{em}) is the total emission current from all N wells. Equivalently, one can express the dark current in an alternate form: $I_{dark}=i_{trap}/p$, where i_{trap} is the trapping current per well and $i_{trap}=i_{em}$ in steady state. The g-r (emission and trapping here) noise therefore consists of contributions from two separate sources: fluctuations in i_{em} and in i_{trap}, and so $\alpha=(Ni_{em}+Ni_{trap})/e$. The magnification F factor is $e/(Np)$ according to Eq. (4). Substitution into Eq. (2) gives

$$i_{n,dark}^2=2e(1/Np)^2(Ni_{em}+Ni_{trap})\Delta f$$
$$=4e(1/Np)I_{dark}\Delta f. \qquad (5)$$

Comparison with Eq. (3) yields the noise gain expression $g_{noise}=1/(Np)$. We can see immediately that the noise gain g_{noise} is different from the photoconductive gain $g_{photo}=(1-p)/(Np)$.[5] Since p is the capture or trapping probability, $1-p$ therefore represents the probability of an electron escaping from a well. Note that because we neglect inter-well tunneling, the capture probability for transport electrons associated with the dark current and that for photoelectrons are the same, i.e., the dark current and the

photocurrent follow th same path with the only difference being the emissi n mechanism from the wells. Levine *et al.*[6] reported measurements of this escape probability $p_e = 1 - p$ versus electric field. Their measured p_e was less than one at low bias voltages and approached one as the bias voltage was increased.[6] Our noise model presented here is equivalent to that of Janousek *et al.*[13] in the same physical regime.

The detector noise associated with the background radiation is caused by fluctuations in the number of background photons absorbed by a detector (Φ_B). For a photoconductor, the noise current due to this mechanism is given by

$$i_{n,B}^2 = 4e^2 g_{photo}^2 \Phi_B \Delta f. \tag{6}$$

Unlike the dark current noise $I_{n,dark}$ which is proportional to $g_{noise}^{1/2}$, the background noise $I_{n,B}$ is directly proportional to the photoconductive gain: $i_{n,B} \propto g_{photo}$. This relies on the fact that I_{dark} is independent of the gain as discussed in detail in Ref. 8.

The background limited infrared performance (BLIP) is defined as the regime where the dominant noise source is due to the background photon fluctuations. BLIP can be achieved at higher detector operating temperatures for devices with larger gain values. The BLIP temperature (T_{BLIP}) is defined as the temperature at which $I_{n,dark} = I_{n,B}$. Equating (5) and (6), we obtain an equation t solve for T_{BLIP}:

$$e\frac{(1-p)^2}{Np} \Phi_B = I_{dark}\Big|_{T=T_{BLIP}}, \tag{7}$$

where we have used $g_{photo} = (1-p)/Np$ and $g_{noise} = 1/Np$. In the weak absorption limit, Eq. (7) is independent of N because $\Phi_B \propto N$ and because I_{dark} versus electric field is independent of N.[8] To improve T_{BLIP} one needs to maximize the quantity on the left-hand side of Eq. (7). In designing a QWIP, N must be large enough to obtain a high absorption quantum efficiency, but increasing N indefinitely will result in a lower T_{BLIP}. Minimizing p would result in an improvement on T_{BLIP}. Current GaAs-AlGaAs QWIPs have values of p in the range of 0.02–0.1 at high electric fields.[3]

For completeness, we give the expression for the most important detector figure of merit. The detectivity (D^*) is given by

$$D^* = \frac{e g_{photo}\eta/h\nu}{\sqrt{i_{n,dark}^2/\Delta f + i_{n,B}^2/\Delta f}}$$

$$= \frac{g_{photo}\eta/h\nu}{\sqrt{4g_{noise}J_{dark}/e + 4g_{photo}^2\Phi_B/A}} \tag{8}$$

where η is the absorption quantum efficiency, $h\nu$ is the photon energy, J_{dark} is the dark current density, and A is the device area. Higher T_{BLIP} and D^* can be achieved with higher gain values. At high enough electric field (e.g., > 10 kV/cm), the two gains are approximately equal: $g_{noise} \approx g_{photo}$ because $p \ll 1$. Once the gain value is large enough so that the second term in the denominator of Eq. (8)

dominates, the detectivity D^* is independent of both dark current and the gain.

We now propose an empirical expression for the escape probability p_e versus electric field ($\mathscr{F}$). Physically, the trapping process is controlled by events that scatter electrons from a barrier transport state onto the confined two-dimensional subband. Therefore, one expects the functional dependence of the trapping probability on the field to be similar to that of drift mobility, and we write

$$p_e = 1 - p = p_0 \frac{(\mathscr{F} + \mathscr{F}_0)/\mathscr{F}_{sat}}{\sqrt{1 + [(\mathscr{F} + \mathscr{F}_0)/\mathscr{F}_{sat}]^2}}, \tag{9}$$

where the fitting constants are p_0, $\mathscr{F}_0$, and $\mathscr{F}_{sat}$. When $\mathscr{F}_0 > 0$ and $\mathscr{F} \to 0$, a nonvanishing escape probability is obtained; this corresponds to the case where the quantum well confines only one bound state, i.e., a bound-to-continuum transition QWIP. The asymptotic high field value of p_e is p_0 which should be nearly 100%. Fitting to the experimental data of Levine *et al.*[6] for the bound-to-continuum case, we found $p_0 = 1$, $\mathscr{F}_0 = 2.2$ kV/cm, and $\mathscr{F}_{sat} = 5$ kV/cm. The fitted p_e vs $\mathscr{F}$ curve is shown in Fig. 1(a). The case of $\mathscr{F}_0 < 0$ corresponds to a bound-to-bound transition QWIP (i.e., two bound states exist in the well), and one must take $p_e = 0$ for $\mathscr{F} < -\mathscr{F}_0$ instead of Eq. (9). Physically, a finite field is needed to obtain $p_e > 0$ for the bound-to-bound case. The optimum detector design[10,14] corresponds to the upper state nearly degenerate with the barrier height for which $\mathscr{F}_0 \approx 0$. We stress that Eq. (9) should be viewed as a pure empirical equation used for curve fitting. Levine *et al.*[6] used an exponential function which also produced good fit to the experimental data of p_e vs $\mathscr{F}$.

Using our model some calculated results are shown in Figs. 1 and 2. The dashed curve in Fig. 1(a) is the escape probability vs electric field used in the modeling, with parameters $p_0 = 1$, $\mathscr{F}_0 = 0$, and $\mathscr{F}_{sat} = 10$ kV/cm. These parameters are appropriate for our detectors with the upper state nearly in resonance with the top of the barrier.[8,10,11] The dark current density for an 8.7 μm peak response detector at different temperatures is shown in Fig. 1(b). The dashed curve is the left-hand-side of Eq. (7), and therefore the intersecting points correspond to T_{BLIP}. Figure 1(c) shows the calculated peak detection wavelength D^* including dark current and background noise contributions. The horizontal line is for the BLIP D^*, i.e., D^* calculated without the dark current noise. The detector spectral bandwidth is 1.8 μm, and this detector therefore covers the 7.8–9.6 μm range. The parameters used in these calculations are listed in Table I, and the dark current model is that given in Refs. 1 and 8. In calculating Φ_B, we have used a 90° (full cone angle) field of view (FOV) for a 300 K blackbody background, and a Lorentzian lineshape for the absorption versus photon energy with a full width at the half maximum corresponding to 20% of the photon energy at the peak absorption. The peak absorption is taken to be 100%, which is achievable with 50 wells and a grating-waveguide light coupling scheme.[3] Figure 2 shows the calculated T_{BLIP} versus applied field for three detectors corresponding to an 8.7 μm peak response detector with half
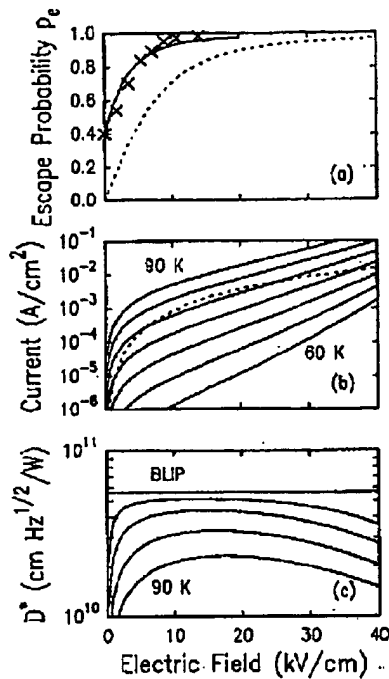
FIG. 1. (a) Electron trapping probability vs electric field. The crosses represent measured results, and the solid curve is the fit to these data using our empirical expression. A model (dashed) curve for the detector used in parts (b) and (c) is also shown. (b) Calculated dark current density vs electric field for an 8.7 μm detector at different temperatures of 60, 65, 70, 75, 80, 85, and 90 K. The intersecting points of the dark current curves with the dashed curve determine the background limited infrared performance (BLIP) temperatures. The dashed curve is plotted for evaluating the BLIP temperature. (c) Calculated detectivity (D^*) vs electric field for the 8.7 μm detector at different temperatures of 90, 85, 80, and 75 K. The horizontal line is the BLIP D^*.
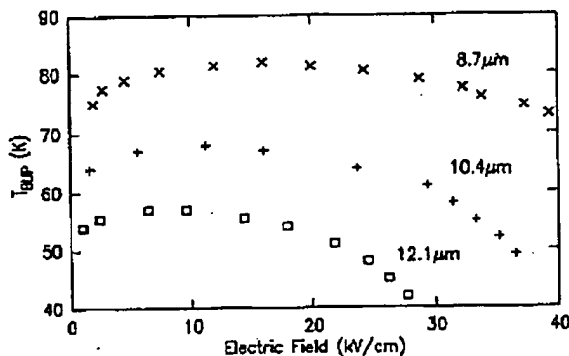

FIG. 2. Detector operating temperature for background limited infrared performance. The three curves correspond to an 8.7 μm peak response detector with half points at 7.8 and 9.6 μm (crosses), a 10.4 μm peaked detector covering 9.4–11.4 μm (pluses), and a 12.1 μm peaked detector covering 10.9–13.3 μm (squares).

TABLE I. Parameters used in calculations. The Fermi energy was 18 meV corresponding to a $5\times10^{11}/cm^2$ two-dimensional doping density in the wells, the mobility was 1000 cm^2 V^{-1} s^{-1}, the saturated velocity was 10^7 cm s^{-1}, and detectors all have 50 wells and 50.0 nm wide barriers. The symbols V_b, E_0, m_b^*, and L_w are for the barrier height, the ground state eigenenergy, the barrier effective mass, and the well width, respectively.

Sample	V_b (eV)	E_0 (meV)	m_b^*	L_w (nm)
8.7 μm	0.211	59.4	0.089	5.9
10.4 μm	0.178	49.4	0.085	6.5
12.1 μm	0.154	42.3	0.083	7.1

points 7.8 and 9.6 μm, a 10.4 μm peaked detector covering 9.4–11.4 μm, and a 12.1 μm peaked detector covering 10.9–13.3 μm. Our estimated T_{BLIP} values are higher than those of Kinch and Yariv,[15] who used device parameters appropriate for lower absorption quantum efficiencies. To investigate the effect of FOV angle on T_{BLIP} and D^*, we have made additional calculations for 30° and 60° FOV angles. Because of fewer background photons on the detector, a smaller FOV angle results in a higher BLIP D^* once the BLIP condition is reached, however, a lower temperature is required to reach BLIP. For the 10.4 μm peaked detector and for 30°, 60°, and 90° FOV, the BLIP D^* is 1.53×10^{11}, 7.91×10^{10}, and 5.60×10^{10} cm Hz$^{1/2}$/W, and T_{BLIP} at the optimum electric field of about 10 kV/cm is 61, 66, and 68 K, respectively. The recent work of Andersson and Lundqvist[16] indicates that the quantum efficiency remains constant at least up to 30° FOV.

I thank Dr. A. G. Steele of NRC and Dr. B. F. Levine of AT&T Bell Laboratories for many discussions. This work was supported in part by DND DREV.

[1] B. F. Levine, C. G. Bethea, G. Hasnain, V. O. Shen, E. Pelve, R. R. Abbott, and S. J. Hsieh, Appl. Phys. Lett. 56, 851 (1990).
[2] Intersubband Transitions in Quantum Wells, edited by B. Rosencher, B. Vinter, and B. F. Levine (Plenum, New York, 1992).
[3] J. Y. Andersson and L. Lundqvist, Appl. Phys. Lett. 59, 857 (1991).
[4] K. K. Choi, L. Fotiadis, M. Taysing-Lara, W. Chang, and G. J. Iafrate, Appl. Phys. Lett. 59, 3303 (1991).
[5] H. C. Liu, Appl. Phys. Lett. 60, 1507 (1992).
[6] B. F. Levine, A. Zussman, M. T. Asom, J. M. Kuo, and W. S. Hobson, J. Appl. Phys. 72, 4429 (1992).
[7] E. Rosencher, F. Luc, Ph. Bois, and S. Delaitre, Appl. Phys. Lett. 61, 468 (1992).
[8] H. C. Liu, A. G. Steele, M. Buchanan, and Z. R. Wasilewski (unpublished).
[9] G. Hasnain, B. F. Levine, S. Gunapala, and N. Chand, Appl. Phys. Lett. 57, 608 (1990).
[10] H. C. Liu, A. G. Steele, M. Buchanan, and Z. R. Wasilewski, Intersubband Transitions in Quantum Wells, edited by E. Rosencher, B. Vinter, and B. F. Levine (Plenum, New York, 1992), pp. 57–63.
[11] A. G. Steele, H. C. Liu, M. Buchanan, and Z. R. Wasilewski, J. Appl. Phys. 73, 1062 (1992).
[12] A. Rose, Concepts in Photoconductivity and Allied Problems (Interscience, Wiley, New York, 1963).
[13] B. K. Janousek, M. K. Daugherty, W. L. Bloss, M. L. Rosenbluth, M. J. O'Loughlin, H. Kanter, F. J. De Luccia, and L. E. Perry, J. Appl. Phys. 67, 7608 (1990); W. A. Beck 69, 4129 (1991).
[14] A. G. Steele, H. C. Liu, M. Buchanan, and Z. R. Wasilewski, Appl. Phys. Lett. 59, 3625 (1991).
[15] M. A. Kinch and A. Yariv, Appl. Phys. Lett. 55, 2093 (1989); see also B. F. Levine 56, 2354 (1990).
[16] J. Y. Andersson and L. Lundqvist, J. Appl. Phys. 71, 3600 (1992).

EXHIBIT D

For

Declaration Under 37 CFR 1.132

US Application No. 09/836,464
Reply to Final Official Action mailed on April 16, 2004

Achievements and Results

QWIP Technology

QWIPs for high-performance thermal imaging

QWIP: a Mature Technology for High-Performance IR Detectors

Quantum well infrared photodetectors (QWIPs) have by now become the new technology for high-performance staring focal plane array (FPA) cameras. In the 8–12 μm spectral window, QWIPs achieve high detectivity and low noise, resulting in excellent noise-equivalent temperature difference (NETD), and high dynamic range. The maturity of the GaAs-technology makes QWIPs particularly suited for large FPAs with high spatial resolution. In addition, excellent lateral homogeneity is achieved, thus giving rise to a small fixed-pattern noise. QWIPs have an extremely small 1/f noise compared to inter-band detectors (like HgCdTe or InSb), which is particularly useful if long integration time τ_{int} or image accumulation is required. For these reasons, QWIP is the detector technology of choice for many applications where somewhat smaller quantum efficiencies and slightly lower operation temperatures, compared to inter-band devices, are tolerable.

In collaboration with our industrial partner AEG Infrarot-Module (AIM),

Heilbronn, we have realized a variety of QWIP FPAs with pixel numbers from 256x256 to 640x512. The arrays are based on different QWIP layer structures according to the desired system parameters of the respective cameras. System properties of our QWIP-based camera products are summarized in Tab. 1.

Detectors for the 8–12 μm Regime

In our initial demonstrators we used a »standard« photoconductive QWIP structure (denoted as PC in Tab. 1), resulting in an excellent NETD below 10 mK in a 256x256 FPA (< 20 mK in a 640x512 FPA). The best NETD is currently achieved by the »Low-Noise« QWIP, a photovoltaic (PV) QWIP design. NETDs as low as 5 mK are achievable with this proprietary QWIP technology that has been described in more detail in our previous annual report.

The new millenium has started with novel application-specific QWIP developments and additional array formats. An important achievement was

Product	Image-format	Pitch (μm)	λ (μm)	T_{Det} (K)	τ_{int} (ms)	NETD (mK)
256x256 PC	256x256	40	8 – 9.5	60 – 65	16	10
640x512 PC	640x480 512x512	24	8 – 9.5	60 – 65	16	20
256x256 PV	256x256	40	8 – 9.5	60 – 65	20 40	7 5
640x512 PV	640x480 512x512	24	8 – 9.5	60 – 65	30	10
384x288 PV	384x288	24	8 – 9.5	60 – 65	30	10*
640x512 PC-FAST	640x480 512x512	24	8 – 9.5	60 – 65	4	20*
384x288 PC-FAST	384x288	24	8 – 9.5	60 – 65	4	20*
640x512 PC-MWIR	640x480 512x512	24	4.3 – 5	80 – 90	20	14

Tab. 1: System properties of camera products based on our QWIP FPAs. NETD-values assume f/2-optics, stars (*) indicate target values of cameras that are currently being assembled at AIM.

the successful demonstration of our first 640x512 Low-Noise QWIP FPA. Integrated in a camera system, the measured NETD of the FPA is as low as 10 mK, which represents a similar improvement as in the previous 256x256 FPA.

A second goal was to provide a photoconductive QWIP for short exposure times (denoted PC-FAST) allowing comparable temperature resolution at 4 ms instead of 16 ms integration time. For this purpose, we have realized a QWIP structure with an increased carrier density in the active region, which ensures higher quantum efficiency at the penalty of higher dark current. PC-FAST QWIP FPAs with 640x512 pixels have been fabricated. Camera integration is currently being performed at AIM.

Third, we have introduced a new 384x288 FPA. The 24 μm pitch being identical to the one used in the 640x512 array, the new FPA has an area of only 0.8 cm². Both Low-Noise and PC-FAST QWIP FPAs with this format have been processed and delivered to AIM.

QWIP FPA for the 3-5 μm Regime

There is a strong need for high-quality detector arrays operating in the 3-5 μm mid-wavelength infrared (MWIR) atmospheric window. In the MWIR, photon fluxes are 1-2 orders of magnitude lower than in the long-wavelength regime. We developed a MWIR-QWIP operating at 4.4-5.0 μm. Compared to the previous detectors for the LWIR, the new detector has a strongly increased carrier concentration (2×10^{12} cm^{-2} per quantum well) to obtain high quantum efficiency at tolerable dark current. The detector is based on coherently strained 2.6 nm $In_{0.3}Ga_{0.7}As$ wells and 45 nm $Al_{0.32}Ga_{0.68}As$ barriers.

Several process developments were necessary to fabricate our first MWIR-QWIP FPA. Reflective two-dimensional gratings with a period of 1.65 μm have been realized by optical contact lithography and reactive ion-beam (RIE) etching. FPA-mesas with center contacts surrounded by gratings are shown in Fig. 1.

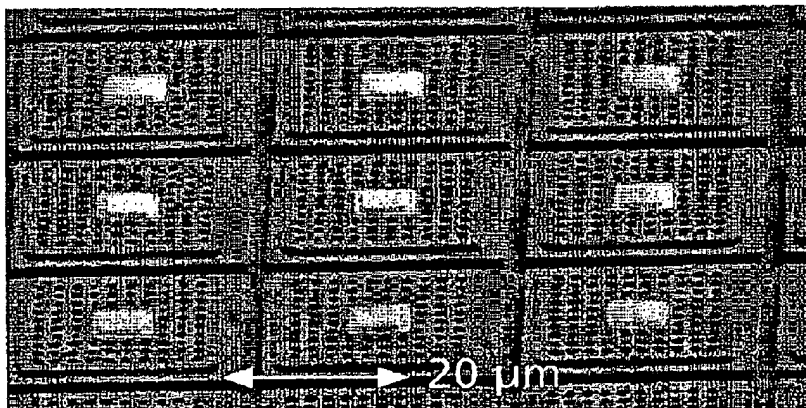QWIP-flexible technology for infrared applications

Fig. 1: Section of a MWIR-QWIP FPA optimized to a 4.4-5.0 μm spectral range (scanning electron microscopy image).

Ach'evements and Results

Due to the In-containing active region, chemically-assisted ion beam etching rather than RIE was applied to define mesas. 640x512 MWIR-QWIP FPAs with a peak quantum efficiency of more than 10% have been successfully fabricated. System integration has been performed by AIM. At a detector temperature of 88 K, the system has an excellent NETD of 14 mK at 20 ms integration time.

Image Signatures in the MWIR and LWIR Spectral Regimes

Both emissive and reflective signatures are prominent in the MWIR spectral regime, while images in the LWIR are strongly dominated by emissive signatures. In order to illustrate this difference, we have included MWIR and LWIR scenes in Figs. 2 and 3, respectively.

Reflection of sunlight from cars, in particular from their windows, gives rise to strong features in the MWIR. Emissive signatures, e. g., from a warm engine and from a person, are simultaneously visible.

In contrast, the image observed in the LWIR spectral regime is largely dominated by emissive effects, while reflective features are strongly suppressed.

Depending on the application, different signatures are of interest in infrared imaging. New system applications for QWIP-based infrared cameras will emerge since different atmospheric windows can now be exploited.

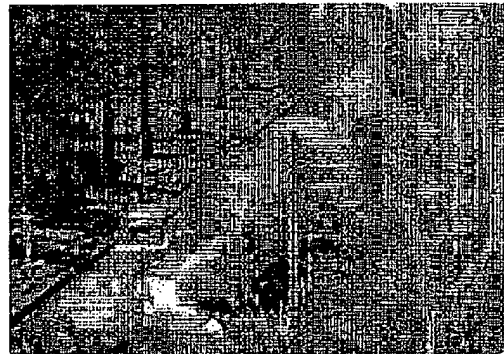Fig. 2: IR-scene taken by a QWIP-camera operating in the MWIR spectral regime.

Fig. 3: IR-scene taken by a QWIP-camera operating in the LWIR.

Contact:
Dr. H. Schneider
Phone: +49 (0)761 5159-359
E-Mail: hschneider laf.fhg.de

EXHIBIT E

For

Declaration Under 37 CFR 1.132

US Application No. 09/836,464
Reply to Final Official Action mailed on April 16, 2004

Acreo

QWIP Arrays

**Infrared Detector Arrays for Thermal Imaging
Tutorial "Infrared Detectors"**

(with links to Glossary)

Load this page as PDF

A. Quantum Well Infrared Photodetector (QWIP) Arrays

- Introduction and Basic Principles
- Dark Current and BLIP Temperature
- Detector Arrays
- Present QWIP projects at ACREO
- Important Publications on QWIPs

Introduction and Basic Principles
By appropriate design of **quantum wells** in certain semiconductor materials, electronic levels can be tailored to absorb radiation in the long wavelength infrared region (wavelength 3-20 um). An excellent material combination in this respect is the aluminum gallium arsenide/gallium arsenide (AlGaAs/GaAs) material system, with gallium arsenide (GaAs) being the substrate material.

The advantage of using GaAs is its mature processing technology compared to the conventional materials now used for this application, primarily mercury cadmium telluride (HgCdTe). Good quality wafers of 4" size are commercially available.Especially for large two-dimensional arrays, where uniformity is extremely important, GaAs based technology is very competitive.
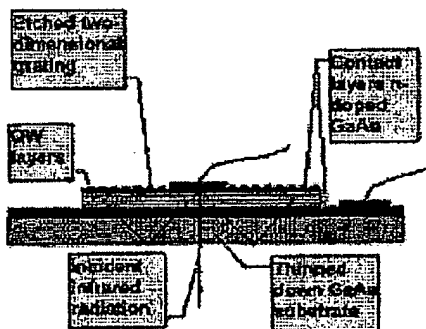
**Links for Tutorials
Tutorials Mainpage
Contact us**

■ **Detector Technol**
  Detector types and imaging, Some def
■ **QWIP Arrays**
  Introduction and B
  Optical Coupling an
  Dark Current and B
  Detector Arrays
  Present QWIP proje
  Important Publicat
● **Micro-Bolometer**
  Important Publicat
  Detectors
■ **Tutorial Glossary**

Fig. 3. *Scheme of quantum well infrared detectors for 8-10 um wavelength, with a crossed grating coupler. The substrate material is thinned down.*

Fig. 4. *A close up of a QWIP array, showing the mesa structure of the detector elements with the 2-dimensional gratings on top.*

Fig. 4 is a close up of a detector array showing the detector mesas with the two-dimensional etched gratings on top. In order to optimize the reflection properties of the gratings they are covered with gold. The central part of the surface acts as an electrical contact, and here gold germanium alloy is used instead. Gold germanium is the standard contact metal for making contacts to n-type gallium arsenide.

http://www.acreo.se/templates/Page____227.aspx   6/16/2004

PAGE 76/79 * RCVD AT 6/16/2004 6:27:50 PM [Eastern Daylight Time] * SVR:USPTO-EFXRF-1/2 * DNIS:8729306 * CSID: * DURATION (mm-ss):50-46

Dark Current and BLIP Temperature
The drawback of QWIP detectors is their comparatively large dark current. For a detector responding in the range 8-9.5 um, cooling to temperatures down to 70-73 K is necessary in order to reduce dark currents to a sufficiently low level. The temperature of background limitation (**BLIP**) is about 72K assuming the following optical parameters when the detector is part of an imaging camera system:f# = 1 and transmission of the optical system = 100%. It is here assumed that the BLIP temperature is defined as the temperature where the photocurrent is ten times as large as the dark current. Operating temperatures around 70 K are easily achievable by e.g. miniature Stirling coolers, now in common use for small hand held camera systems.
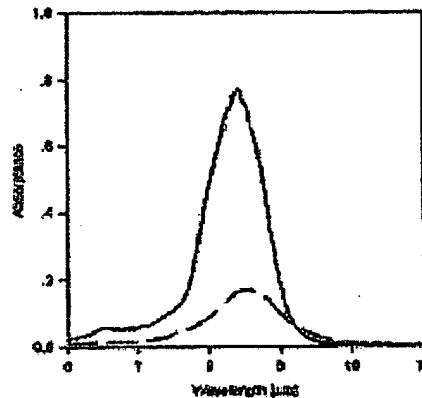

Fig. 5. Spectral absorptance vs.wavelength of a QWIP pixel (full curve), and of a corresponding polished edge detector (dashed). Both curves refer to unpolarized radiation.

The most important origin of dark current inQWIPs is **longitudinal optical phonon** excitation of carriers, and is very fundamental and therefore difficult to get rid of, except by decreasing the detector temperature. The reason for this is that coupling between optical phonons and charge carriers is very strong in **III-V materials** such as GaAs. There is however one advantage of this fact: the dark current distribution between pixels in a detector array becomes very uniform and is thus comparatively easy to compensate for.
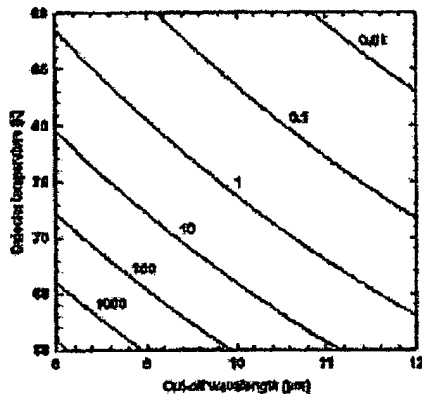

Fig. 6. Contour plot displaying (calculated) levels of constant ratio: photocurrent / dark current vs. cut-off wavelength and detector operating temperature.

Assumptions: detector with two-dimensional grating and thinned down substrate, optics f#=1 and transmission 100 %.

Background temperature=300K.

Fig. 6 displays the BLIP behaviour of a QWIP. The curve indicated with the photocurrent to dark current ratio of ten conforms with the same definition of BLIP temperature as used above. It is evident from the figure that the cooling requirements become severer the larger the cut-off wavelength is. This is a general fact for all types of infrared photon detectors.

Detector Arrays
Device Fabrication
320x240pixels QWIP arrays have been fabricated at ACREO. Such detector arrays consist of a QWIP chip **indium bump flip-chip** bonded to a silicon CMOS readout integrated circuit (ROIC). The fabrication process consists of the following steps:

- Fabrication of QWIP chip (based on GaAs)
  - Epitaxial growth of QWIP structure
  - Processing ofQWIP array
- Fabrication of ROIC (based on siliconCMOS)
- Processing of indium bumps
- Hybridization -Flip-chip bonding
- Mounting and wire bonding

The first step is to grow the QWIP structure by **MOVPE** starting with a semi-insulating GaAs wafer.

A typical QWIP structure consists of 50 quantum wells, each of width 5.0 nm surrounded på AlGaAs layers (x = 0.28) of width 35 nm. On either side of the QW structure is a contact layer consisting of highly n-doped GaAs.

The next step is to lithographically define and etch gratings into the uppermost part of the mesa. The gratings have rectangular profile with the dimensions: grating constant = 2.75 um, cavity width = 1.8 um and depth = 0.9um. Then detector mesas are fabricated by etching down to the lower contact layer. Finally metal contacts are made and a layer of gold deposited over the grating. The latter acts as a reflector for the radiation.

The **ROIC** is based on direct injection, silicon CMOS, and has one charge storage capacitor per pixel. The output signal has a serial analogue format. Amplification, A/D conversion and pixel correction is done externally to the chip.

Indium bumps are then processed onto the chips, after which the QWIP and ROIC chips are aligned and bonded in a **flip-chip bonder**. The GaAs substrate is finally thinned down by a combination of lapping and chemical etching.

Fig. 7 shows a cross-section through a detector pixel. Pixels are of square shape of side length about 30 um. The pitch between pixels is 38 um.
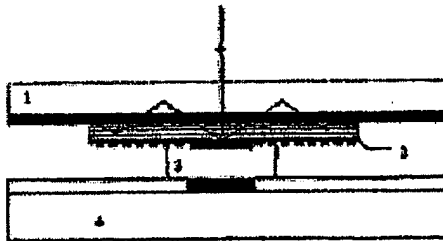

Fig. 7. Scheme of detector pixel in cross-section. 1 = dielectric reflector, 2 = QWIP structure, 3 = indiumbump, 4= readoutcircuit.

The arrows show the incident radiation, together with the multiple passes of the radiation diffracted by the grating.

The hybridized QWIP array mounted onto a ceramic substrate and wire bonded is shown in Fig. 8. The total size of the chip is 11x14 mm.
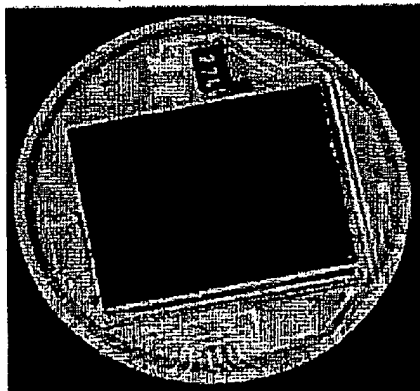

Fig.8. Photograph of a 320x240 pixels hybridized detector array mounted onto a carrier substrate.

The total size of the chip is 11x14 mm. The pitch between pixels is 38 um.

Array Performance
The 320x240 pixels QWIP array fabricated at ACREO has the following characteristics:

- The detector has maximum response at about 8.5 - 8.8 um, and spectral characteristics as shown in Fig. 5.
- The operation temperature is 70-73 K, achievable bya miniature Stirling cooler
- QWIP technology offers excellent uniformity: 2 -4 % across an array. (See histogram in Fig.

9)
- Noise equivalent temperature difference (NETD) is 30-40 mK
- Images are obtained by a two-point calibration procedure

An image of a person obtained by such a QWIP array is shown in Fig.10. Cold areas of the image are dark and warmer areas brighter.
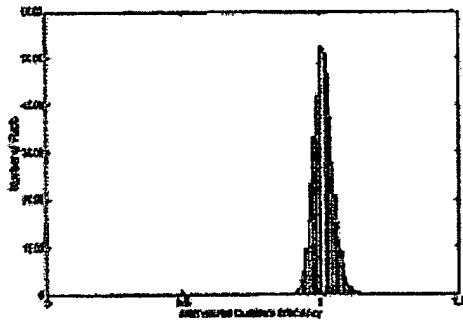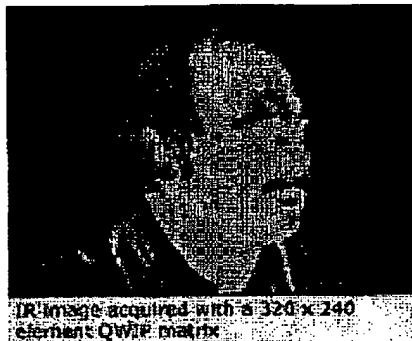

Fig. 9. Histogram of quantum efficiency normalized to unity mean value. The standard deviation is 3.3 % of the mean value across an array.

Development of detector arrays of higher resolution is under way. The main application insight is thermal imaging, for both civilian and military purposes.

IR image acquired with a 320 x 240 element QWIP matrix

Present QWIP projects at ACREO
ACREO is presently involved in a R&D project on high resolution LWIR detector arrays, MWIR and two-color arrays (i.e. MWIR + LWIR). Array sizes will be about 640x480 pixels for the LWIR arrays. The project is supported by FSI (FLIR Systems Inc.), CelsiusTech AB, Saab Dynamics AB, FMV (Defence Materiel Administration) and NUTEK (Swedish National Board for Industrial and Technical Development).

Important Publications on QWIPs

1. J. Y. Andersson and L. Lundqvist, "Near-unity quantum efficiency of AlGaAs/GaAs quantum well infrared detectors using a waveguide with a doubly periodic grating coupler", Appl.Phys. Lett 59 (1991) p. 857-859
2. J. Y. Andersson and L. Lundqvist, "Grating coupled quantumwell infrared detectors: Theory and performance", J. Appl. Phys. 71 (1992) p. 3600-3610.
3. L. Lundqvist, J. Y. Andersson, Z. F. Paska, J. Borglind, and D. Haga, "Efficiency ofgrating coupled AlGaAs/GaAs quantum well infrareddetectors", Appl. Phys. Lett.,63 (1993) p.3361-3363.
4. J. Y. Andersson and L. Lundqvist, "Grating coupled quantum well detectors", in Long Wavelength Infrared Detectors, Vol. 1, Ed.M. Razeghi, part of the series Optoelectronic Properties of Semiconductors and Superlattices, p. 207-270, Series Editor M. O. Manasreh, Gordon and Breach Science Publishers, ISBN2-88449-208-9.
5. J. Y. Andersson, "Dark current mechanisms and conditions of background radiation limitation of n-doped AlGaAs/GaAs quantum-well infrared detectors", J. Appl. Phys. 78, pp. 6298-6304, 1993.
6. J. Y. Andersson, J. Alverbro, J. Borglind, P. Helander, H. Martijn, and M. Östlund,"320x240 pixels quantum well infrared photodetector (QWIP) array for thermal imaging: fabrication and evaluation", Proceeding of the SPIE, Infrared Technology and Applications XXIII, Vol. 3061,pp. 740-748, 1997.